Kaunas University of Technology
Faculty of Mathematics and Natural Sciences

Investigation of Secondary Radiation Effects Caused by Metal Artifacts Inside the Patient's Body

Master's Final Degree Project

Egidijus Lysenko
Project author

Professor Diana Adlienė
Supervisor

Kaunas, 2021

Kaunas University of Technology

Faculty of Mathematics and Natural Sciences

Investigation of Secondary Radiation Effects Caused by Metal Artifacts Inside the Patient's Body

Master's Final Degree Project

Medical Physics (6213GX001)

Egidijus Lysenko

Project author

Professor Diana Adlienė

Supervisor

Doc. Dr. Linas Puodžiukynas

Reviewer

Kaunas, 2021

Kaunas University of Technology

Faculty of Mathematics and Natural Sciences

Egidijus Lysenko

Investigation of Secondary Radiation Effects Caused by Metal Artifacts Inside the Patient's Body

Declaration of Academic Integrity

I confirm the following:

1. I have prepared the final degree project independently and honestly without any violations of the copyrights or other rights of others, following the provisions of the Law on Copyrights and Related Rights of the Republic of Lithuania, the Regulations on the Management and Transfer of Intellectual Property of Kaunas University of Technology (hereinafter – University) and the ethical requirements stipulated by the Code of Academic Ethics of the University;

2. All the data and research results provided in the final degree project are correct and obtained legally; none of the parts of this project are plagiarised from any printed or electronic sources; all the quotations and references provided in the text of the final degree project are indicated in the list of references;

3. I have not paid anyone any monetary funds for the final degree project or the parts thereof unless required by the law;

4. I understand that in the case of any discovery of the fact of dishonesty or violation of any rights of others, the academic penalties will be imposed on me under the procedure applied at the University; I will be expelled from the University and my final degree project can be submitted to the Office of the Ombudsperson for Academic Ethics and Procedures in the examination of a possible violation of academic ethics.

Egidijus Lysenko

Confirmed electronically

Lysenko, Egidijus. Investigation of Secondary Radiation Effects Caused by Metal Artifacts Inside the Patient's Body. Master's Final Degree Project / supervisor Prof. Diana Adlienė; Faculty of Mathematics and Natural Sciences, Kaunas University of Technology.

Study field and area (study field group): Heath sciences, Medical technologies (G09).

Keywords: Radiotherapy, metal artifact reduction, MAR, Computed tomography, filtering.

Kaunas, 2021. 69 p.

Summary

Images in computed tomography are generated by using rotatory gantry and detector array movement around the patient. This fundimentally poses a problem whenever the scanned projection intercepts a dense object or a patient implant in its path. Due to the density of these implants, x-rays scattering effects may occur, creating shadow-stripe type artifacts. In many cases of radiotherapy, these artifacts are either overlooked or ignored. Only rarely they are reduced using the commercial metal artifact reduction algorithms. The re-distribution of the doses when comparing original CT images to MAR reduced images can be significant enough to sometimes reduce unwanted potential after-treatment radiation induced side effects

The aim of this paper was to evaluate the difference and re-distribution of doses to the target organs of the patients, as well as organs at risk surrounding them, according to the organ dose constraint guidelines. A metallic artifact reduction (MAR) algorithm was constructed, using different types of filtering methods traditionally used in photography and other image editing fields, for edge (detail) enhancement as well as overall image noise and blur reduction. CT data sets of 7 patients in total were evaluated for potential edge drifting and dose reduction in radiotherapy planning system. For further data evaluation, patients were split in to two groups. One group consisted of 4 patients of prostate cancer patients, while the other group consisted of 3 patients of cervix-uterus cancer patients.

It was found that the application of the MAR algorithm has resulted in a high dose reduction to the organs of interest. On average a 14.03% dose reduction to the target organ was determined for the cervix-uterus cancer patients as compared to the 2.26% dose reduction of the prostate cancer group. Dose reduction for organs at risk has also been significantly higher in the cervix-uterus cancer group of patients. Rectum organ dose on average was reduced by 8.59% among all patients of the second group, while dose reduction to the rectum in the first group was 2.26% only. Bladder in the second group of patients received a 8.53% dose reduction, contrary to the increased average dose of 4.45% for the first group of patients. It was shown that, the application of metal artifact reduction algorithm before radiotherapy treatment planning, which is based on the patients CT images, is of high importance, since these algorithms provide a significant reduction of dose to all organs surrounding target and substantial dose re-distribution.

Images in computed tomography are generated by using rotatory gantry and detector array movement around the patient. This fundimentally poses a problem whenever the scanned projection intercepts a dense object or a patient implant in its path.

Lysenko, Egidijus. Metalinių darinių paciento kūne sukeltos antrinės spinduliuotės efektų tyrimas. Magistro baigiamasis projektas / vadovė Prof. Diana Adlienė; Kauno technologijos universitetas, Matematikos ir gamtos mokslų fakultetas.

Studijų kryptis ir sritis (studijų krypčių grupė): Sveikatos mokslai, Medicinos technologijos (G09).

Reikšminiai žodžiai: Radioterapija, metalinių artefaktų slopinimas, MAR, Kompiuterinė tomografija, filtravimas.

Kaunas, 2021. 69 p.

Santrauka

Kompiuterinės tomografijos vaizdų gavimo procesas yra procesas, kurio metu KT vaizdai yra atkuriami 2D būdu, nors pats generavimo metodas yra gantrio (KT stovo) detektorių sukimasis aplink pacientą, kuomet rentgeno spinduliai "perveria" pacientą, ir šis jų pradinis ir galutinis energijų skirtumas yra atkuriamas kaip KT vaizdai. Pats šis vaizdų generavimo metodas savaime tampa problema, kuomet į skenavimo projekciją patenka įvairūs dirbtiniai protezai. Dėl šių implantų tankio, daugybė rentgeno spindulių retkarčiais yra išsklaidomi visomis kryptimis, taip sugadindami vaizdus bei sukuriant šešėlio tipo juostinius artefaktus. Dažniausiai radioterapijoje šie artefaktai yra paliekami, o tik retkarčiais būna redukuojami komercinės paskirties metalinių artefaktų redukavimo algoritmų pagalba. Pakitusi vaizdų doze radioterapijos planavimo sistemose, lyginant originalius vaizdus su MAR vaizdais, gali būti pakankamai didelė jog pacientas galėtų išvengti nenorimų atsitiktinių post-gydimo radiacinių šalutinių reiškinių.

Šio baigiamojo projekto tikslas – įvertinti dozės pokytį į pacientų organus "taikinius", taip pat į šalia esančius jautrius organus, remiantis dozių ribų kriterijais. Šiam tikslui buvo sukonstruotas metalinių artefaktų redukavimo algoritmas (MAR), naudojant įvairius filtravimo metodus, kurie tradicičkai yra naudojami fotografijų ir kitų vaizdų korekcijoms, norint paryškinti vaizdų detales, ribas, taip pat sumažinti vaizdų "triukšmą" bei blukimą. Iš viso buvo ištirti 7 pacientų KT vaizdų serijos, potencialiam organų ribų kitimui bei dozes pokyčiui radioterapijos planavimo sistemose. Tolesniam duomenų apdorojimui, pacientai buvo suskirstyti į dvi grupes. Pirmąją grupę sudarė 4 prostatos vėžio pacientai, o antrąją 3 gimdos kaklelio vėžio pacientės.

Buvo nustatyta jog, MAR algoritmo pritaikymas sumažino tiriamų organų dozę. Antroje grupėje dozių pokytis taikinyje buvo vidutiniškai 14,03%, lyginant jį su pirmosios grupės 2.26% pokyčiu. Šalutinių organų dozes redukcijos procentas antroje grupėje taip pat buvo didesnis. Tiesiosios žarnos vidutinis dozes sumažėjimas antroje grupėje buvo 8.59%, lyginant jį su pirmosios grupės 2.26% sumažėjimu. Šlapimo pūslės dozes sumažėjimas antroje grupėje siekė 8.53% lyginant jį su 4.45% dozes padidėjimu pirmoje grupėje. Nustatyta, jog metalinių artefaktų slopinimo algoritmų pritaikymas pacientų KT vaizdams yra labai svarbus prieš planuojant spindulinės terapijos dozes. nes ženkliai sumažina dozę taikiniui ir periferiniams organams.

Table of contents

List of Figures

List of Tables

List of abbreviations

Abbreviations:

CT – Computed Tomography;

RT- Radiotherapy;

TPS – treatment planning systems

MAR – metallic artifact reduction

Terms:

Edge drift – edge relocation

Introduction

In today's clinical practice, CT images are one of the most crucial methods of patient diagnosis. This patient evaluation method has seen rapid development in the last two decades. The usefulness and fast image acquisition of CT scanners have also seen an increasing number of implementations in all fields of medicine. What started, as a way of diagnosing patients fast, became an essential tool in other field of medicine, as well, such as, radiotherapy and nuclear medicine. In today's medical practice, CT images are used as ways to create treatment plans as well as to measure radiation treatment progresses in radiotherapy and nuclear medicine radioisotope treatments. For the purpose of internal treatment, CT images are used as a roadmap to guide wanted radiopharmaceuticals or external radiation beams to the desired targets. This is a very precise and cost-efficient method of patient treatment. However, despite this success, the image reconstruction processed used in CT imaging poses a significant problem due to its fundamental design. When dense objects, such as artificial prosthesis protrude in to the field of scan, a lot of times, reduction or elimination of these "artifacts" can become a challenging task. That's why this problem is sometimes ignored when working with patient CT data. Due to the rotatory nature of the image, acquisition process artifacts of all sizes can be cast in various directions, sometimes deleting or obstructing organs in the final CT image data set. In recent years however, new-post CT acquisition algorithms and filtering methods have been proposed as a way to reduce these unwanted shadow-line effects. These algorithms in the past were used as methods to edit photography data, as well as enhance or reduce unwanted noise and blurs, and in recent years have been proposed as a tool to further optimize CT images. Fundamentally, any types of data inconsistencies can lead to excessive radiation doses, especially in the previously named medical fields.

The radiotherapy process is a precise method where organs are evaluated in radiotherapy planning system software, and treatment plans are created on top of the patients CT images. Due to this, it is important to have as precise data as possible, as any errors lead to patients being over exposed to the radiation dose. This is where the proposed MAR algorithms come in to play. Many articles and papers suggest that implementing various types of filters as pre-RT technique can reduce the RT plans overall dose distribution to the target organ as well as organs at risk that are surrounding it. As the technical computational capabilities of processors is increasing so is the commercial application of the CT image editing, as most of the new CT scanners these days have their own original MAR algorithms available in the editing software provided by the supplier. To optimize patient radiotherapy plans even further, it is of great importance to investigate these potential filtering methods and their influence on the CT images.

The aim of the Master's final degree project is to identify and evaluate dose reduction capability to the target organs and organs at risk when MAR algorithms for the improvement of CT imaging data are applied prior to plan the treatment doses in radiotherapy effect.

Objectives of the Master's final degree project:

1. To investigate possible computed tomography filtering methods;

2. To assess the suitability of metallic artifact reduction algorithm application on the edges in computed tomography images;

3. To evaluate the impact of the metallic artifact reduction algorithm on the quality of the computed tomography images aimed for dose planning in radiotherapy.

1. Literature review

1.1 CT artifacts

Image filtering is a useful process that results in removing potential unwanted artifacts and other corruptions of the data, that CT images tend to be affected by when the images are affected by external unwanted processes during data acquisition. Due to X-Ray and CT-images being one of the most popular tools for patient diagnosis in the medical field, these artifacts pose an important issue, which has been addressed more and more in the recent decade. The field of CT filtering is important for further diagnosis optimization and image salvaging. According to authors like (VASPVT and European statistics department), the CT image acquisition has grown substantially, with the annual acquisition averaging around 30-40 CT acquisitions/1 mil. of population, and a growth from 1.6 to around 2 CT machines for 100000 population from the year 2013 to year 2018. This growth suggest that this trend is going to continue further with an even higher emphasis on CT and X-Ray image acquisition for better patient evaluations. Due to this, it is important to understand images affected by artifacts better. Such images sometimes suffer from errors that manifest as undesirable visual quality reduction, intense X-ray attenuations (stripe patterns) and excessive noise that hinders image evaluations, fig. 1., [1, 2].

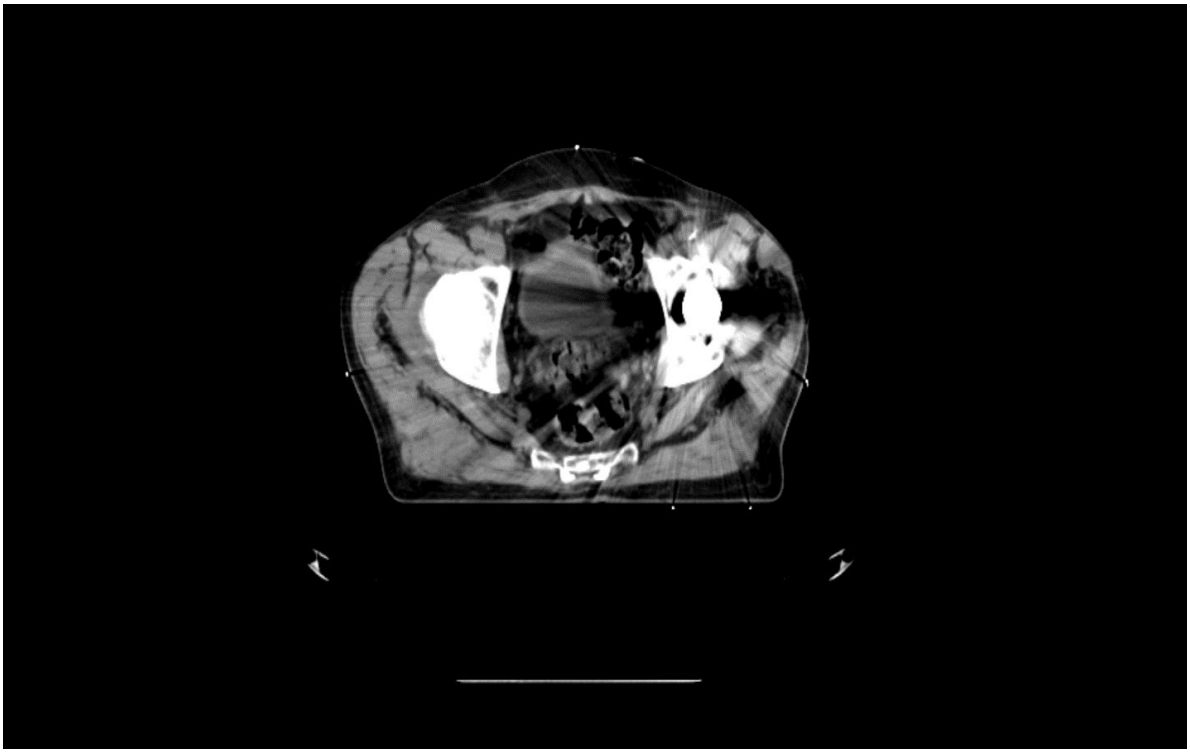

Fig. 1. Patient artifacts in pelvis region, patient No. 1., Kaunas Clinics, Hospital Of Oncology

The image series slices portrays heavy attenuation in pelvic region, making evaluation and any kind of treatment planning in case of cancer patients nearly impossible or heavily inaccurate, therefore an insight in to secondary radiation effects and artifact manifestation is beneficial for better comprehension of the possible ways to reduce such digital errors.

1.2 Secondary radiation effects and physics

Despite there being multiple artifact types that can arise due to various causes, such as detector faults, rotational gantry issues, and even higher than usual anatomical density in some particular areas of the body. The heaviest influence on the image these days remains artificial prosthesis and metallic object perturbations in to the field of scan. These perturbations result in beam hardening and scatter radiation (secondary radiation). According to (P. Sprawls), two of the main processes in CT data corruption are beam hardening along with scatter radiation. These two types of effects are the most probable and common secondary radiation effects, which happen when the beam intercepts an object in its path

causing x-ray scattering. The higher the density of the structure in the body, the more scattered radiation is produced as a result. Radiation scattering is the main phenomenon that reduces image quality when a metal foreign object falls in to the field of scan, [3].
One of the previously mentioned causes, beam hardening, occurs when x-ray beam consisting of polychromatic energies (energies that cannot be filtered using meshes and scattering filters) pass through an object, which is very high in density. The resulting attenuation of the x-rays is mostly comprised of low-end energy spectrum photons. The effect heavily resembles a high pass filter, in a way that only high-energy photons pass through and contribute to the beneficial x-ray energy beam. This results in the average beam energy being higher than the initial beam that left the x-ray tube, thus resulting in "beam hardening". The result of this – streaking artifact appears as a multiple streaks along the axis of the initial high-density object, just like fig. 1. Due to CT unit gantry (tube and detectors) rotation during the procedure the polychromatic x-rays are hardened at different rates resulting in multiple dark streaks. Beam hardening is mostly present with polychromatic X-ray sources. In polychromatic beams, transmission does not follow the simple exponential decay law seen with a monochromatic X-rays. This is a huge problem with high atomic number materials such like metallic implants. Compared to low atomic number materials such as water and fat (to some degree), these high atomic number materials dramatically increase attenuation at lower energy x-ray beams. Due to low energy X-ray attenuation being primarily consisted of the photoelectric effect, it is proportional to Z^3/E^3 , Z is the atomic number of the incident object, and E is the energy of the beam. At high energies however, attenuation is primarily due to Compton scatter, and is proportional to 1/E, [7].

The second cause for metallic object artifact manifestation is that when beam hardening occurs, a large amount of photons engages in Compton interactions along projection lines and additionally produces scattered radiation. Only some of this radiation leaves the body in the same direction as the primary beam and reaches the image X-ray detector array module. This scattered radiation contributes to reducing image contrast, and heavily enhances image noise. The degree of contrast loss depends on the scattering degree of the radiation emerging from the patient's body, in other words it mostly depends on the amount of scattering that occurs during the beam is trans-versing the patient, due to metallic interference in the beams path. When these secondary photons are produced, they are high in energy and change direction, that in itself further add to the photon attenuation problem. The previous two cause are main notable culprits for images containing streaking artifacts [3, 4].

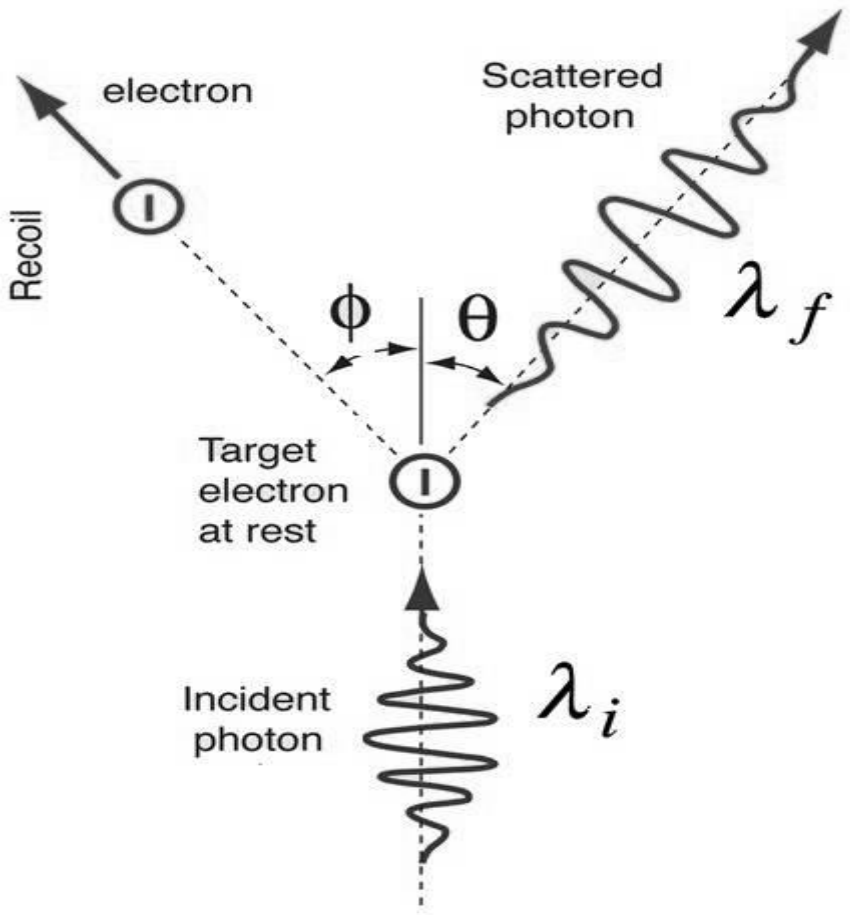

Fig. 2 A principle of Compton effect

The Compton scattering in further detail can be explained by the photon deflected through a scattering angle θ after a collision occurs. The recoil electron receives partial energy. In the process of this, photon loses energy. The scattered photon's energy in Compton principle is related to the scattering angle θ by momentum and energy conservation law:

$$E_{sc}=E_0/[1+\left(\frac{E_0}{0.511}\right)\cdot(1-Cos_\theta)] \qquad (1)$$

where E_0 – incident photon, and E_{sc} – scattered photon energies in MeV. According to the same the energy and momentum conservation law of the recoil electron, E_{re}, becomes:

$$E_{Re}=E_0-E_{Sc} \qquad (2)$$

Typically the amount of energy transferred to the recoil electron in Compton scattering ranges from nearly zero MeV, for angles θ that are close to 0 degrees (referred to as "grazing" collision), up to a maximum of E_{re}^{max} that occurs in the maximum 180 - degree backscattering events. In these events, recoil electrons are able to maintain energies high enough for further potential interactions in their path. Due to Compton scattering, further interactions of these recoil electrons and shifted photons not only increase the surrounding organ irradiation, but also contributes to the overall image quality degradation in certain areas of the image, [5].

1.3 Image reconstruction

CT image reconstruction is a crucial step in CT image generation. It has been attracting more and more attention in the recent decades, with the released number of articles yearly growing almost exponentially in the last decade. This can be represented by authors like (M. J. Willemink, P. B. Noel) in fig. 3.

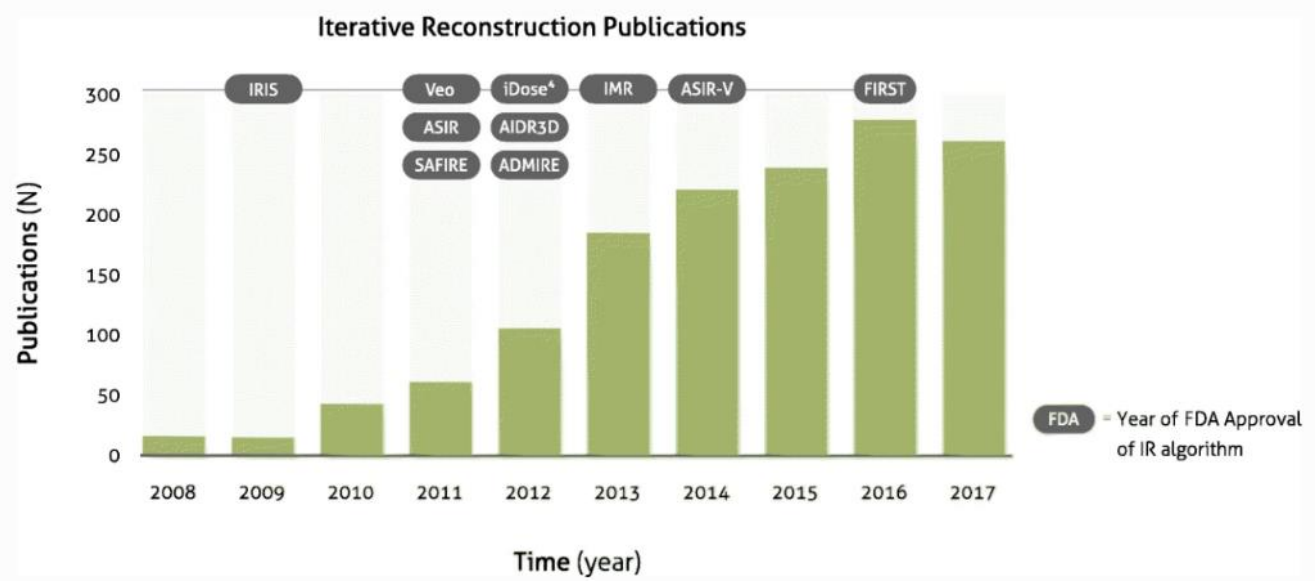

Fig. 3. Iterative algorithm article growth 2008-2017, "PubMed" database, [6]

In general, for the images to be represented in correct manner visually as it is know, the attenuation coefficients of different x-ray absorption paths (ray sum) have to be calculated. They are obtained as a set of data (projection). To understand this process in further detail it is important to understand the way filtered back projection works in today's commercially available CT scanners.

Authors like (M.T. Al Hussani, M.H. Ali Al Hayani) state that, image reconstruction process aims to estimate object's image slice f(x, y) from a set number of projections p(t, θ). To achieve this image reconstruction algorithms are used. The "Filtered back projection" algorithm is often called as a convolution method. Such methods are used as a one-dimensional integral equation for the reconstruction of a two dimensional image. This algorithm has gained wide spread success, and is the most popular reconstruction method used today in CT applications. It utilizes a convolution filter, sometimes known as "ramp filter" to reduce the blurring associated with back projection (first iteration reconstruction algorithm used in the past), and is faster than its predecessor. Despite being a fast reconstruction method and having great advantages over its predecessor, it also has limitations regarding metallic object secondary radiation (effects mentioned previously) and artifact creation (mostly organ edge loss) during reconstructions, [8, 9].

As CT scanner takes images of the body part at projections around the body. For any given angle of the projection, the line contains brighter and darker pixels, who depend on how much the beam has been attenuated during the exposure (how much of the polychromatic energy is high-pass filtered during the beams travel).

Fig. 4. Patient No. 1, slice 54, 68 deg. projection

Fig. 4 represents a visual slice, however the CT scanners process data using the typical signal domain. Additionally, it is common to believe that the detector fan in CT machines rotate and expose the patient

to 360 degrees of irradiation, however, in reality image reconstruction requires only 180 degrees of data (180 + fan beam angle width). It does not matter which way the beam transverse the patient, therefore the rest of the 180 degree of the projections are a mirror image of the first projections. In addition, extra fan beam angle width projections are required for proper projection overlapping.

A better representation of this concept is the "sinogram method". The mirrored slices can be seen using a sinogram to display all of the different projections for a given slice stacked together. As the CT tube rotates around the patient, the parts, which are attenuated more heavily, can be clearly seen using sinograms for better representation.

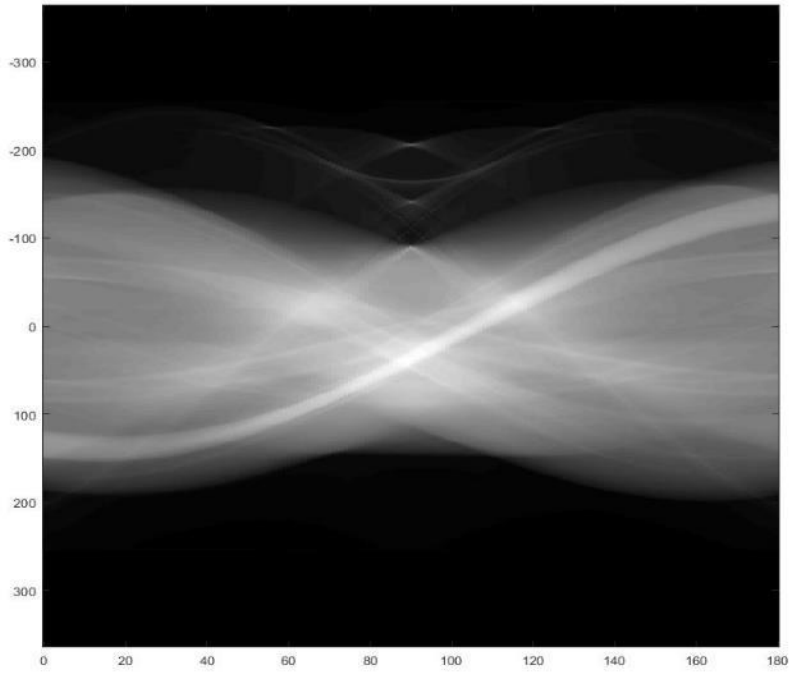

Fig. 5. Patient No. 1, slice 54 sinogram

1.3.1 Back projection and ART method

The first set of data that the CT processor acquires during the exposure are the projection beam intensity (photon intensity) data, however the real voxel data values first have to be found in order for the data to be converted in to attenuation values, that are later used in image generation. The back projection process for voxel attenuation value finding is called „Linear interpolation", [8, 11, 12, 13].

The amount of photons (photon intensity) in an X-ray beam linear voxel matrix is calculated by:

$$\mathrm{I} = I_0 e^{-(\mu_1\mu_1+\mu_2\mu_2+\mu_n\mu_n)} \qquad (3)$$

Where I is the intensity, and I_0 denotes initial beam energy, μ_1 is attenuation coefficient.

For polychromatic x-ray beams however, this intensity equation has to be altered, it becomes:

$$\mathrm{I} = \int_0^{E_{max}} I_0(\mathrm{E})\ e^{-\sum_i^n \mu_{i(E)} x_i} \mathrm{dE} \qquad (4)$$

The logarithm of the ratio of the initial photons divided by the measured photons ln(I0/I) is known as ray sums. A set of ray sums, at a particular angle can be described as an angular projection, and can be found by the following equation (5), and is later used by back projection to figure out individual voxel attenuation coefficients.

$$\ln = \frac{I_0(E)}{I} = \int_0^x \mu(E)x\,dx \qquad (5)$$

When the beam intensities and angular projection ray sums are processed, the next stage that CT processor initiates is the back projection algorithm. Many different kernels have been proposed for this next step. For the purpose of attenuation calculations such kernels that fall under ,,iterative reconstruction group" like: ,,Line kernel", ,,Joseph's kernel" or ,,Strip kernel" have been implicated, however, each and every one of them comes with their own advantages and disadvantages, mostly - processing speed that is crucial for patient investigations, [11, 12, 13].

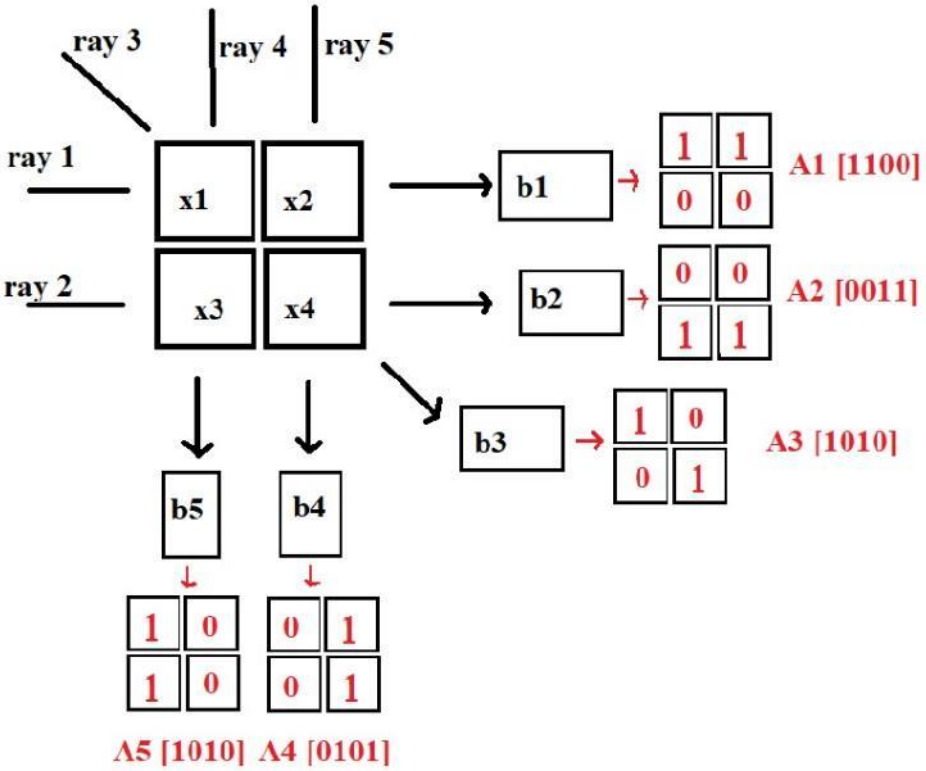

Fig. 6. Back projection schematics

The basic idea of iterative algorithms are to calculate individual voxel values after the converted beam photon intensity values are estimated according to equations (4, 5). The most widely used iterative algorithm is called ,,ART algorithm". In fig. 5. blocks a_n^{Tn} are called "weight matrix", they are necessary to be processed by computer for voxel approximation. These blocks are found using the previously explained beam linear attenuation values. The matrixes are marked by A_n operator, and are proportional to the number of N cells amount in the initial image matrix and beam angular projection numbers.

$$x = \begin{bmatrix} x1 \\ x2 \\ x3 \\ \dots \\ xN \end{bmatrix} \in \mathbb{R}^N, = \begin{bmatrix} b1 \\ b2 \\ b3 \\ \dots \\ bM \end{bmatrix} \in \mathbb{R}^{M\,x\,1}, A = \begin{bmatrix} a_1^{\sim T} \\ a_2^{\sim T} \\ a_3^{\sim T} \\ \dots \\ a_M^{\sim T} \end{bmatrix} \in \mathbb{R}^{M\,x\,N} \qquad (6)$$

For the purpose of final equation calculations for individual voxels, 3 parameters explained in equation (3) and fig. 5. are necessary. The initial cell values are $x^{(0)} = 0$, for the first image sequence. Additionally, λ_n relaxation parameter is specified by the CT scanner manufacturers depending on the cycle index, typically ranging from 1.6 – 1.8, [8, 11, 14].

The final ART iterative algorithm back-projection equation that updates voxel values row by row:

$$x^{(k+1)} = x^k + \lambda_n \frac{1}{a_i^{\sim T} a_i^{\sim}} (b_i - a_i^{\sim T} x^k) a_i^{\sim} \qquad (7)$$

Back projection reproduces the f(x, y) coordinates by averaging all projections running through a singular point called the convolution point. The average of the radon transform along the degree θ is found by:

$$\frac{1}{\pi} \int_0^{\pi} hRf(x\cos\theta + y\sin\theta)\mathrm{d}\theta \qquad (8)$$

This leads to back projection formula for a function $h = h(t, \theta)$ in polar coordinates [15].

$$Bh(x, y) = \frac{1}{\pi} \int_0^{\pi} h(x\cos\theta + y\sin\theta)\mathrm{d}\theta \qquad (9)$$

1.3.2 Filtered back projection

Radon and Fourier transform generated images blur and smear the final image, so in order to fix this, a second iteration algorithm was developed that uses the previously mentioned ramp filter to fix the these problems. The filtering alters the initial projection data – attenuation beam values in a signal domain. The filter type is sometimes also referred to as high-pass filter, or sharpening filter. These types of filters in CT algorithms pick up and enhance sharp edges, but ignores flat areas. Because the filter in reality create negative pixel values at the edges, it subtracts out the extra smearing – blurring caused by the traditional back projection.

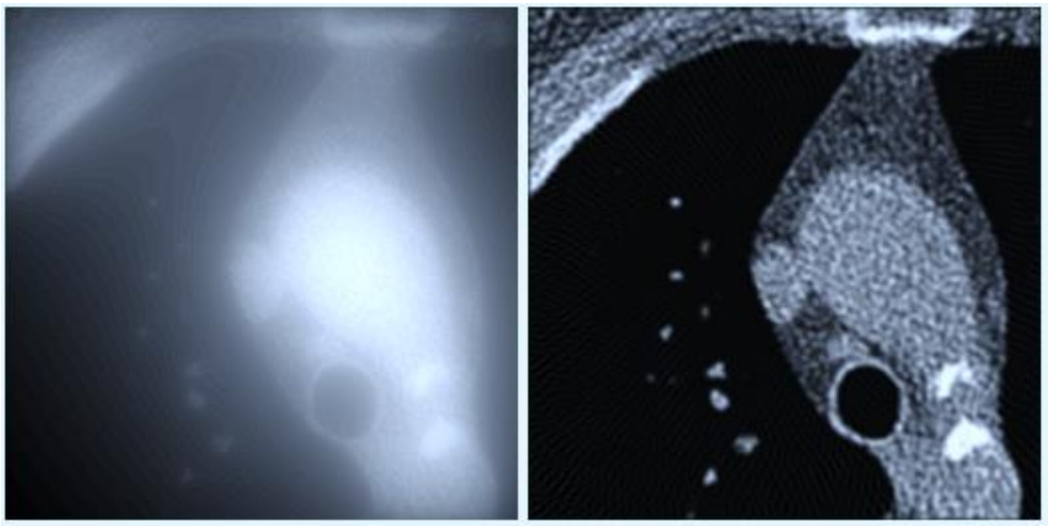

Fig. 7. Back projection – left, and Filtered back projection – right comparison, [9].

Back projection acquisition is typically a lot slower than the FBP method, therefore it is necessary to delve deeper to understand the more popular method of image reconstruction FBP, and its processes like Radon and Fourier transform projecting. When the individual voxel values for f(x, y) projection are found using ART back projection method previously, the next step is to discuss the advanced image generation sequence. Back projection creates additional excessive noise, therefore a second iteration projecting called FBP is used in today's clinical CT scanners. The basic FBP equation is:

$$f(x, y) = \frac{1}{2} B\left\{F^{-1}\left[|r| F\left(Rf(r, \theta)\right)\right]\right\}(x, y) \qquad (10)$$

where F and F^{-1}, Fourier and the inverse Fourier transforms accordingly, B is represented by back-projection voxel values used in eq. (8) for each slice, and Rf(r, θ) is the Radon transform of f(r, θ) [8, 15]. The |r| in the filtered back projection formula is very important factor. In case the equation is missing this factor the inverse Fourier transform and the Fourier transform cancels out and leaves the

back projection formula of [f], which will not allow to recover the original function f(x, y), but rather its smoothed version of this equation, [15, 16].

The $|r|$ factor in the eq. (10) can be further simplified introducing a function $\varphi(\mathrm{t})$. By introducing this function in to the previous equation, it becomes possible to further build on top of it, to represent band-limit function for image de-noising. In that case, the eq. (10), due to Fourier transform convolution becomes:

$$f(x,y) = \frac{1}{2}B(\varphi * \mathrm{Rf})(x,y) \qquad (11)$$

This equation denotation is very important, because it allows for additional filtering iterating, [8, 15].

1.3.3 Noise and filtering in Computed Tomography

Due to real CT data containing a lot of noise, the filtered back projection accentuates such noise, therefore in reality the ramp filters are designed to be "softer" or "harder", according to the image itself. The amount of noise reduced depends on "softness" of the filter itself, which is sometimes referred to as "reconstruction kernel". Different types of kernels are typically assigned for different scan protocols – scanned areas of the body. For instance, lung or bone scans focus on sharp edges and require a lot of detail, therefore a hard filter is preferred. Abdomen area on the other hand contains lots of large features, which have very gradual differences in attenuation, therefore a softer kernel is preferred for this region. Generally, the used kernels heavily depend on the area of the scan, post image processing, different view windows, as well as additional reconstructions of the areas of interest, [10, 16].

By taking a closer look at eq. (10) again, in signal domain, for signals r where they are close to zero the low-pass filter function becomes nearly $|r|$, hovewer for large values of r it nearly vanishes. The band-limiter value that represents the filter is further denoted by $A = F\varphi$, in the eq. (11), therefore the equation can be re-written as: [15].

$$f(x,y) = \frac{1}{2}B(F^{-1}\mathrm{A} * \mathrm{Rf})(x,y) \qquad (12)$$

The function A(r) of low pass filter in digital processing usually has the form $A(r) = |r|G(r)x_{(-L;L)}(r)$. G(r) is an even function of r, and G(0) = 1, $x_{(-L;L)}$ are the filters characteristic function interval, this variable A allows for filter insertion in to the FBP equation, [15, 16].

One of the most widely used previously mentioned filters in CT is the "Ram-Lak" filter, denoted by previous equation A, as:

$$A(r) = |r|x_{(-L;L)}(r) \qquad (13)$$

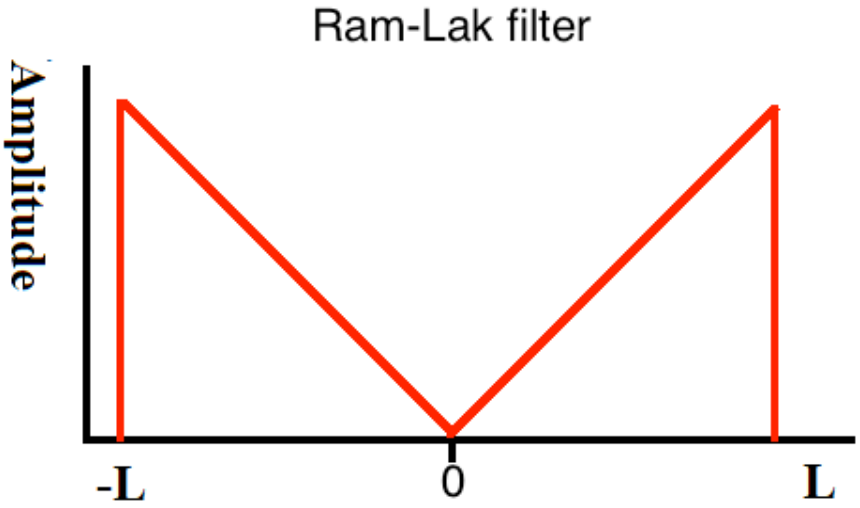

Fig. 8. Ram-Lak filter, visible $x_{(-L;L)}$ band-limit, in frequency domain

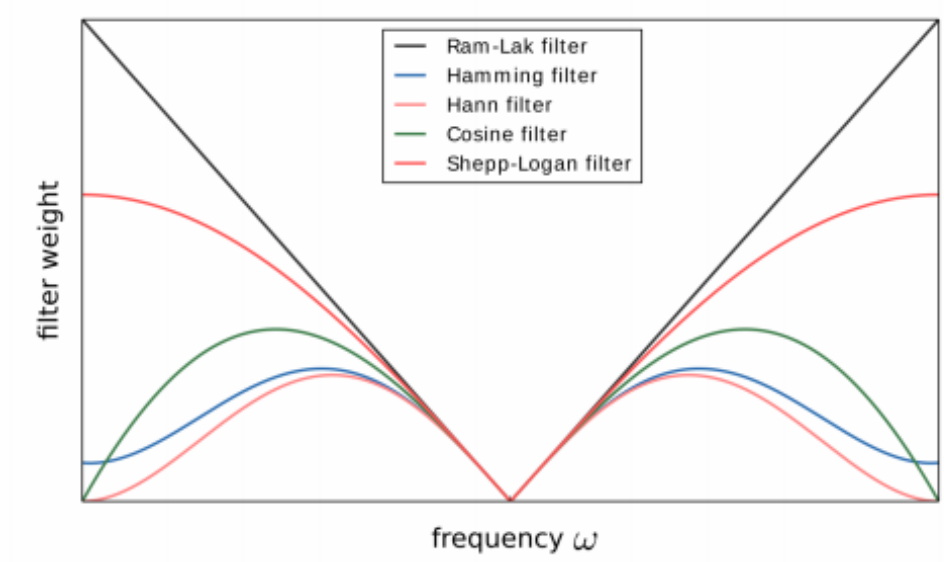

Fig. 9. Comparison of different filters used in CT FBP, different weight-frequency edges [16]

1.4 Post-Acquisition filtering

Noise in computed tomography is described as an unwanted change in pixel values in an otherwise homogenous image or organ boundaries. Often noise is defined loosely as the grainy appearance on cross-sectional imaging, but when dealing with metallic artifacts this noise can be further enhanced deleting the organ boundaries completely [17]. To counter this CT image processing does not necessarily have to be defined by the conventional image acquisition – method, but can also be built upon. There are many proposed methods that can be implemented for the purpose of image structure enhancement and editing. Many filters that have been used in digital processing and photo editing are being applied as post-processing tools in today's CT image processing. Another reason for such editing tools is that the acquisition of projection data in a Computed Tomography scanner, is usually carried out once in the typical commercial CT scanners. The projection data acquired during the intensity to attenuation domain transfer in the CT scanners is often not stored in the process, making further reconstruction with different reconstruction algorithms impossible, thus creating the need for post-process editing. Authors like (M. Ohkubo, S. Wada and others) further add to this idea claiming that, the reconstruction kernel is one of the most important parameters in CT image editing. To have access to all the reconstructions data, either reconstruction kernels must be implemented, or the projection data must be stored after the initial data acquisition. This is difficult, because all of these requirements would create a heavy burden on data archiving if all of the process data was attempted to be stored. The

proposed method by these authors essentially the same as common image filtering, which performs processing in the spatial-frequency domain with a filter function, [17, 18].

Multi-filter method also known as MAR (metallic artifact reduction) algorithm is an application of multiple filters for edge enhancement in CT processing. Some of the few filters that can be used for this purpose are: „edge – Sobel filter with edge – Prewitt operator“, „edge - Roberts with threshold“, „LOG filter with zero-crossing threshold“, „edge – Canny“, „motion blur – Wiener filter“ and „Gaussian filters“. All of these filters are essential and provide edge-detection for different areas and pixilated value inconsistencies for potential metallic attenuation effected slices. Working together, these filters provide a reasonable noise reduction, contrast and soft tissue enhancement in the peritoneal areas, organ areas, and metallic object attenuation reduction around prosthesis topography, [19, 20].

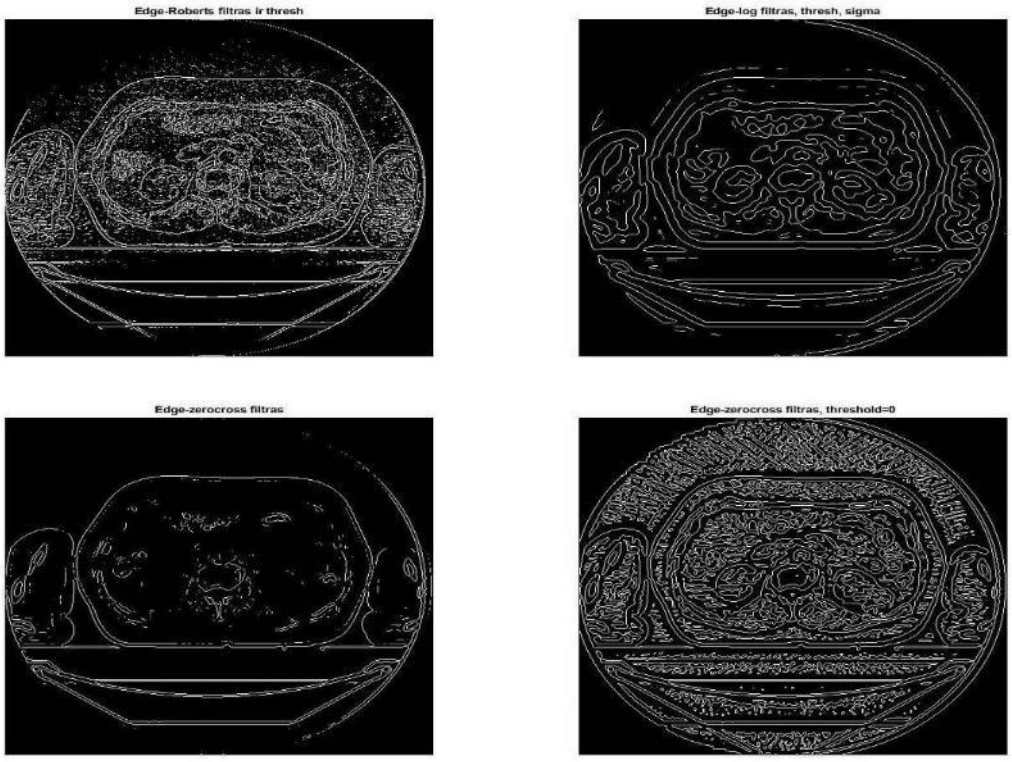

Fig. 10. Convolution edge detection image for 4 filters in “Matlab” environment, patient No. 1, Slice 20

1.4.1 Edge-Sobel filter

The Sobel method utilizes a „Prewitt operator“. This operator calculates the gradient (directional intensity change) of the image at each point of the kernel, giving the direction of the largest possible increase from light to dark and the approximation of the rate of change in that direction. The result of this is approximation of how “smoothly” the image changes at each individual point, and how likely this point is probable to be referred to as “edge”, as well as the orientation of this edge. Two mask-kernels, Sx and Sy, which are shown in fig. 11, performs convolution on the gray image and then obtains the edge intensities (gray level shifts in both directions), Gx and Gy in the vertical and horizontal directions. The edge intensity of the mask center is defined as |Gx|+|Gy |. If the edge intensity of each pixel is larger than an appropriate threshold T, set before using the kernel-mask, then the pixel in the mask is going to be regarded as an edge. Edge detection operators like “Prewitt“ reduces noise by smoothing the image, but sometimes in the process slightly enhances the bounds, by creating additional uncertainty in high-frequency variation images. The derivatives in these Sx and Sy kernels are shifted horizontally and vertically, used for the detection of horizontal and vertical shifts in edges, [21, 22, 23].

$$\begin{bmatrix} -1 & 0 & 1 \\ -2 & 0 & 2 \\ -1 & 0 & 1 \end{bmatrix} \text{ and } \begin{bmatrix} -1 & -2 & -1 \\ 0 & 0 & 0 \\ 1 & 2 & 1 \end{bmatrix}$$

Fig. 11. Sobel Sx – Left, And Sy – Right Masks, Shifted At 90 Degrees Used In Filtering Edge Detection, [21]

1.4.2 Edge-Roberts filter (Roberts cross)

The Roberts edge filter similar to Sobel filter, is used in image processing to detect edges based on the application of similar, horizontal and vertical kernels in a sequence. The kernel matrix is 2x2 instead of 3x3. Roberts filter is faster than the previous filter due to the size of the kernel matrix, but is typically subject to more interference by noise. If the edges are "blunt", there is high probability that the edge is not going to be detected, whereas Sobel and Prewitt filters are typically less interfered by noise. A combination of these filters provide a relatively great edge detection for CT images, [24, 25]. The equation for Roberts filter can be defined by:

$$z_{i,j=}\sqrt{(y_{i,j} - y_{i+1,j+1})^2 + (y_{i+1,j} - y_{i,j+1})^2} \qquad (14)$$

where z is the computed derivative and i, j represent the location coordinates in the image.

$$\begin{bmatrix} +1 & 0 \\ 0 & -1 \end{bmatrix} \text{ and } \begin{bmatrix} 0 & +1 \\ -1 & 0 \end{bmatrix}$$

Fig. 12. Roberts Cross Operator Mask Sx – Left, And Sy – Right, [24, 25]

In fig. 12., it is visible that these kernels are identical, except one of them is rotated by 90°. This is very similar to the Sobel operator explained previously, except varies in size. In this detector, the parameters are fixed which cannot be changed, thus sometimes missing or misinterpreted the edges. Convolution is performed when the kernel is dragged across the initial image matrix one pixel at a time. At each pixel, its neighbours are weighted by the corresponding value in the kernel and summed to produce a new value [26].

1.4.3 LOG (Laplacian and Gaussian) filter with zero crossing

In research papers like (S. V. Fotin, D. F. Yankelevitz, C. I. Henschke, A. P. Reeves), a LOG filter (Laplacian of Gaussian filter) is suggested as a post CT processing tool for lung nodule detection for whole lung CT scans. The typical nodule detection in todays practice is carried out using CAD (computer-aided detection) systems, however a lot of times some of these nodules are missed. For this purpose, authors propose using a LOG filter for further sensitivity increase and edge enhancement, [27]. Other authors like (B. Ganeshan, K. A. Miles, R. C. D. Young, C. R. Chatwin), in addition to the previous research paper, suggest the algorithm as a potential tool for malignant tumor (in liver) evaluation in the pelvic-thoracic areas of the body. This further proves that LOG filtering method is a wide and a very potent tool for filtering in most areas of the body. Contrary to the lung topography, the pelvic area-thoracic area is notorious for very slight attenuation, except for some occasional vertebrae perturbations to kidneys and liver organ's in some cases. The organ and bone edges in this area are a lot thicker, thus proving that the potential edge outlining is accurate enough to provide insight before surgery or radiotherapy planning. In this paper, researches have evaluated 40 patients CT images, with no contrast enhancement, and have concluded that, "… Although the findings are comparable to those previously described using CT perfusion imaging, texture analysis can be readily applied to images acquired in routine practice, thereby reducing cost, complexity and radiation burden. Abnormal texture in the absence of visible metastases on non-contrast enhanced CT could potentially be used as an indication for further investigation with hepatic MRI." [28]. Notably there has been an increasing amount of articles that suggest filtering as a cheaper alternative to sometimes performed PET procedure, for early cancer indication in non-contrast CT images and other sensitive areas. In general, LOG filter finds itself at the center of many new filter iterations proposed today.

It is important to discuss this filter method from a more technical perspective and address both of the components present in this filter. A Laplacian filter is a component used to compute second derivatives of an image, measuring the rate of change in the process. This in itself plays a crucial role in determining if the adjacent pixel values are due to edging of an organ. The Laplacian filter kernel is most commonly recognized by its negative values in a cross pattern, with corners being positive values centered in a 3x3 array, but there are other existing array types as well [26].

$$\begin{bmatrix} 0 & -1 & 0 \\ -1 & 4 & -1 \\ 0 & -1 & 0 \end{bmatrix} \text{ or } \begin{bmatrix} -1 & -1 & -1 \\ -1 & 8 & -1 \\ -1 & -1 & -1 \end{bmatrix}$$

Fig. 13. Laplacian Kernel Array

Gaussian blur (Gaussian smoothing) filter, is a filter that is used in combination with the previously mentioned Laplacian filter before the edge detection to reduce noise in the image to some degree. This image filter is a type of filter that uses a Gaussian function which in statistics is used to express a normal distribution of variables. The two dimensional function for image processing can be express by eq. (15), [29].

$$\mathrm{G(x,y)} = \frac{1}{2\pi\sigma^2}^{\frac{x^2+y^2}{2\sigma^2}} \qquad (15)$$

Where X can be denoted as the distance from the origin in the horizontal axis of the filters center, while Y denotes the distance in the vertical axis, σ is the standard deviation of the Gaussian distribution of the pixelated values. The shape of this filter manifests as a concentric circle with the distribution center being at the central point. Gaussian filter are described as a low-pass filter attenuating high frequency signals, reducing overall image noise [29].

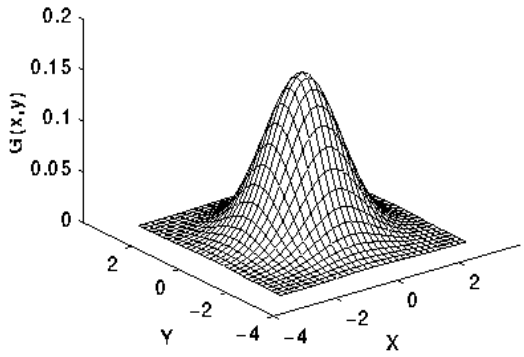

Fig. 14. Gaussian bell filter shape according to Gaussian distribution law, with a mean (0.0) and deviation = 1, [30]

$$\mathrm{LOG} = -\frac{1}{\pi\sigma^4}\left[1 - \frac{x^2+y^2}{2\sigma^2}\right] e^{-\frac{x^2+y^2}{2\sigma^2}} \qquad (16)$$

LOG kernel introduced for image processing is a combination of the two filters mentioned before. The basic idea is for a grayscale input image to detect using the „zero crossing“ method, for the second derivative of the initial CT image signal. This means that in areas of the image that have constant signal intensity gradient (gradient = o), the log response is also zero. When the kernel is in the vicinity of a gradient change, then the LOG response will be more positive on the darker side of the pixel values, and negative value on the lighter side of the homogenous area. The kernel recognizes this as a reasonably sharp edge between two regions and detects it as an edge, fig. 15. The thresholds-edge detection sensitivity is set for these zero crossings individually and only those pixels which exceed the threshold

are retained, resulting in edge detection-enhancement. Our previous Gaussian distribution kernel can be seen inverted due to the inverse secondary derivation in LOG filters, and it takes a shape of an inversed bell shape, [31].

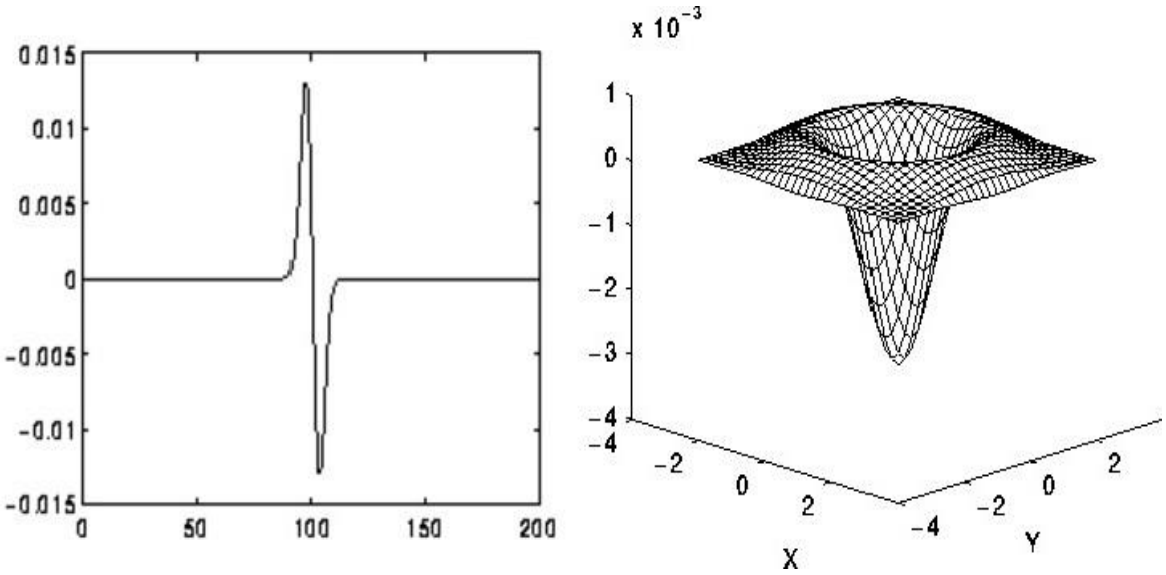

Fig. 15. Zero-Crossing edge detection signal domain - left, LOG filter shape – right, [31]

The two notable advantages for a LOG filter, compared to other filtering methods are:

- Gaussian and the Laplacian kernels are typically a lot smaller than the input image, thus this method requires far fewer arithmetic calculations and processing time;
- The LOG kernel can be pre-made in advance so only one type of convolution needs to be performed at real run-time of the filtering of the image [31];

1.4.4 Edge-Canny filter

The "Canny edge" detector filtering is a method unlike the previous ones, used for detecting a wide variety of edges in the image. It uses a multi-stage technique to achieve this. This type of filtering is very widely used in image editing, and is one of the most used type of filtering outside the medical field. Along with exceptional sensitivity of this method, three additional advantages can be pointed out in regards to this filter [32].

- The edge detection method has a low error rate, the detection catches nearly all of the edges in a typical method;
- The edge point detected from the operator, accurately localizes the centre of the edge, thus not enhancing or making the edge wider than it actually is;
- The existing edge is typically marked only once compared to other filtering methods. By doing this the noise occurring after processing is relatively low;

The process of the Canny edge detection is typically broken down and explained in to five steps:

- Application of the Gaussian filter for removing additional noise. This is a pre-filtering condition. The previously mentioned Gaussian kernel is applied in this step. The selection of the Gaussian kernel is an important variable as it determines the effectives of the Canny filter. Typically, the larger the kernel, the lower the sensitivity is to filtering noise in the image. Additionally, edge detection errors can occur if the Gaussian kernel selected in this step is too big, resulting in missed edges [32, 33].

$$\frac{1}{159}=\begin{bmatrix}2 & 5 & 4 & 5 & 2\\ 4 & 9 & 12 & 9 & 4\\ 5 & 12 & 15 & 12 & 5\\ 4 & 9 & 12 & 9 & 4\\ 2 & 5 & 4 & 5 & 2\end{bmatrix}$$

Fig. 16. Gaussian kernel 5x5 matrix, most typically used kernel in Canny edge detection

- Locating, and finding the intensity gradients using a kernel;
- Applying gradient magnitude thresholding for thinning the edges. In this step, the current pixel gradient is compared to other pixel values in the positive and negative gradient directions. To achieve this, a Sobel kernel is implemented, fig. 11. This allocates the derivatives of both horizontal and vertical directions G_x and G_y for the purpose of finding out the gradient of the pixel:

$$\mathrm{G} = \sqrt{G_x + G_y} \qquad (17)$$

  After the allocation of the pixel gradient, edge detection can be carried out using an angle calculation of the pixel gradient found by (eq. 12). Because the gradient angle is always perpendicular to the edges in an image, [33];

$$\mathrm{Angle}(90°, 270°) = tan^{-1}\left(\frac{G_y}{G_x}\right) \qquad (18)$$

- Implementation of double thresholding, for exceptionally sharp edges. After the third step in the processing, the remaining pixels provide a more clear representation of the actual edges. This step focuses more to preserve edges with big gradient values. It does this by implicating additional threshold. Same values are exposed to this threshold, and if the gradient values are higher than the threshold they are kept. In case they are lower than the selected threshold, they are filtered out. The threshold values are typically selected by the content of the grayscale image in CT, [32, 33];
- Edge tracking method. This method finalizes the fifth step, which focuses on deleting weak-unconnected edges in the intensity domain. To achieve this a "blob method" is introduced. By taking a look at a weak edge pixel and its 8-connected neighbouring pixels, as long as there is one strong edge pixel that is situated in one of the surrounded blob kernel pixels locations, that weak edge point is identified and preserved, [32, 33];

Despite the Canny edge detection filtering method finding its success in the conventional image editing, the field of filter application for CT imaging is still a relatively new field. Authors like (E. Punarselvam, P. Suresh) have used this filtering algorithm in practice, for the examination the soft tissue and vertebrae meniscus in total 29 patients that have vertebrae fixation bolts and heavy attenuation cast in lumbar thoracic vertebrae areas. They have concluded that, the object boundaries recovered in noisy images are very close to the boundaries given my doctors. They were capable of successfully applying edge detection technique to enhance boundaries of spine disc in spinal images, [34].

Another research paper has investigated the potential uses of different filters in the pelvic area of the patients with hip prosthesis in conventional X-ray imaging. Authors (A. Castro, C. Dafonte, B. Arcay) have evaluated 40 patients' images with medical professionals and they have concluded that: the best results were achieved when using Canny and Heitger edge detectors filters. They have also concluded that Canny algorithm obtains its best results with a low sigma value selected as a threshold. In their paper they suggest that, high values cause considerable loss of information because of the low signal/noise relationship (mainly in the area where the bone and the iron coincide), and that lower sigma values are preferred [35].

The edge canny filter cannot only be used for robust morphological region boundary detection, but also other more delicate areas of the body, such as lungs. Authors (R. Noviana, I. Rasal, E. U. Cintamurni Lubris) have investigated the potential use of canny edge detection for the lungs region as a pre-surgical tool surgery planning for nodule detection. In their paper, they have segmented lung areas that require surgery, and then edge Canny filter was introduced to further outline the edges and measure the distances before the surgical procedure. They have concluded that, ‘‘the segmentation methodology shows an honest result. It obtains an awfully smooth edge. Moreover, the image background can also be removed in order to get the main focus, the lungs‘‘ (p.8, [36]). This suggests a potential implementation in the pre-surgical planning field in patients whose CT images suffer from heavy attenuation or require precise measuring. The lung region filtering is a relatively new technique, but a crucial one. In the past few years many new iterations for the Canny edge detector were proposed that focus on detecting different pathologies in the lung areas, due to very gradual drift in pixelated values when abnormalities are present in this area. Lung cancer and nodule detection are a relatively new areas of filtering investigation. In the last few years even Covid-19 patient identification edge detecting has been proposed as methods based on the Canny filtering. The second iteration Canny filtering is becoming more and more accepted in the medical field and have found different medical areas to focus in manifesting as subgroups of this algorithm, namely, ,,Enhanced Caddy filtering“ ,,CAD‘‘ and ,,Automata‘‘ filtering, [37, 38].

1.4.5 Motion blur (Wiener filter)

Wiener filter is typically used as a tool to reduce the motion blur in images affected by sudden movement, or in some cases excessive noise. It uses a different approach than the previously mentioned filters by filtering in the power spectrum domain. A statistical estimate is carried out in an input signal that’s been corrupted by noise, to estimate the real signal values lying underneath. The statistical estimating of the real signal values is based on the minimum mean square error theory. Wiener filter is typically characterized by: [39].

- Signal and noise are stationary linear stochastic processes with known spectral characteristics or known autocorrelation and cross-correlation;
- The filter is causal;

Wiener filter in Fourier domain can be expressed as follows:

$$\mathrm{W}(f_1, f_2) = \frac{H\cdot(f_1,f_2)S_{xx}(f_1,f_2)}{|H(f_1,f_2)|^2 S_{xx}(f_1,f_2)+S_{\eta\eta}(f_1,f_2)} \qquad (19)$$

where $S_{xx}(f_1, f_2)$ is the power spectra of an image and $S_{\eta\eta}(f_1, f_2)$ expresses additive noise. $H(f_1, f_2)$ is the blurring filter. The equation expresses two basic principles of the Wiener filter named previously - inverse filtering (deconvolution), and noise smoothing. This is achieved by deconvolution when using the inverse filtering (high-pass filtering). After this, the removal of the noise is carried out by the compression operation (low-pass filtering) contrary to the step before, [40].

Power spectra generation and additive noise estimation is a complex process. The typical power spectrum is equal to the variance of the noise. To estimate the power spectrum of the original image many methods can be used, however in reality, due to fast processing in today’s processors a “periodogram” is used to estimate of the power spectrum, [40].

$$S_{xx}(f_1, f_2) = \frac{1}{N^2}[Y(k, l)Y(k, l)] \qquad (20)$$

where $Y(k, l)$ is the discrete Fourier transform (DFT) of the observation, N is the variance of the noise. Noise estimate is determined by:

$$\Delta S_{\eta\eta}(f_1, f_2) = \frac{S_{xx} - S_{\eta\eta}}{|H|^2} \qquad (21)$$

where H is in the eq. (21), can be a simple kernel. Typically, a smaller kernel is used for the reconstruction.

$$\mathrm{H} = \frac{1}{16} = \begin{bmatrix} 1 & 1 & 1 & 1 \\ 1 & 1 & 1 & 1 \\ 1 & 1 & 1 & 1 \\ 1 & 1 & 1 & 1 \end{bmatrix}$$

Fig. 17. Wiener 4x4 kernel

Wiener filter in combination the other filters mentioned previously provides a great possibility for noise reduction. Authors like (C. Anam, F. Haryanto, R. Widita, I. Arif) have conducted an investigation, where Prewitt operator with Sobel filter, along with other edge detecting algorithms were combined. They have concluded that, "From the measurements, the new method can reduce the noise to an average 64.85%", [41].

Other authors further add to this idea of applying Wiener filter in coordination with other edge detectors for substantial noise reduction. (C. Anam, T. Fujibuchi, T. Toyoda and others) in their research concluded that: when using the modified Wiener filter-edge detection, the spatial resolution of the image remained relatively as good as the original image, in other words, the edges of the temporal bones investigated were still very sharp and detailed enough to perform evaluations. It is correct to assume that, the filter in combination with edge preservation has the potential to keep the edges of organs and bones relatively sharp. In accordance to this, it also reduces the noise in the image substantially [42].

1.5 CT radiotherapy planning

CT imaging is the most often used medical imaging procedure for radiotherapy planning in the RT field because of its fast acquisition and availability. CT images used in RT have to serve two purposes: to provide high geometric fidelity and the position of the tumour with surrounding tissues, and OAR's (organs at risk) to be accurately identified. This is where previously explained filtering algorithms have the potential to come in to play. They provide better boundaries (edges) for organs and significant noise reduction for the RT planning. This is very important because RT planning systems are very sensitive to heavy attenuation noise (specifically metallic prosthesis) and excessive noise. The most important steps in every RT planning is the target and OAR identification, organ contouring and plan selection. To better understand this, focusing on the pelvis and sacrum-lumbar areas of the CT scans is helpful, as organ identification is relatively easier for non-medical professionals when comparing to other areas.

According to worldwide cancer data, the most common cancer types in the mentioned areas in male patients today are prostate (14.5% of all cancer cases) and colorectal (11.4%). For women, cancers frequently occurring in these areas today are colorectal (9.7%), cervix-uterus (6.9%). This paper is consisting of both men and women CT scans, for that reason, for greater organ recognition and identification, prostate and cervix-uterus cancers were selected as an investigation target. To do this, a great topographical knowledge of CT images, target organ and OAR boundaries and locations is necessary, [43].

1.5.1 Prostate RT

The contouring of the CT images according to the guidelines for prostate cancer cases involve scrupulous planning around the lover and upper pelvic areas of the body. Target organ is close proximity to bones of the lower pelvis, as well as very sensitive structures of the reproductive system. When creating a prostate RT plan, these structures are typically outlined, [44, 45]:

- Femoral heads;

- Bladder;
- Penile bulb (in male anatomical topography, just slightly below prostate, at the base of prostate);
- Rectum (dorsal side, situated closely to the lower side of the bladder);
- Small and large bowels (typically hard to distinguish, and in most cases with artifact streaking nearly impossible);
- Seminal vesicles;
- OAR space (an intraperitoneal space sometimes created in between rectum and prostate or bladder). This space is created through an interventional large bowel wall puncture-injection. This results in reducing OAR irradiation, [44, 45];

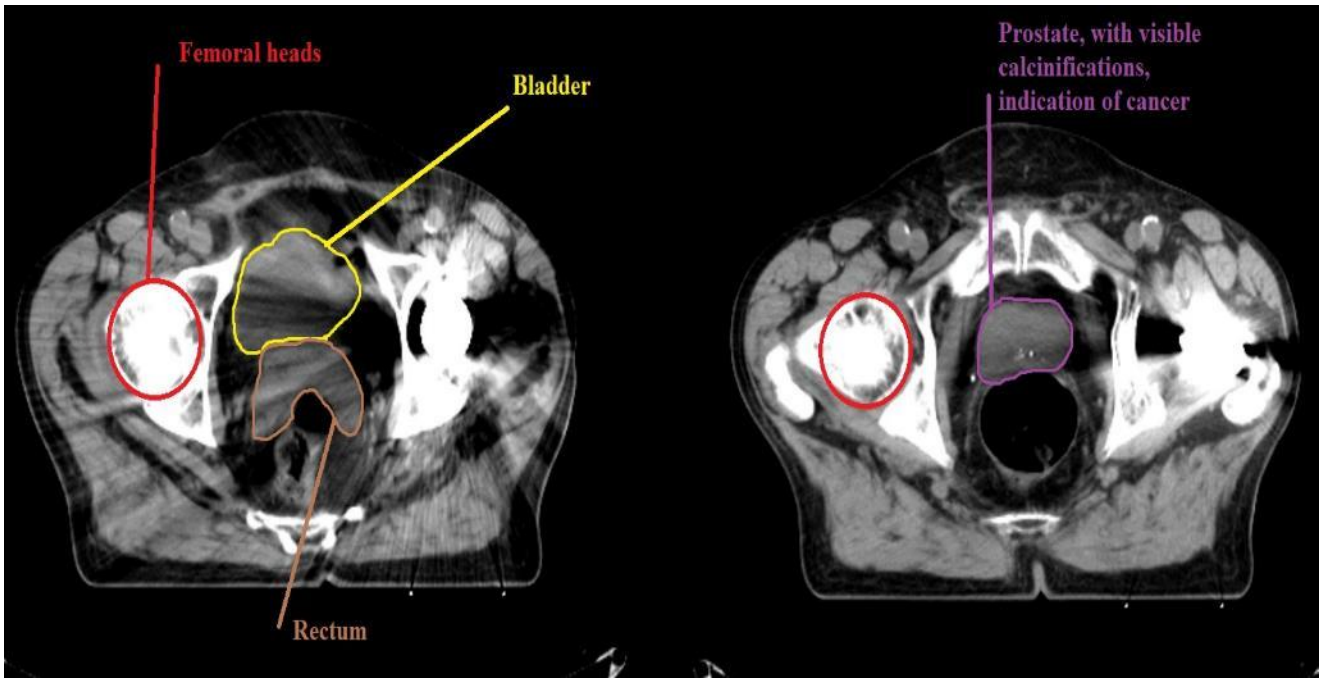

Fig. 18. Patient No. 1, pelvis prostate target and OAR outlining, visible attenuation from prosthesis, Kaunas Clinics, Hospital Of Oncology

Fig. 18 displays the target and surrounding important structure topographical locations in in the small and greater pelvic areas. Due to metal attenuation, bladder boundaries in some of the slices in the original image are hardly recognizable. Other OAR's that are difficult to distinguish in images like these are rectum and seminal vesicles. When RT plans are created, one of the most important structures to outline are the femoral heads, because osteocytes and bone marrow are very sensitive to radiation and potential complications that may arise from over-exposition of the radiation [44, 45].

According to most prostate planning guidelines in RT planning, despite occasional papers suggesting lower and individualistic doses to patients with additional investigation, the recommended treatment dose is 74 Gy. / 2Gy. per fraction. Additional rules have to be implied. Typically:

- 95% of the prescribed dose covers at least 95% of the PTV volume;
- At least 99% of the GTV volume should receive at least 100% of the prescribed dose;
- Each femoral head cannot receive higher than 10% of the prescribed dose;
- Penile bulb should not exceed 60 Gy. dose, and mean dose must remain below 52.5 Gy;

These rules are strictly follower, however, sometimes due to the difficulty or unusual anatomical topography, some of the constraint values can be increased in accordance with medical oncologist reference.

Table 1. OAR constraint for prostate cancer patients, [46, 47, 48]

Rectum	Bladder	Small bowel

50% volume < 60 Gy. 35% volume < 65 Gy. 10% volume < 70 Gy.	50% volume < 65 Gy. 35% volume < 70 Gy. 25% volume < 75 Gy. 15% volume < 80 Gy.	35 Gy. receiving volume < 180 cm^3 40 Gy. receiving volume < 100 cm^3 45 Gy. receiving volume < 65 -150 cm^3

1.5.2 Cervix-Uterus RT

- Due to very sensitive nature of the soft tissue in the lower pelvic area for cervix-uterus cancer patients, the RT planning has to be very precise. Typically, 3D conformal radiation therapy is done with accordance with brachytherapy after the fractioned RT treatment is carried out in 5 weeks' time. Just like the prostate cancer plan, there are some OAR's that have to be particularly cared for when creating a cervix-uterus RT plan. Structures typically outlined are, [44, 45]:
    - Femoral heads;
    - Bladder (dorsal proximity to the uterus and fallopian walls);
    - Rectum (also in close proximity to the uterus);
    - Small and large bowels;
    - Liver and kidneys (outlined in some of the cases);
    - Spinal cord (in the sacral area), [44, 45];

Fig. 19. Patient No. 6, cervix-uterus and OAR outlining in lower pelvis, visible attenuation from femoral head prosthesis, Kaunas Clinics, Hospital Of Oncology

The typical doses prescribed for Cervix-uterus RT plan are in the range 45-50 Gy. / 2Gy./fr. Similarly to prostate RT planning rules, additional restraints have to be implied, [49]:

- 95% of the prescribed dose covers at least 95% of the PTV volume;
- At least 99% of the GTV volume should receive at least 100% of the prescribed dose;
- Each femoral head cannot receive higher than 10% of the prescribed dose;

Table 2. OAR constraint for cervix-uterus cancer patients, [49]

Rectum	Bladder	Liver	Kidneys	Small bowel	Spinal cord
50% volume < 37 Gy. 35% volume < 40 Gy. 10% volume < 43.5 Gy.	50% volume < 40 Gy. 35% volume < 43.5 Gy. 25% volume < 47 Gy. 15% volume < 50 Gy.	30% volume < 20 Gy.	Each kidneys < 18 Gy, or 20 % volume < 17.5 Gy.	40% volume < 35 Gy.	< 50 Gy.

Both prostate and cervix-uterus cancer RT planning systems can provide us with great information in regards to filtering. By measuring the reduced noise and attenuation as well as increased contouring of the organs in filtered images, a change in the RT doses to the targeted organs in the RT plans and the organs around them becomes apparent.

2. Materials and methods

2.1 Software and tools

Matlab software; in this work Matlab environment was used for coding and metallic object x-ray attenuation for CT reduction. Algorithm was built using Matlab program. This environment allowed for great algorithm building, because there are many original functions built to specifically focus on DICOM format files, as well as edit various parameters of the images. The build algorithm consists of three parts. Anonymization of the patient, filter application, and original data-parameter saving.

RadiAnt; is another software tool used to view DICOM format files. This software was crucial for understanding patients slice compositions and the variables contained in their data. The usefulness of this this software has allowed for a quick to look in to some of the crucial parameters of each slice. Parameters like ‘’InstanceNumber’’ and ‘’SeriesNumber’’ are crucial for any filter or algorithm application in CT image editing. RadiAnt allows for viewing of this important data.

PlanUNC; radiotherapy planning software used for original and filtered CT images to create radiotherapy plans. Three-dimensional (3D) treatment planning is one of the most important steps in the treatment of various cancers when radiation treatment is prescribed. Typically, RT treatments are prescribed when the gross tumour volume lies in a difficult to reach area, or is proximal to critical bodily structures such as bladder, prostate, cervix-uterus etc. PlanUNC toolset provides a possibility for an extensive RT planning. Tools like energy selection, beam manipulation, as well as beam isocenter alteration and wedge selection are used for optimizing the initial CT and MAR filtered CT image sets to being as close as reasonably possible to the required guideline values. Due to metallic artifact image corruption, this sometimes is difficult to achieve. Despite this, PlanUNC toolset is extensive, and this makes it relatively achievable under these difficult conditions.

2.2 Algorithms and filtering

The applied MAR algorithm used for the image processing consisted of: “edge – Sobel, with Prewitt operator”, “edge – Robert” with thresholding (Roberts cross operator), “LOG” (Laplacian and Gaussian) with zero crossing, “edge – Canny”, and “motion – blur” (Weiner) filters. All of these filters acting together and detecting different edges make the MAR algorithm. The MAR algorithm focuses on contrast – soft tissue enhancement in the peritoneal and pelvic areas, as well as metallic object attenuation, and image noise reduction around hip prosthesis areas. For desired edge enhancement, “Sobel filter” threshold was selected to be 0.0003, while “Prewitt operator” was set to 0.0001. For “Roberts cross operator” a threshold of 0.0002 was selected. LOG filter threshold value was set to be 0.000002, while “zero-cross” operator was set to 0.00001. For “Canny filter” threshold of 0.0001 was selected. “Motion blur” filter values of “len – linear motion camera”: 200 and theta of 45 were introduced. These filters acting together “caught” most of the edges present in the CT images, fig. 10 and appendix 1.

2.3 DICOM parameters and anonymization

The first step in the image processing involved anonymization of the CT sets, appendix 1. In (Fig. 20), portrays the basic DICOM image parameters. The format of the image is holding not only the pixelated values of the matrix of the image, but also personalized information of the provider, physician as well as patients ID themselves and many other attributes. Some of these parameters are crucial to the DICOM images for file editing. If corrupted or altered, the image may be unreconstructable. In this case, the highlighted parameters are the crucial values of the image. As a rule, “StudyInstanceUID’’ and ‘’SeriesInstanceUID’’ variables have to be separate from one another and from the original DICOM image (slice), however, have to be maintained throughout the whole series – slices as the same code. Only then, the anonymized images are considered belonging to a singular instance study, as without this, the images are scattered. In built Matlab environment commands help with this, as they allow these

parameters to be opened in the editing tool and saved, exported and copied. Additionally, “InstanceNumber” variable has to be maintained and be identical to the original slice’s instance number. This variable represents an order of slices in the CT series, therefore the instance number and the name of the file have to be identical, so that any RT and DICOM viewing software could display the image in the correct sequence. Lastly and most importantly, part of the DICOM file editing involved “SOPClassUID” variable editing, due to the fact that original matrix pixel values and information of the image are stored in this variable as a 2D matrix kernel. The newly acquired matrix data (after filtering) has to over-ride the previous values. For this purpose, special Matlab commands are implemented and the matrix of the new processed images are copied and written in the new DICOM info file. To achieve this, DOI and ROI – crucial data preservation DICOM variable functions were used as means of countering unwanted data tampering and data corruption.

```
info = struct with fields:
                        Filename: '/mathworks/devel/bat/Bdoc20b/build/matlab/toolbox/images/imdata/                dcm'
                     FileModDate: '
                        FileSize: 525436
                          Format: 'DICOM'
                   FormatVersion: 3
                           Width: 512
                          Height: 512
                        BitDepth: 16
                       ColorType: 'grayscale'
  FileMetaInformationGroupLength: 192
      FileMetaInformationVersion: [2x1 uint8]
         MediaStorageSOPClassUID: '1.2.840.10008.5.1.4.1.1.7'
     MediaStorageSOPInstanceUID: '1.2.840.113619.2.1.2411.1031152382.365.1.736169244'
              TransferSyntaxUID: '1.2.840.10008.1.2'
         ImplementationClassUID: '1.2.840.113619.6.5'
      ImplementationVersionName: '1_2_5'
    SourceApplicationEntityTitle: 'CTN_STORAGE'
        IdentifyingGroupLength: 414
                     ImageType: 'DERIVED\SECONDARY\3D'
                  SOPClassUID: '1.2.840.10008.5.1.4.1.1.7'
                SOPInstanceUID: '1.2.840.113619.2.1.2411.1031152382.365.1.736169244'
                     StudyDate: '1993.04.30'
                    SeriesDate: '1993.04.30'
                   ContentDate: '1993.04.30'
                     StudyTime: '11:27:24'
                    SeriesTime: '11:27:24'
                   ContentTime: '11:27:24'
                      Modality: 'CT'
                ConversionType: 'WSD'
                  Manufacturer: 'GE MEDICAL SYSTEMS'
               InstitutionName: '
        ReferringPhysicianName: [1x1 struct]
                   StationName: 'CT01OC0'
           StudyDescription: 'RT ANKLE'
  NameOfPhysiciansReadingStudy: [1x1 struct]
               OperatorsName: [1x1 struct]
        ManufacturerModelName: '            '
           PatientGroupLength: 18
                  PatientName: [1x1 struct]
       AcquisitionGroupLength: 10
             SoftwareVersions: '03'
     RelationshipGroupLength: 134
              StudyInstanceUID: '1.2.840.113619.2.1.1.322987881.621.736170080.681'
             SeriesInstanceUID: '1.2.840.113619.2.1.2411.1031152382.365.736169244'
                  SeriesNumber: 365
                InstanceNumber: 1
 ImagePresentationGroupLength: 168
              SamplesPerPixel: 1
   PhotometricInterpretation: 'MONOCHROME2'
                          Rows: 512
                       Columns: 512
                BitsAllocated: 16
                   BitsStored: 16
                      HighBit: 15
         PixelRepresentation: 1
     SmallestImagePixelValue: 0
           PixelPaddingValue: 0
                WindowCenter: 1024
                 WindowWidth: 4095
             RescaleIntercept: -1024
                RescaleSlope: 1
                 RescaleType: 'US'
    PixelDataGroupLength: 524296
```

Fig. 20. DICOM file variable list in the file parameters, using Matlab “Dicominfo” function

After this, post-processed CT images were then evaluated using the previously mentioned CT DICOM viewing software “RadiAnt”. To achieve this, a universal organ bladder was selected, as edge detection is most visible in this area throughout all of the patients. And measurements were done across the bladder and compared to the new values of the filtered CT images for every slice containing bladder, Fig. 21

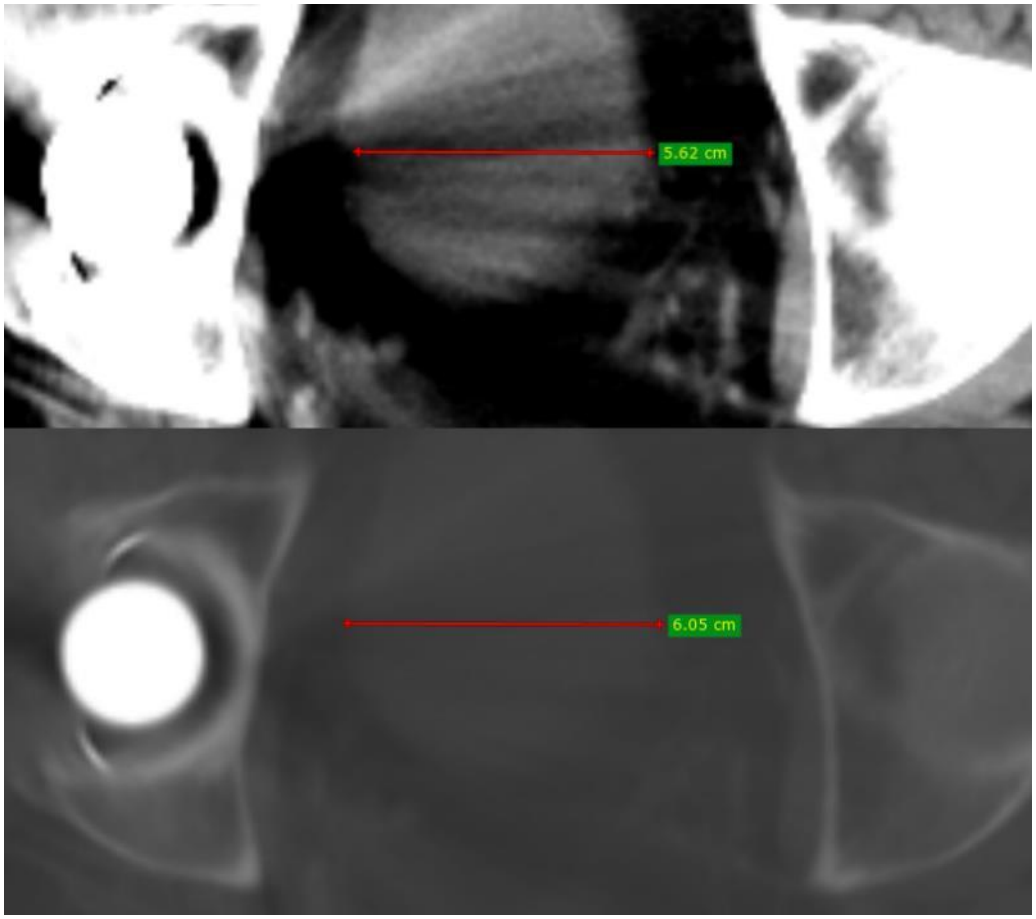

Fig. 21. Edge measurement in patient No. 1, slice 44, bladder organ, Kaunas Clinics, Hospital Of Oncology

After the anonymization process and image filtered matrix over-riding was complete, the images were ready to be implemented in to "PlanUNC" RT environment where the difference in volumetric data can be explored for the original and altered CT data sets. This was done in accordance to the "PlanUNC" user manual, and involved "command prompt" coding and binding of individual slices to a singular study, [50]. Root directory creation and image name-root sharing - "root name" is essential for this step. All of the slices had to start with the same symbol. For instance, "001", "002"… for the images to be opened and RT plan to be executed.

2.4 Patient information

2.4.1 Patient No. 1

Patient No. 1 consisted of 72 slices in the original CT data set. In fig. 22 and fig. 23, heavy attenuation of the left hip prosthesis is present. Left bladder organ bound deletion is present in this patient, as well as fat tissue deletion around the left hip area. This additionally resulted in unwanted noise increase throughout most of the pelvic slices. After the MAR algorithm implementation, a substantial bladder edge enhancement is seen, as well as attenuation reduction in all of the slices.
After the MAR algorithm implementation, RT plans for the original and filtered data sets were created identically. 4-beam technique was selected for this patient. Beams were placed at 0°, 45°, 180° and 315°. A beam energy of 15MeV Primus2 was selected with no additional wedges required for this patient. Autofocus-prostate, 1 mm. margin was also used for this patient. The 3D dose of the patient displayed value of 102% for the selected guideline dose of 74 Gy, 2 Gy per fraction.

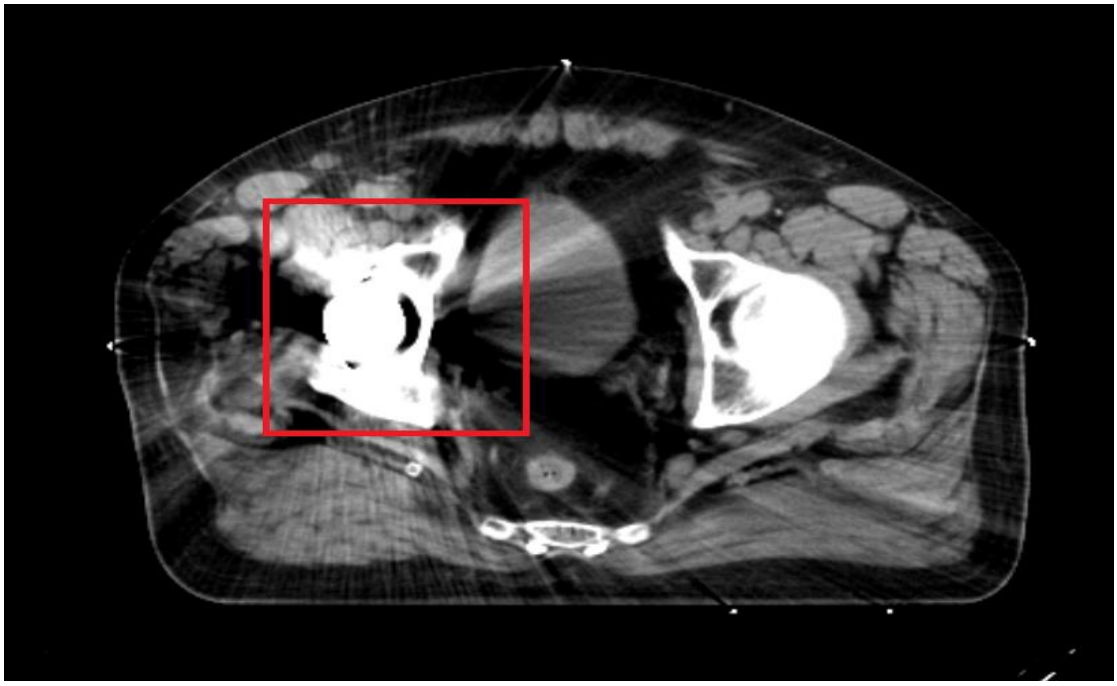

Fig. 22. Patient No. 1, original CT, slice No. 41, Kaunas Clinics, Hospital Of Oncology

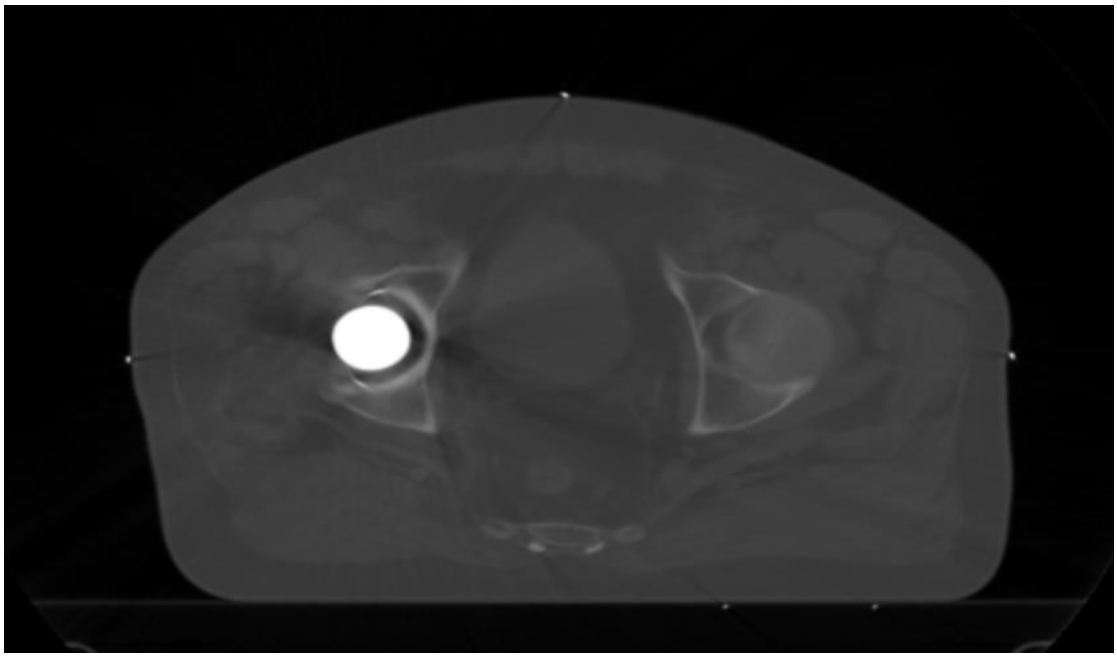

Fig. 23. Patient No. 1, MAR algorithm CT, slice No. 41, Kaunas Clinics, Hospital Of Oncology

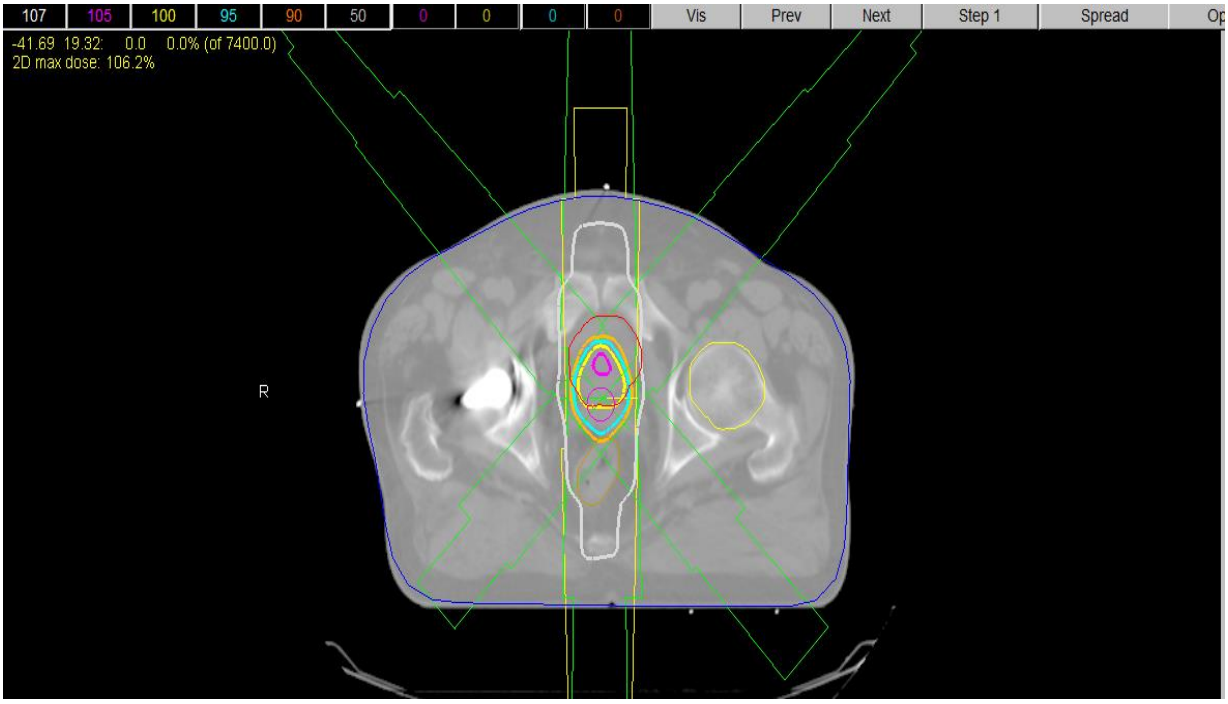

Fig. 24. Patient No. 1, RT planning, prostate projection

2.4.2 Patient No. 2

Patient No. 2 CT data set consisted for 65 slices of the pelvic region, in the original RT plan of the patient. In the provided slice No. 44 of the initial CT data set, some calcification is present in the prostate – bladder area, additionally heavy attenuation protruding from the right hip prosthesis in to the peritoneal area is visible for this patient, appendix No. 2. This heavily affected the prostate edges and surrounding organs bounds throughout most of the slices. From the newly acquired MAR images, it is seen that the previous perturbations of the right hip joint x-rays have been reduced. More anatomical structures, such as intraperitoneal muscle are visible around the metallic prosthesis. The areas around the metallic joint in the image become much clearer, and easier to evaluate and organ draw in RT software.

After this, identical RT plans were created for both of the CT data sets using the “PlanUNC” in-built coordinate system for orientation of organ drawing. According to the guideline dose values, 4 beams were selected at 0°, 45°, 180° and 315° with wedges placed on the last 3 beams, 30 deg./rt, 30deg./lt and 30deg./out accordingly. The dose selected was according to the recommendations 74 Gy, 2 Gy per fraction with beam energy being Primus 2. 15 MeV. Autofocus function was selected, for proper prostate organ targeting with a 1 mm. margin. Radiation treatment plan displayed an overall 3D dose of 107%, not exceeding the maximum allowed value of 107%, in addition not being below the minimum threshold of 95%

2.4.3 Patient No. 3

Patient No. 3 consisted of 117 slices. In this patient, heavy attenuation of the right hip prosthesis is present in the lower pelvic area. Heavy X-ray perturbation and noise is present to the prostate, bladder and rectum organs. After the filtering, noise has been reduced, with image bounds being more visible for all of the patient slices, appendix 3. This patient RT plan consisted of 4-beam technique, placed at the previously named degrees. A wedge 30deg/out was placed at 180°. This has helped to reduce dose as reasonably as possible to the rectum OAR, while providing enough energy to make the plans 3D dose 105%.

2.4.4 Patient No. 4

The last prostate patient No. 4 was built up of 120 slices in the CT data set. Excessive heavy attenuation is visible in this patient clearly, due to both artificial hip present in this patient data, appendix No. 4. Just like previous patients, 0°, 45°, 180° and 315° beams were used. Due to heavy noise and organ corruption, last 3 beams contain 45 deg./rt, 45deg./lt and 60deg./out wedges accordingly. For this patient the 3D dose was slightly above the recommended values, 109.2%. This is due to huge corruption by the x-ray attenuation to the pelvic area.

2.4.5 Patient No. 5

The cervix-uterus case consisted of 74 slices. Right hip prosthesis was present in this patient. Excessive attenuation was cast from the prosthesis-hip towards the cervix-uterus. Intraperitoneal muscle, as well as right side fallopian tubes (visible calcification area), received significant edge deletion. Post filtering images display significant reduction in noise, as well as edge enhancement around the bladder and cervix-uterus areas, appendix 5. The RT plan was made according to the guidelines, using the in-verse prostate type technique, where total radiation dose of 46 Gy, 2 Gy per fraction, with beams distributed over 6 angles. Beams for all of the Cervix-uterus patients were placed at: 0°, 45°, 135°, 180°, 225°, 315° angles. For this patient, wedges of 15°/rt, 15°/lt and 30°/out were placed at the last 3 angles, to reduce irradiation to the rectum and sensitive OAR's as much as possible. The overall achieved 3D dose to the patient was 94.7%, slightly lower than the recommended guidelines due excessive shadow cast to the cervix-uterus organ, as well as patient topographical anatomical OAR locations in close proximity to the uterus-cervix.

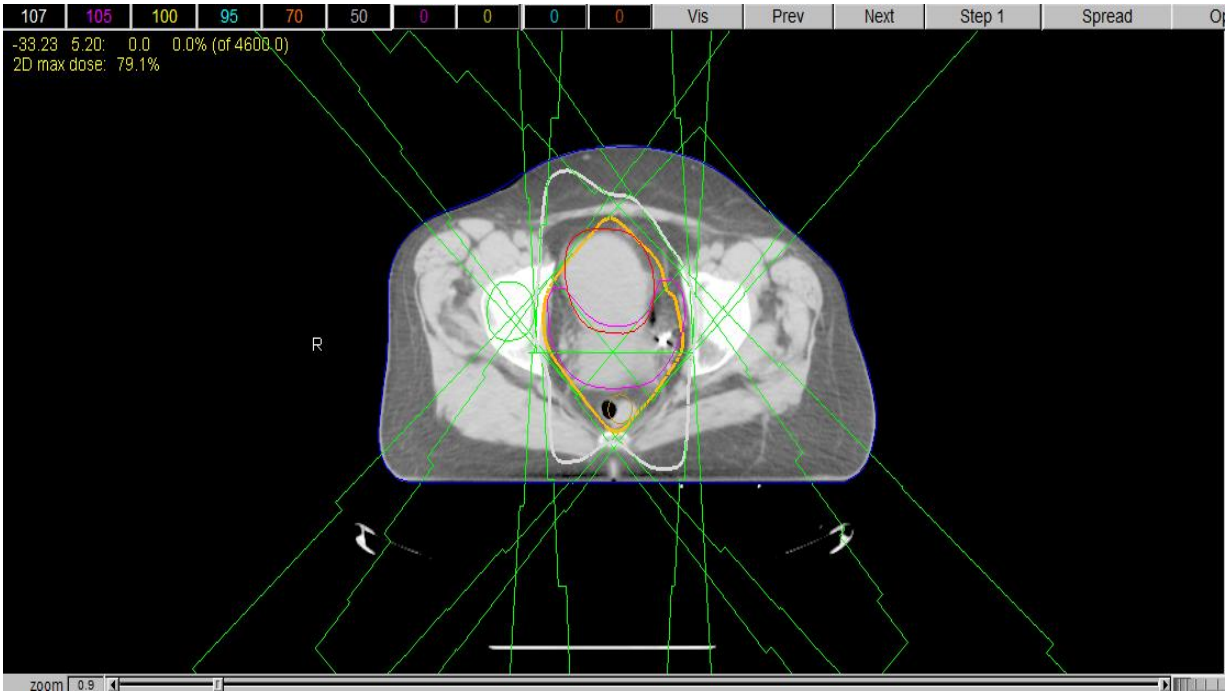

Fig. 25. Patient No. 5, RT planning, cervix-uterus projection

2.4.6 Patient No. 6

Patient No 6. Consisted of 108 slices in the whole data set. In this patient right hip-prosthesis was present. Just like the previous patients, x-ray attenuation cast has protruded in to the right side of the uterus, and noise is elevated heavily in this patient's data. This was possible to reduce slightly using the MAR algorithm. Like previously, same planning technique was used for this patient. The achieved 3D dose was 107.8%, slightly above desired threshold. Beams were placed at the same exact angles as the previous patient No. 5. Wedges were placed at beam angles of 0° 135°, 180°, 225°. The wedges in this case were selected: 15 deg./in, 30 deg./lt, 30 deg./out, and 30 deg./lt.

2.4.7 Patient No. 7

In this patient, heavy attenuation is present in both replaced artificial hips. Similar to patient No. 4, shadow is cast for both cervix-uterus and bladder organs. This patient has resulted in the highest levels of noise and image corruption out of all of the patients, appendix No. 7. The image edges to some organs are corrupted to the point of irreversible proportion. This however, using the MAR algorithm was possible to reverse to some extent, as the edges post-filtering become clearer. Without MAR application, original image RT planning would be almost in-conclusive, because organ bounds are difficult to make out. Using the filtered images RT plans were made for both of the data sets. Due to this corruption, the guidelines values for any of the organs were non-possible to achieve, using the previously used 6 beam angle technique. The overall 3D dose for this patient was 111.2%, a lot higher than desired. Additionally wedges for all of the posterior beams at 60 deg. were used to reduce OAR irradiation.

3. Results

3.1 Edge enhancement

To determine edge drift in filtered CT images, slices containing bladder bounds were investigated. Measurements were done across the patient's pelvis in the horizontal projection, due to most of the hip prosthesis artifacts casting shadows towards the center of the lower pelvis. In most cases, this results in deletion around the edges in the original images. For most of the original CT image data sets, bladder edges had to be approximated, as edge measurements tend to be highly inaccurate in error-affected slices. For patient No. 1, the average approximated bladder diameter was measured to be 5.62 cm. The filtered CT data set has enhanced the deleted bladder bounds, and measurements that are more accurate were possible because of this. The real bladder bounds were measured to be approximately 6.05 cm., a change in bladder diameter of 7.65% was determined for this patient. For patient No. 2, right hip prosthesis was present, therefore the right side of the bladder, side closest to the prosthesis "shadow-cast side", had to be approximated. The original patient data set has displayed a bladder diameter of 7.32 cm. while the filtered images have shown a more accurate value of 8.01 cm. This patient has resulted in a 9.42% edge drift. Patient No. 3 consisted of right hip prosthesis artifact, with only a very slight bladder's right edge corruption. The original data set wall diameter was measured to be 6.4 cm., while the more accurate enhanced image diameter was determined to be 6.65 cm. A change of 3.9% was determined for this patient. In patient No. 4, right hip prosthesis induced heavy attenuation was heavily present. This has resulted in edge deletion in both right and left sides of the bladder. Both sides' edges had to be approximated for most slices in the pelvic region. The original data set has shown a diameter of 7.03 cm., while the filtered data set edges were slightly drifted, enhancing additional edges. This measured edge drift diameter was around 7.87 cm., a substantial 11.94% difference in the diameters was concluded for this patient. In patient No. 5 data, right hip prosthesis presented with left bladder wall deletion around the edges. Original diameter was measured to be 8.64 cm., while filtered diameter – 8.88 cm. Only a very slight edge drift of 2.77% was determined for this patient. For the next patient, the data contained both hip prosthesis with heavy attenuation in the pelvic region. Despite this, a relatively accurate approximation was possible for the original patient No. 6 data set. The resulting edge shift was estimated to be in a relatively high accuracy compared to the original edges, a 2.11% difference was determined. The edge diameters for this patients were 6.16 cm., and 6.29 cm., for original and filtered CT data set edges accordingly. In the last patient No. 7, both hip prosthesis were also present with heavy bladder edge-approximation necessity in this case. The original CT bladder diameter was measured to be 10.53 cm., while the filtered diameter – 10.31 cm., a difference of 2.08% was determined when comparing both CT plan edges. In general, it is safe to assume that edge enhancement provides us with more accurate values of the edges than they were approximated initially. On average, edge drifting MAR filtering algorithm can provide us with a change of approximately 5.1% across all patients.

Table 3. Patient CT post filtering edge shift

Patient No.	Original image diameter (cm)	Filtered image diameter (cm)	Change (±%)
1.	5.62	6.05	7.65
2.	7.32	8.01	9.42
3.	6.4	6.65	3.9
4.	7.03	7.87	11.94
5.	8.64	8.88	2.77
6.	6.16	6.29	2.11
7.	10.53	10.5	2.08
			Average: 5.1

3.2 RT doses

The pre-RT filtering algorithm (MAR algorithm) in general can provide us with a great possibility for dose optimization to the original RT plan. When creating an RT plan for the patient, errors become more apparent. This is expressed more easily with the MAR application, when comparing the original images with the filtered ones. Lots of information is typically misinterpreted or lost in RT plan creation, when plans are being built on x-ray attenuated images. In all 7 of the patient data, anatomical structure enhancement and heavy noise reduction is visible. Despite x-ray attenuation, RT plans as close as possible according to the reference guidelines had to be created, in order to investigate dose reduction in MAR filtered CT plans.

3.2.1 Patient No. 1

For this patient, comparing the original CT RT plan with filtered CT RT plan, it is clear that, all of the values are in the required threshold bounds. The target – prostate received at least 95% of the dose as required by the guidelines, in our case 78.16 Gy. The OAR (organ's at risk) values were also in the desired thresholds. For rectum, 50% of the volume received 35.16 Gy, 35% volume was receiving 44.2 Gy of the dose, and 10% volume received around 65.55 Gy dose. When taking a closer look at another important OAR – bladder, once again, values are in the desired thresholds. 50% of the volume received 15.13 Gy of dose, additionally 35% and 25% volumes are receiving 44.79 Gy and 59.09 Gy accordingly. 15% bladder volume received 59.09 Gy of dose. In this and all of the following CT RT plans, femoral heads that are present receive a lot less dose than the required 10% of the prescribed treatment dose. Additionally, artificial hip replacement deprives us of a possibility of proper femoral head evaluations, therefore evaluations of this OAR can be ignored.

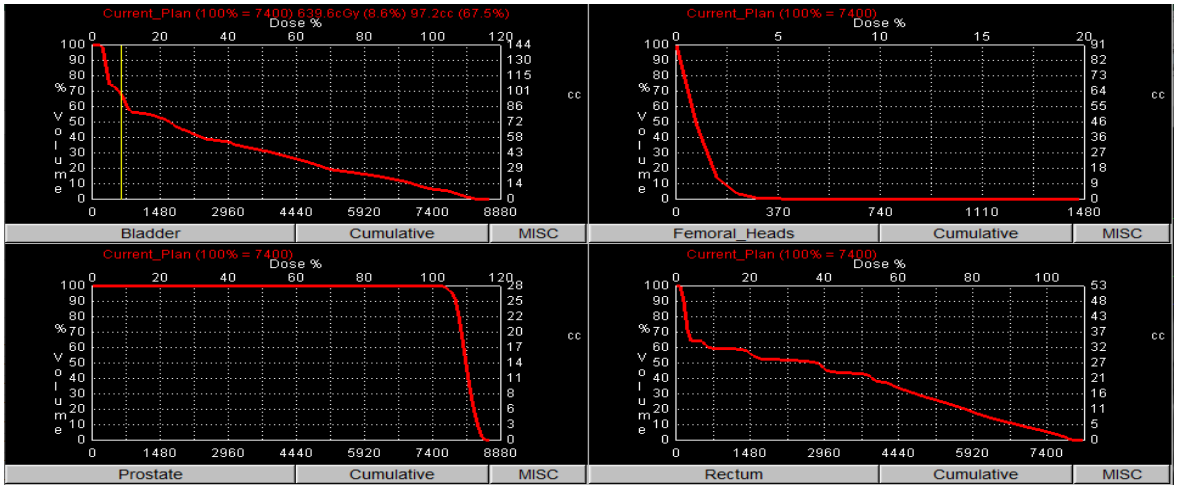

Fig. 26. Patient No. 1 original CT scan DVH values

The filtered CT image DVH (dose volume histogram) values can be seen reduced through out all of the organs. The steep prostate dose curve drift expresses a new 95% volume value of 73.92 Gy. The OAR rectum 50%, 35%, 10% volumes doses are receiving 22.37 Gy, 37.42 Gy and 62.91 Gy. Bladder 50%, 35%, 25% and 15% volumes in the filtered CT data set receive 16.05 Gy, 29.89 Gy, 42.27 Gy, and 58.78 Gy accordingly. From the new DVH values it is seen that, the RT plan was optimized when MAR algorithm was applied reducing the organ received doses.

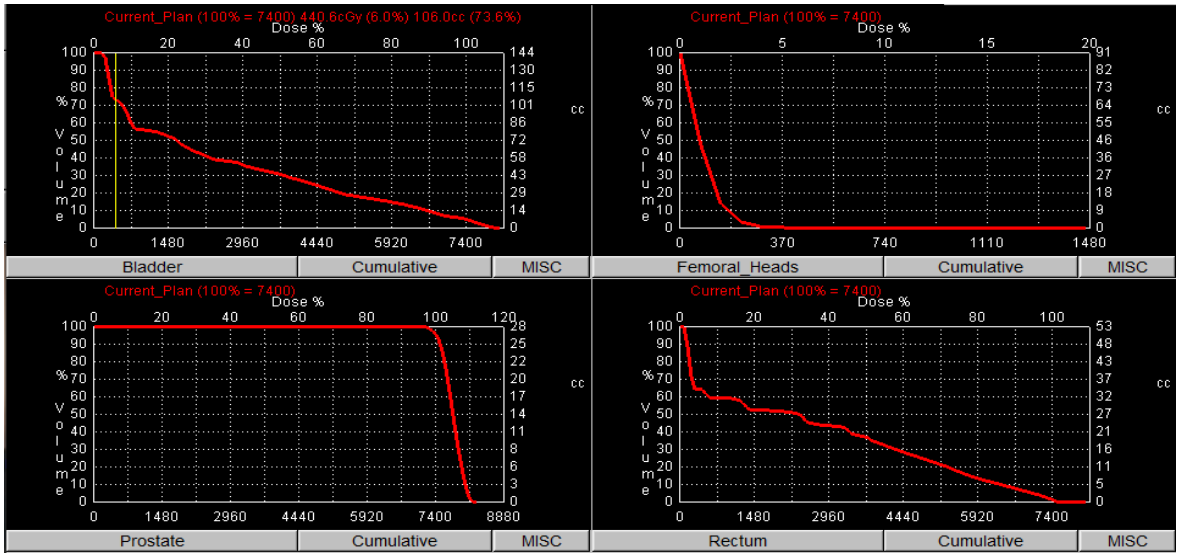

Fig. 27. Patient No. 1 filtered CT scan DVH values

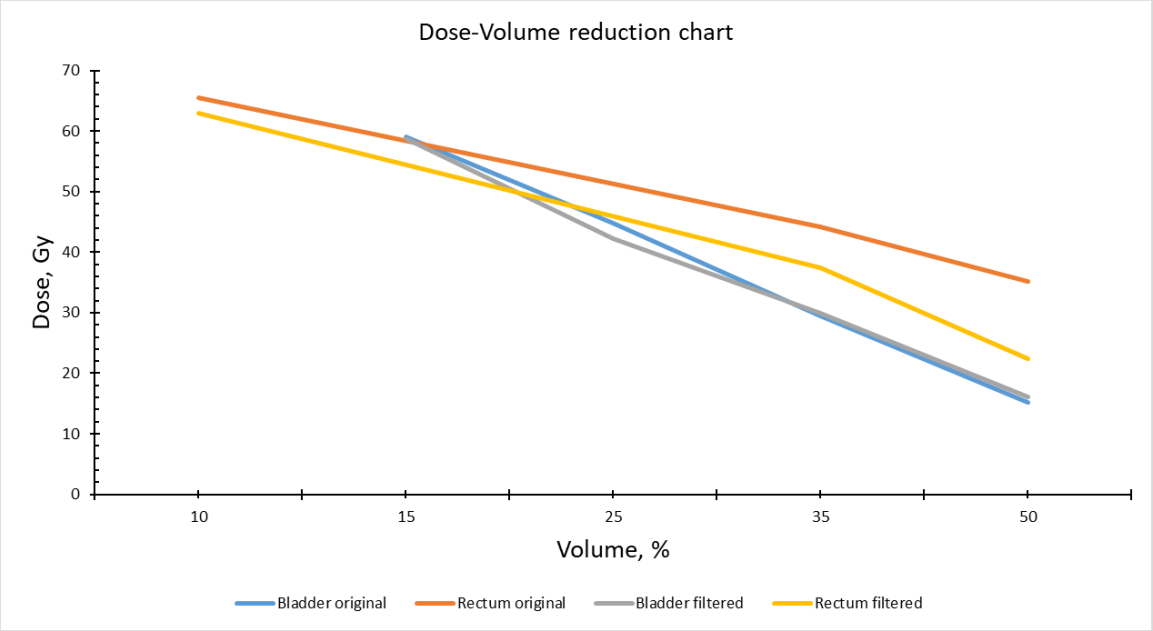

Fig. 28. Patient No. 1 dose-volume reduction chart

For patient No. 1 a reduction of 5.42% to the target organ was determined after the MAR algorithm. Additionally, rectum average dose reduction for all the mentioned volumes is 4.69%, while average bladder volume dose on the contrary is seeing a slight 0.37% increase.

3.2.2 Patient No. 2

For the original image CT RT plan, all of the dose values are in the required threshold bounds, except for a slight 95% dose misalignment of 0,4% - 67.89 Gy dose, due to RT plan optimization caused by heavy artifact presence. The other OAR values however are in the desired threshold bounds. For rectum, 50% of the volume receives 42,5 Gy, 35% is receiving 44,3 Gy of the dose and 10% receives around 62,3 Gy of the dose. In this patient case, bladder, once again displays threshold values, with 50% of the volume receiving 7,7 Gy of the dose, additionally 35% and 25% volumes receiving 22,1 Gy and 43,1 Gy, and 15% volume dose being 46.32 Gy.

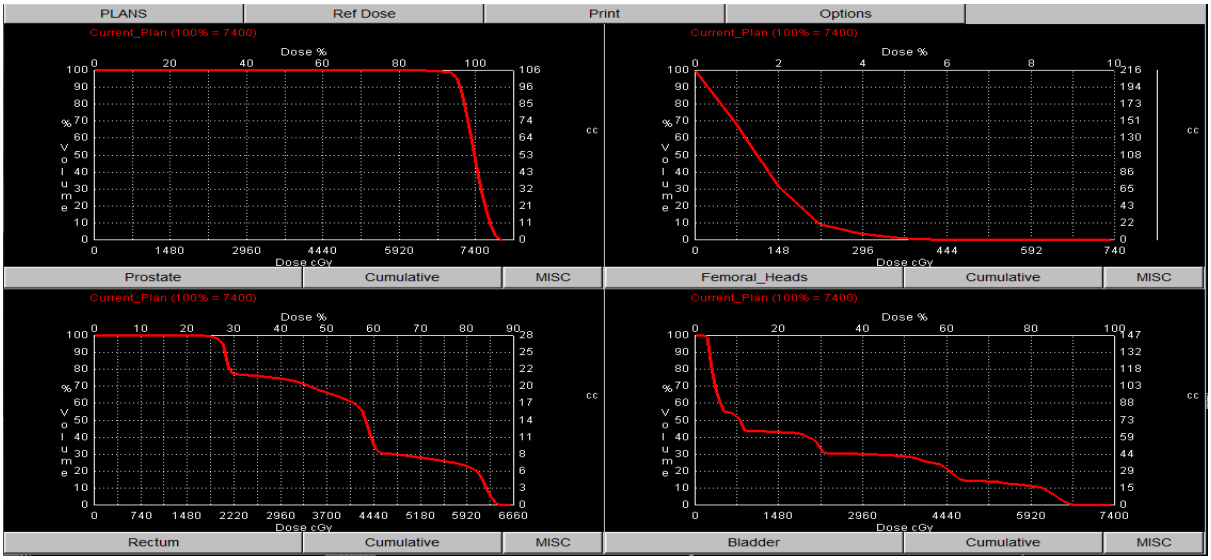

Fig. 29. Patient No. 2 original CT scan DVH values

The MAR algorithm displays a new 95% dose decrease. The new value is 66.52 Gy. When comparing OAR values of the original DVH with filtered DVH values, this time, rectum volumes of 50%, 35%

and 10% are receiving 47,4 Gy, 49,6 Gy and 65,8 Gy accordingly. These values show a slight 1-4 Gy increase in all of the doses, due to re-distribution of the edges and attenuation values. Despite this, the values are still in the desired threshold bounds. For Bladder OAR 50%, 35%, 25% and 15% volumes display 9 Gy, 26,5 Gy, 44,6 Gy and 52.3 Gy values accordingly. This patient again results with an approximate 4 Gy increase to this organ. The main reduction is visible in the target organ, as the curve of the DVH is a lot steeper in the original DVH. This indicates that the filtered RT plan has the potential to be optimized further, with potential OAR dose re-distribution.

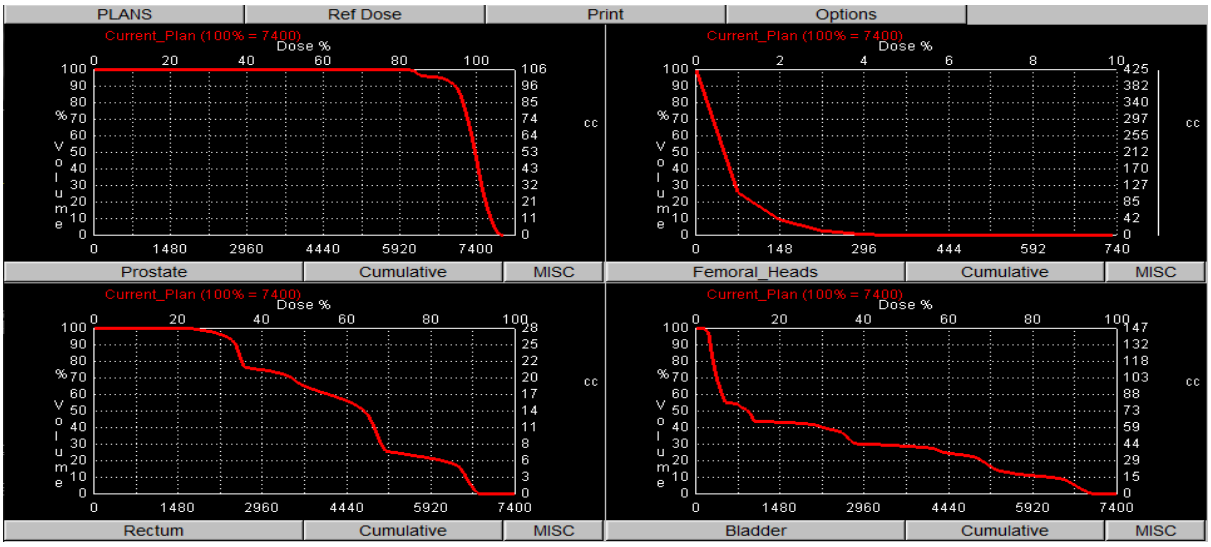

Fig. 30. Patient No. 2 filtered CT scan DVH values

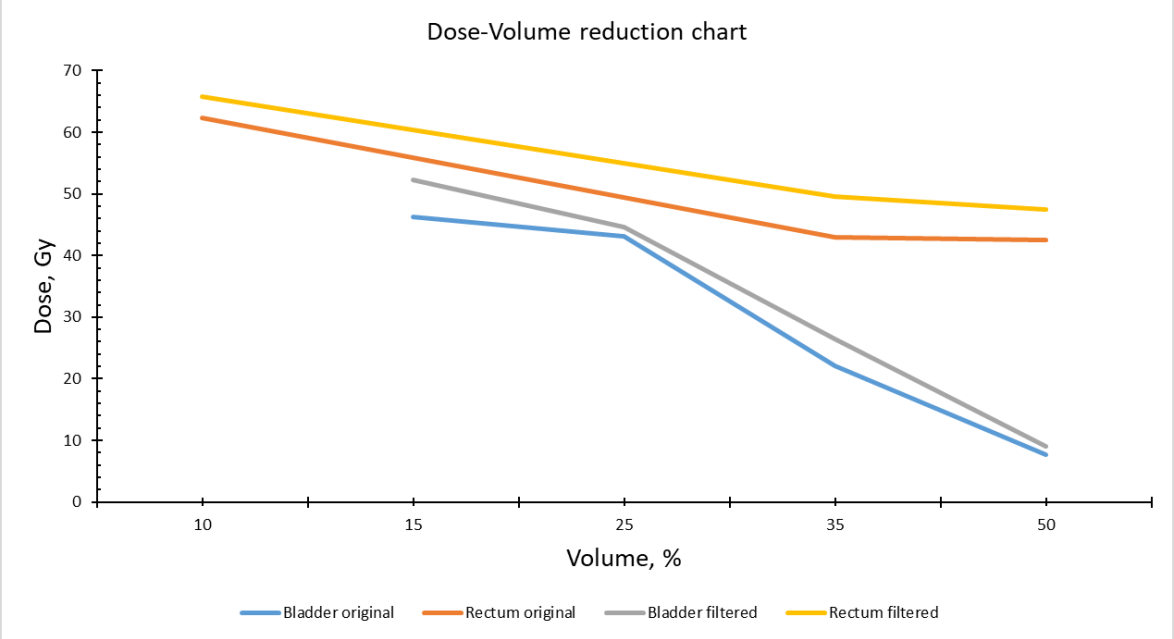

Fig. 31. Patient No. 2 dose-volume reduction chart

For patient No. 2 a reduction of 2.02% to the target organ is present after the MAR algorithm. A dose increase of 9.7% for the rectum and 13.3% to the bladder on average are present in this CT case. This can be explained by very heavy attenuation to the pelvic area, and that the MAR filtering algorithm redistributes the organ edges along with reducing the noise heavily. These results indicate further nessesity of the RT plan optimization under MAR filtering application.

3.2.3 Patient No. 3

In patient No. 3 CT images, the initial target dose at 95% volume was measured to be 72.86 Gy, which is in the desired threshold for the prostate target. For rectum organ, the measured 50%, 35% and 10% volume doses were measured to be 66.9 Gy, 70.65 Gy and 72 Gy. These values are slightly above the threshold-desired values due to CT image heavy attenuation in the pelvic region approximate to this organ. Values as close as reasonably possible were achieved when creating the RT plan to counter this percentage error. Bladder in the original CT data at 50%, 35%, 25% and 15% volumes display 10.71 Gy, 21,6 Gy, 36.93 Gy and 55.14 Gy doses. All of these values are in the desired threshold bounds according to the guidelines.

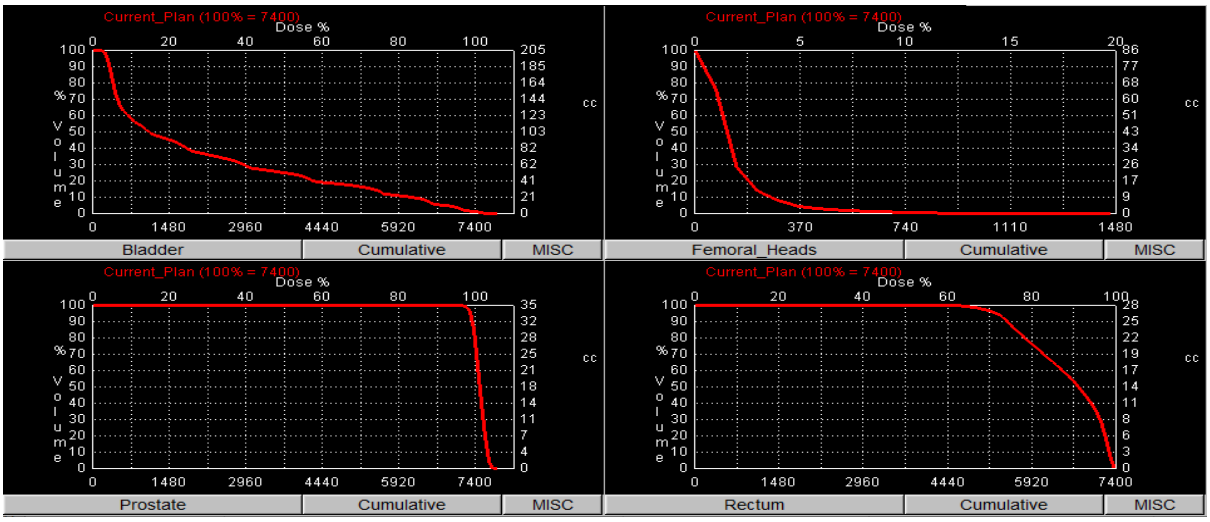

Fig. 32. Patient No. 3 original CT scan DVH values

The filtered MAR algorith values for this patient show very slight reduction in the target dose, 72.72 Gy. The rectum OAR for the previously mentioned volumes show new doses: 65.8 Gy, 61.1 Gy and 71.9 Gy. News bladder volume dose values are 9.99 Gy, 22.12 Gy, 37.18 Gy and 54.8 Gy.

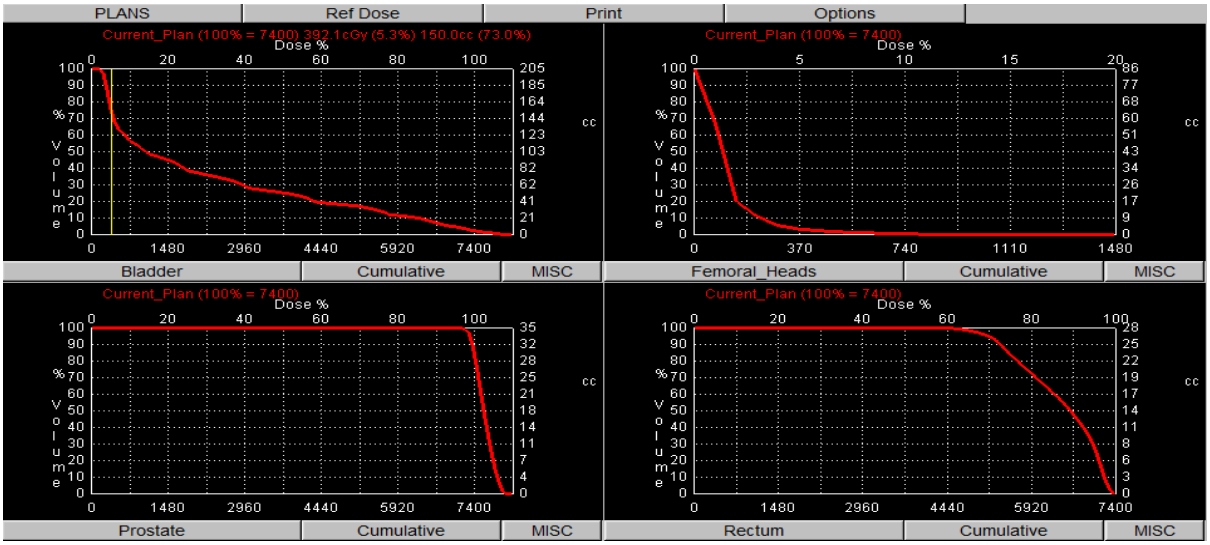

Fig. 33. Patient No. 3 filtered CT scan DVH values

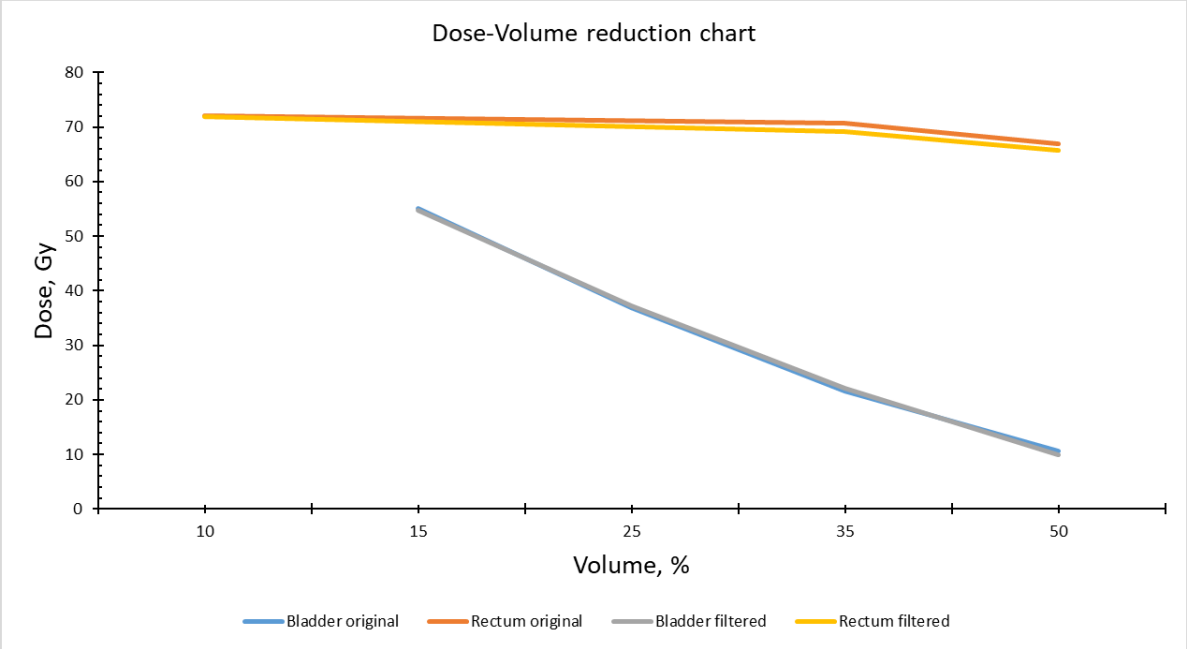

Fig. 34. Patient No. 3 dose-volume reduction chart

For this patient only very slight reduction was visible post MAR filtering. The biggest diference is visible in the rectum OAR, with the average volume reduction being 1.33%. The Bladder organ dose has seen less reduction, only 1.06%. The target RT dose reduction for this patient was calculated to be 0.19%. This patients data suggests that not many edges of interest around bladder and prostate were enhanced when the MAR algorithm was applied, additionally less than usual ammount of noise could have been present in the area of interest. This resulted in this Patient's MAR application manifesting in the lowest % dose change in all of the patients.

3.2.4 Patient No. 4

The last prostate patient original CT data set displayed 72.91 Gy dose to the target. The rectum organ at risk doses for the previously mentioned volumes in this case were: 66.24 Gy, 71.12 Gy and 73.5 Gy. The bladder values in our case are in the desired threshold, and are as follows: 8.94 Gy, 22.14 Gy, 36.87 Gy and 56.14 Gy. All of these values are slightly above the threshold due to quite heavy attenuation to the pelvic region in this particular prostate case.

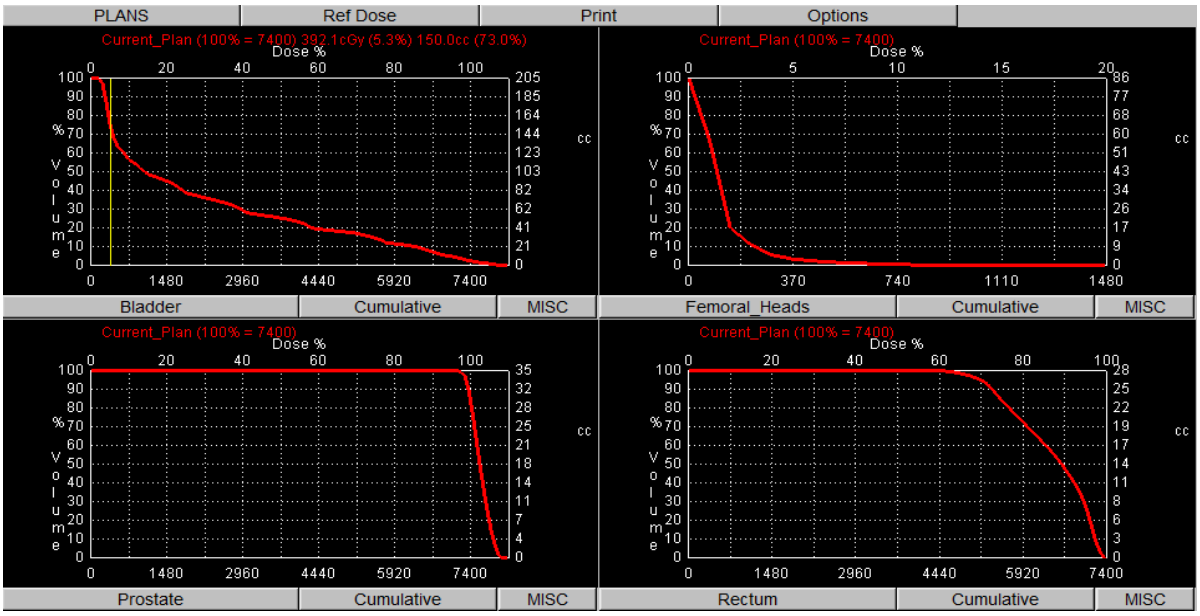

Fig. 35. Patient No. 4 original CT scan DVH values

The new filtered dose curves are shifted only very slightly towards the left side in the DVH. A new 95% volume target dose of 72.1 Gy is registered. The new OAR values for rectum and bladder are: 66.03 Gy, 68.25 Gy and 73.01 for rectum, and 8.74 Gy, 28.06 Gy, 36.25 Gy and 59.85 Gy for bladder.

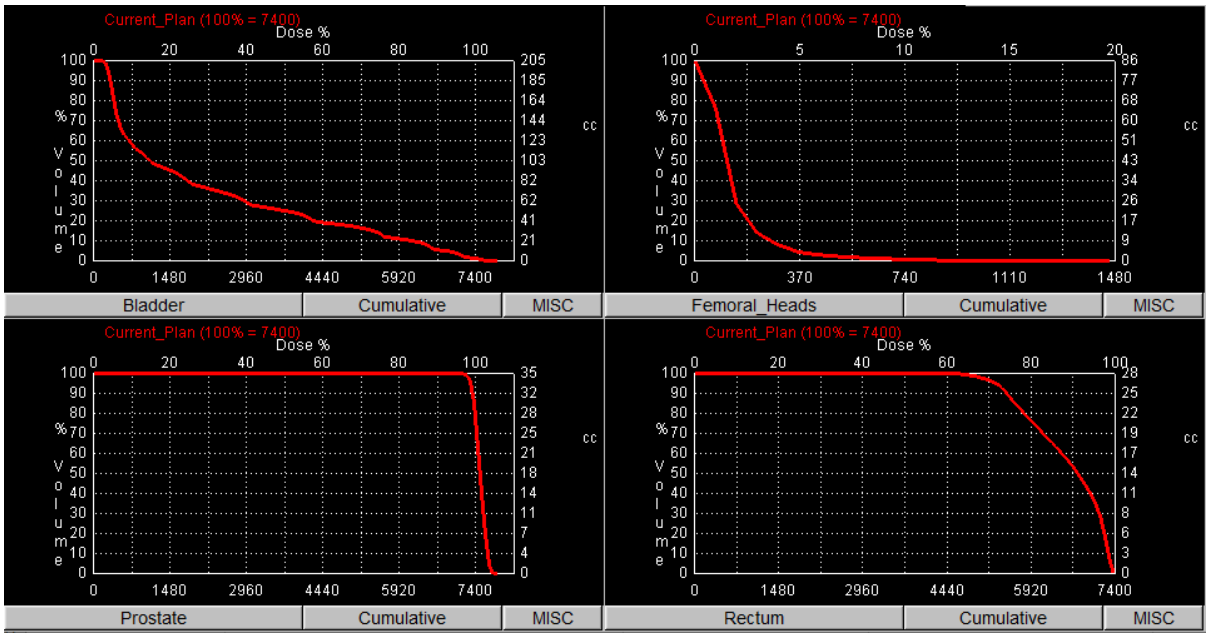

Fig. 36. Patient No. 4 filtered CT scan DVH values

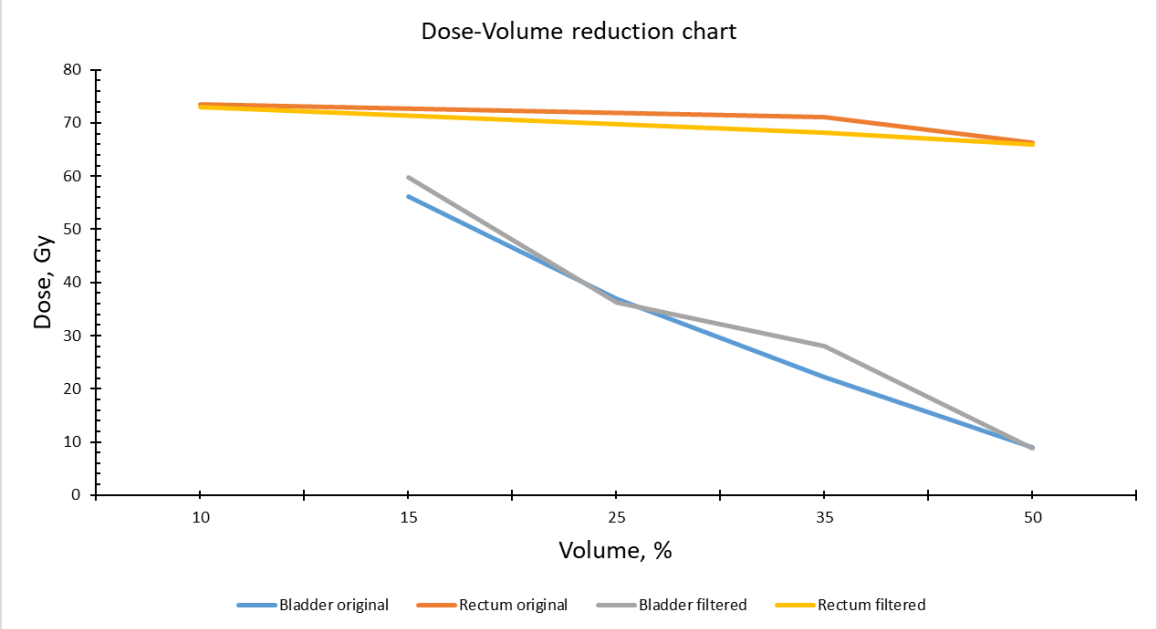

Fig. 37. Patient No. 4 dose-volume reduction chart

For this patient a target dose redution of 1.11% and rectum reduction of 1.67% are present, while bladder average dose seems to have seen a 7.35% increase.

3.2.5 Patient No. 5

Patient No. 5 was investigated as cervix-uterus case. Due to the topography of this area of interest, heavy attenuation is typically present around the uterus area. Bones of the small-pelvis, close to the uterus typically cast heavy shadowing, resulting in deleted uterus edges in CT images. The CT images

affected by hip prosthesis artifacts typically corrupt cervix-uterus cases even more. Due to this, original image optimisation is very challenging, with threshold dose achieval being very difficult. For this patient the original CT data set target dose for the 95% volume was measured to be 37.5 Gy. The OAR rectum values for this patient for 50%, 35% and 10% were measured as: 20.02 Gy, 34.5 Gy and 40.6 Gy. Bladder doses for 50%, 35%, 25% and 15% volumes are: 37.3 Gy, 37.9 Gy, 38.7 Gy and 39.8 Gy.

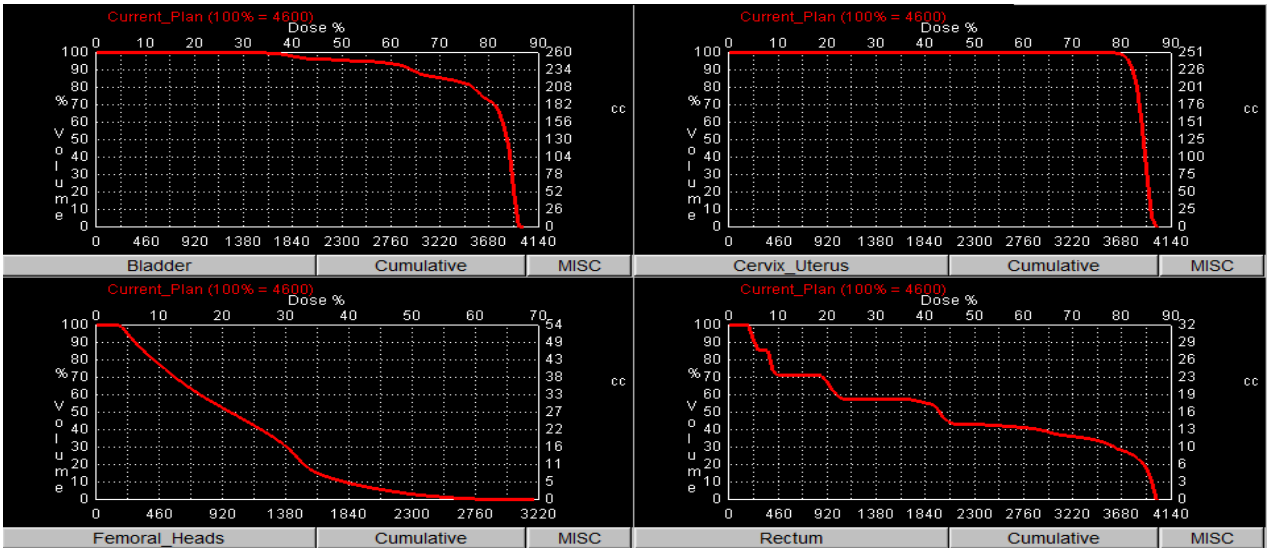

Fig. 38. Patient No. 5 original CT scan DVH values

The filtered RT plan 95% target dose as seen in the new histogram is 31.62 Gy. The previously mentioned volumes contain 18.4 Gy, 29.8 Gy and 36.17 Gy doses for the rectum. Bladder volumes-doses in the new DVH are: 30.82 Gy, 31.8 Gy, 32.2 Gy and 33.1 Gy accordingly. Both of the OARS are in the desired constraints post MAR application

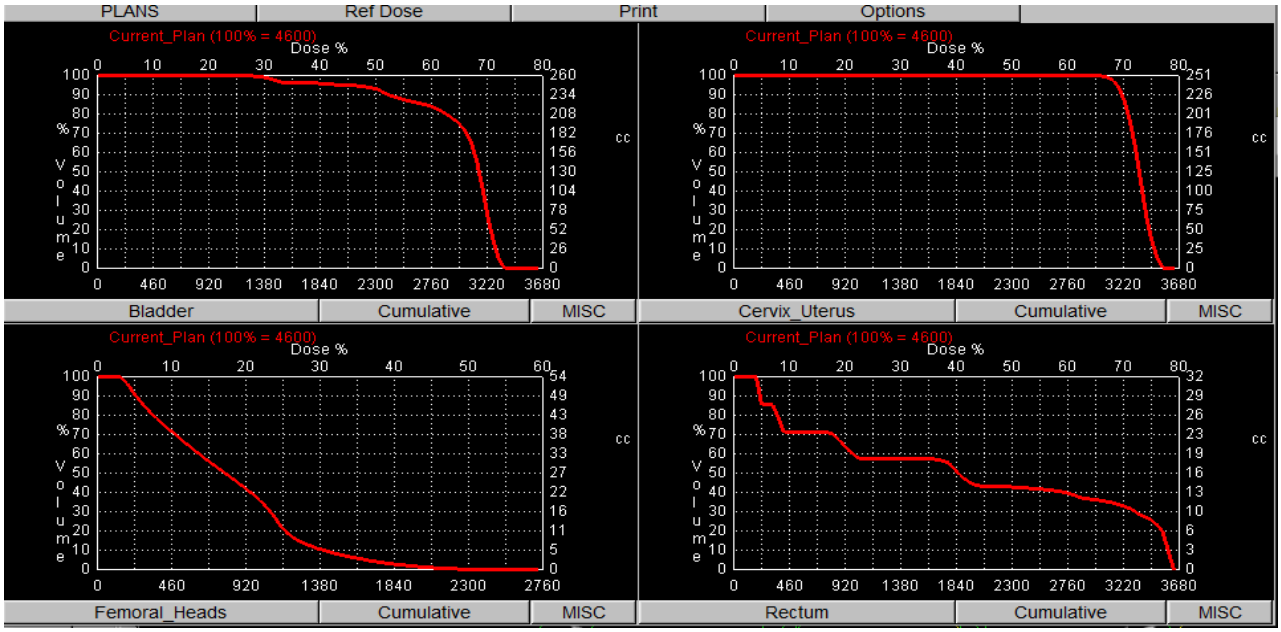

Fig. 39. Patient No. 5 filtered CT scan DVH values

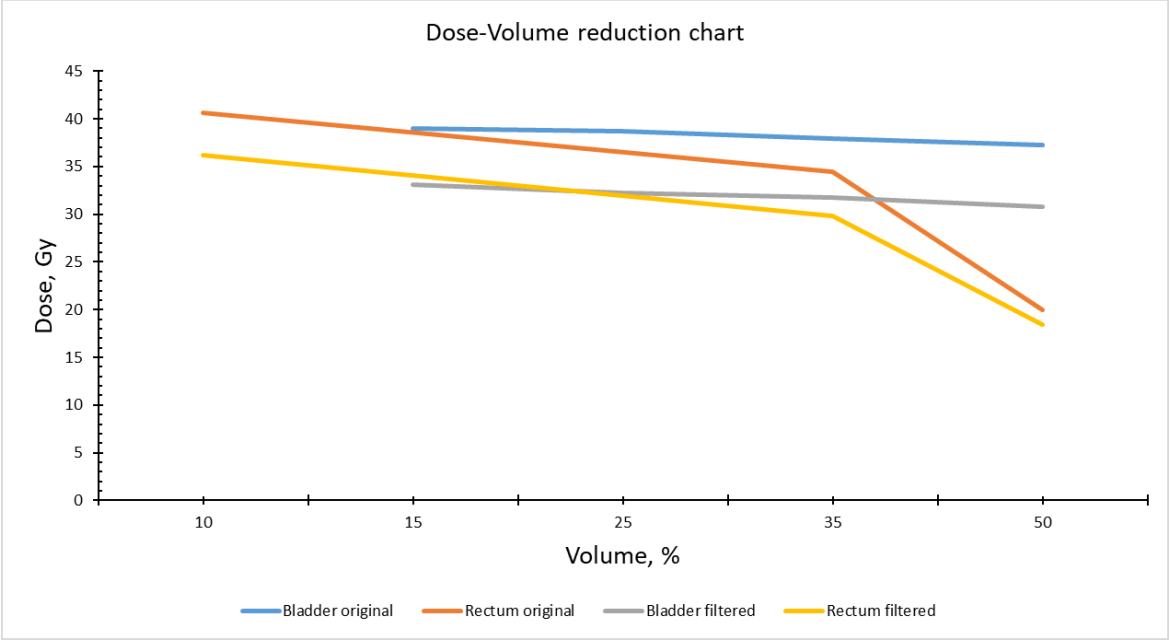

Fig. 40. Patient No. 5 dose-volume reduction chart

For patient No. 5, reduction in almost all volumes is visible. The initial 95% target volume dose after applying the MAR algorithm was reduced by 15.68%, while the average rectum and bladder dose changes for all volumes are: 10.88% and 16.35% accordingly. This could be explained by extreme x-ray attenuation in the original images, as the MAR filtering has re-distributed the edges a lot more closer to the presumed edge values. This has resulted in the biggest % dose reduction in all of the patient data sets.

3.2.6 Patient No. 6

Patient No. 6 consisted of another cervix-uterus dose investigation. In this patient, heavy edge missinformation and artifacts were present. This manifested itself in a substantial bladder edge deletion and heavy noise in the lower pelvis region. For the original CT data set 95% target, cervix-uterus, received a dose of 43.9 Gy. The OAR values for this patient were out of threshold by a small margin. The rectum doses for 50%, 35% and 10% volumes were: 48.67 Gy, 49.11 Gy and 49.8 Gy. A very steep bladder dose-volume curve is present in this case. The bladder OAR doses for volumes 50%, 35%, 25% and 15% are: 45.3 Gy, 45.4 Gy, 46 Gy and 46.02 Gy.

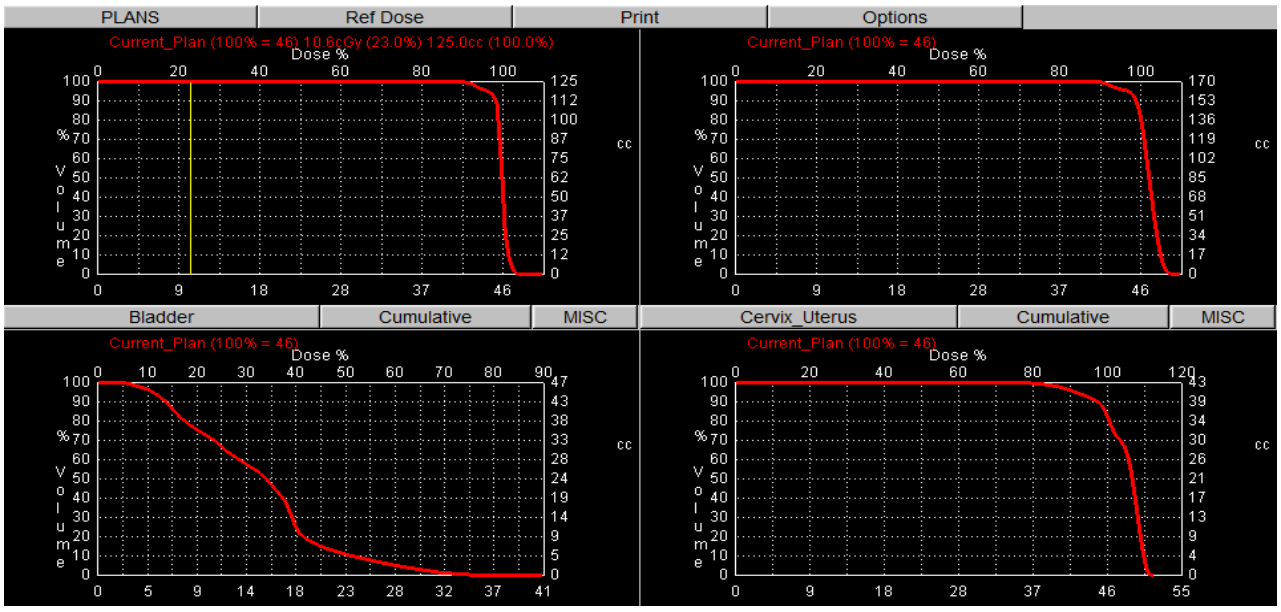

Fig. 41. Patient No. 6 original CT scan DVH values

After MAR algorithm was applied, the DVH values shifted indicating a RT plan optimisation. The new 95% target dose is 40.2 Gy. The previously listed doses for OAR‘s became 43.82 Gy, 46.01 Gy, 48.7 Gy for rectum, and 44,8 Gy, 44.9 Gy, 45.8 Gy and 46 Gy for the bladder.

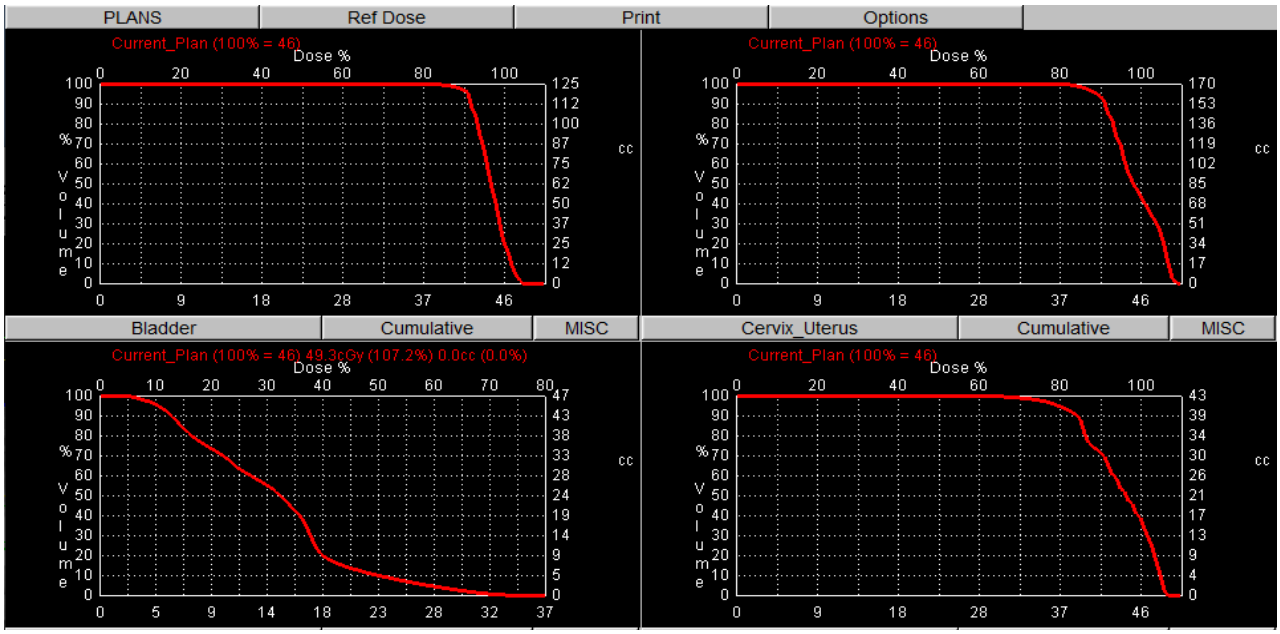

Fig. 42. Patient No. 6 filtered CT scan DVH values

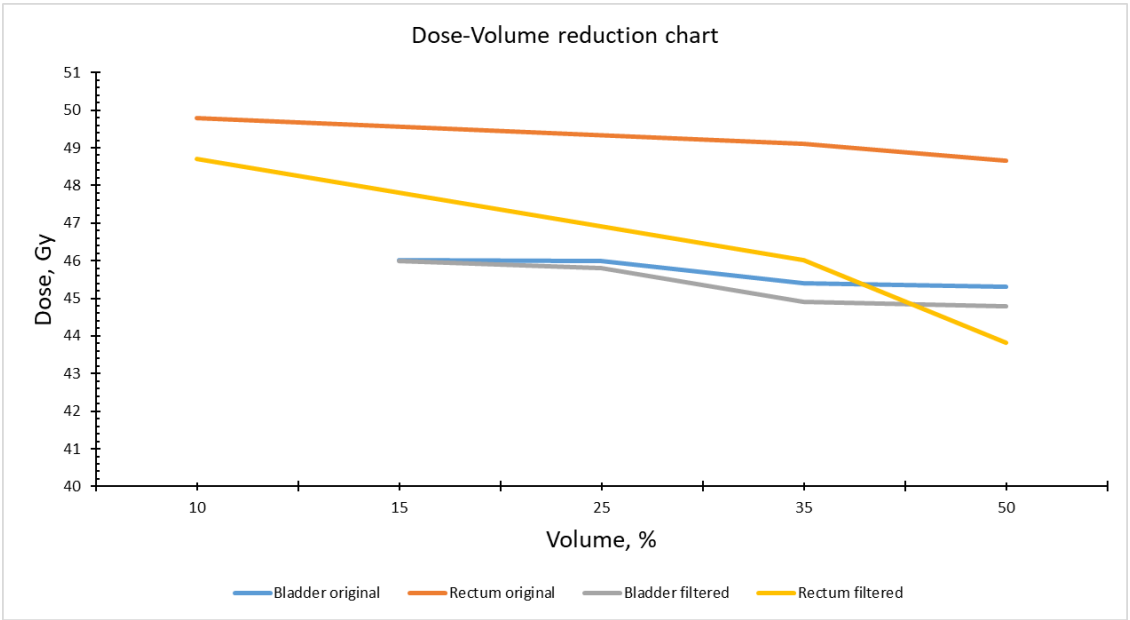

Fig. 43. Patient No. 6 dose-volume reduction chart

In this case a dose reduction of the target by 8.43%, along with rectum and bladder reductions of 6.16% and 0.67% are visible. This was possible to MAR algorithm reducing image noise significantly and enhancing the deleted bladder edges significantly in this particular case.

3.2.7 Patient No. 7

This patient suffered greatly from x-ray attenuation around the peritoneal and lower pelvic areas through out most of the slices. Both hips were replaced with artificial ones for this patient. Due to very heavy corruption of the CT data most of the values measured are above the desired thresholds. In this patient

the target 95% volume received dose is 38.5 Gy. Organs at risk like rectum at their according volumes and doses are: 50% 30.02 Gy, 35% 33.4 Gy, 10% 38.02 Gy. Bladder in this instance received doses for the according volumes: 50% 3.9 Gy, 35% 4.6 Gy, 25% 14.8 Gy, 15% 35.9 Gy.

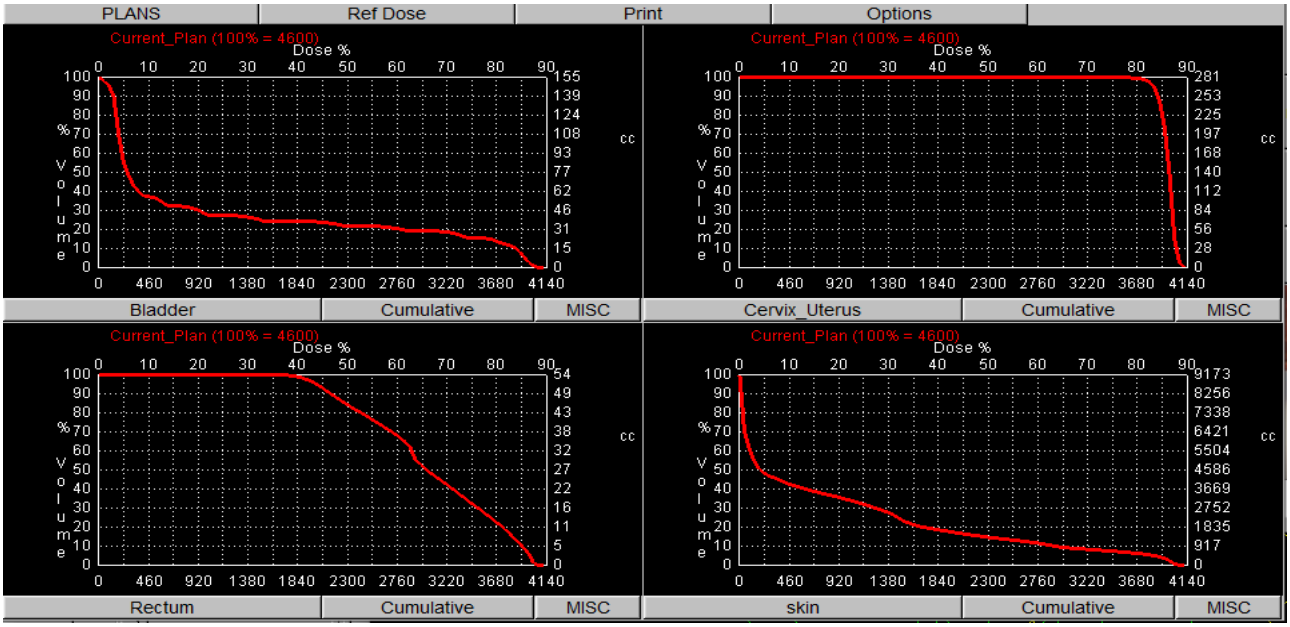

Fig. 44. Patient No. 7 original CT scan DVH values

From the filtered CT scan a new 95% DVH value can be seen, 31.25 Gy. A substantial reduction to the target. For rectum volume 50%, a reduced dose of 27.8 Gy is present. 35% volume contains 29.01 Gy dose, and 10% volume has 33.8 Gy dose to these volumes. All volumes of the rectume resulted in reduced dose for this OAR. For bladder the volume-dose values re-distributed are: 50% volume 3.63 Gy, 35% volume 4.48 Gy, 25% volume 11.4 Gy, and 15% 32.2 Gy.

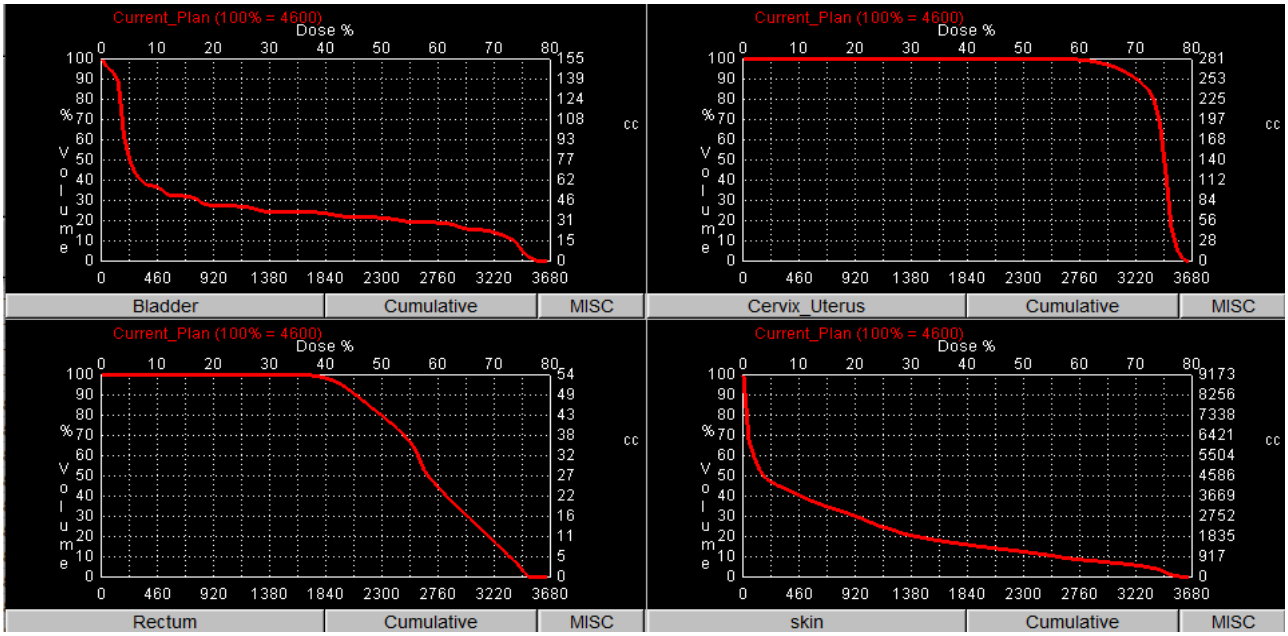

Fig. 45. Patient No. 7 filtered CT scan DVH values

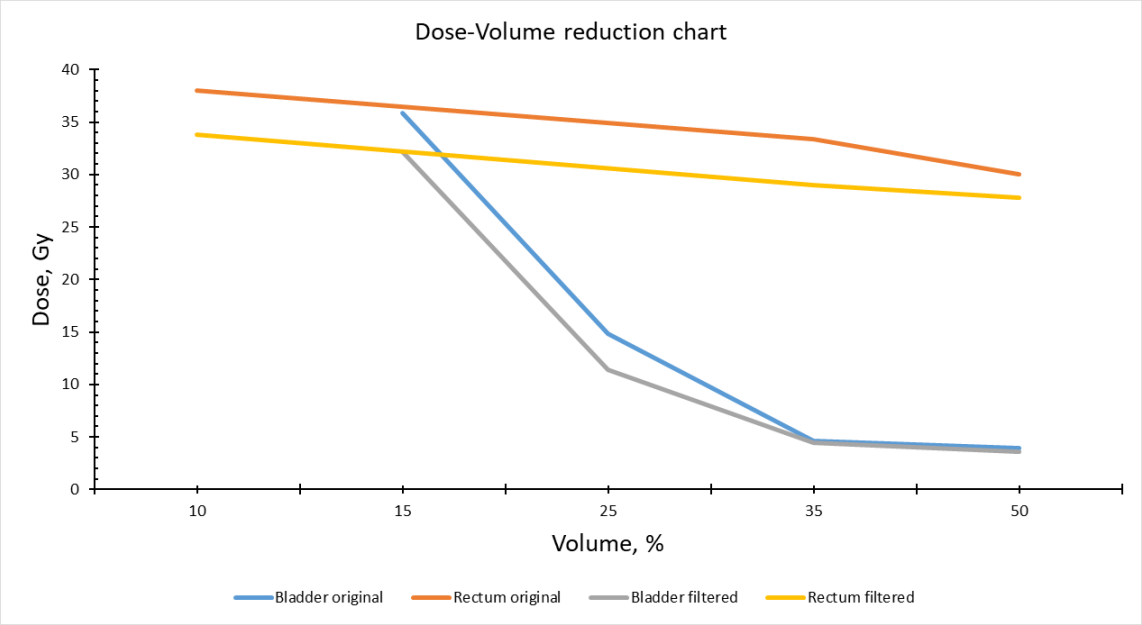

Fig. 46. Patient No. 7 dose-volume reduction chart

In the end, for this patient a reduction to the target 95% volume of 18.83 % reduction is present. Rectum dose reduction of 10.54%, and bladder dose reduction of 10.7% is present.

3.3 General doses

As a better way of data representation, all of the previous patients have been grouped in to two groups. Prostate group and Cervix-uterus group. For the first group, data volume-dose investigation displays an average reduction of 2.6% to the target organ-prostate. In the data it is apparent that, on average, through out all of the prostate patients, for rectum OAR, the reduced dose by the MAR application for all of the volumes is approximately 2.21%. Contrary to this, a slight increase by an average of 4.45% to the bladder is visible through out this group. Originally the prostate patient group suffered from slightly less x-ray attenuation, as a result of this, average dose shifts are relatively smaller when comparing them to the other group of patients. The average increase in bladder re-distributed dose could suggest that further RT plan optimisation is indicative for proper-real prostate plan evaluation, as the doses re-distribute according to the organ edge shift significantly, according to the cavity theory used by the RT planning systems.

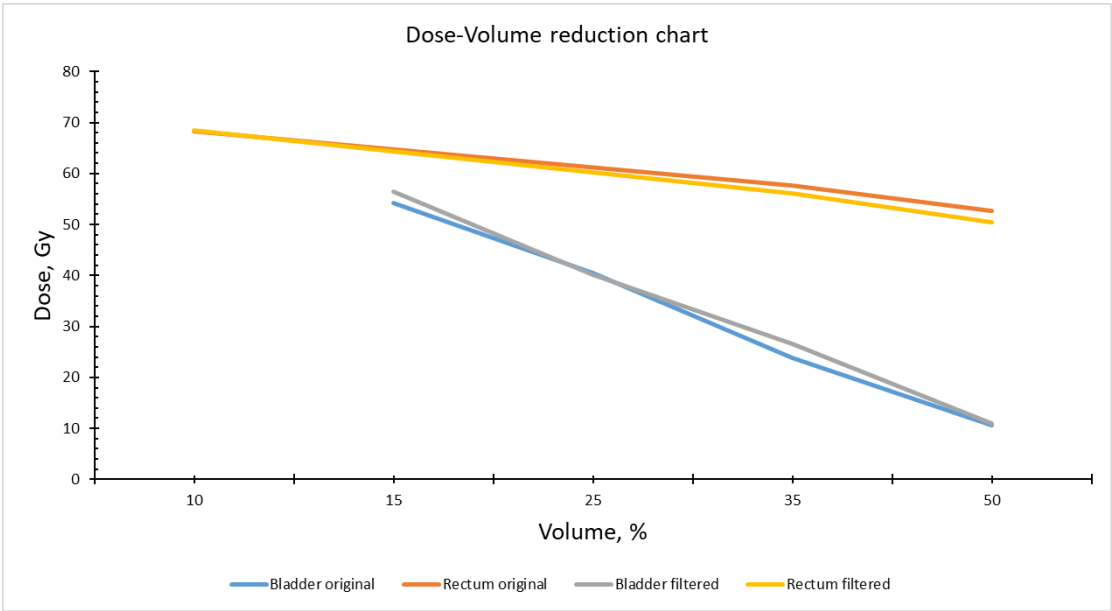

Fig. 47. Prostate group dose-volume reduction chart

The second group of patients seem to have received a higher ammount of dose re-distribution. For all of the organs the registered doses seem to have been reduced. The main target Cervix-uterus reduction on average for the whole group is around 14.03%. The rectum and bladder have also seen significant reduction, 8.94% and 6.59% accordingly. This substantial reduction in doses for these patients could be explained by originally higher volumes of the target organ, as well as the whole group containing heavier x-ray attenuation in the original CT images. MAR algorithm suggests higher dose reduction, the higher the % error is in the CT scan slices. These reduction numbers are promissing and are also indicitive to further dose optimization possibility for these patients.

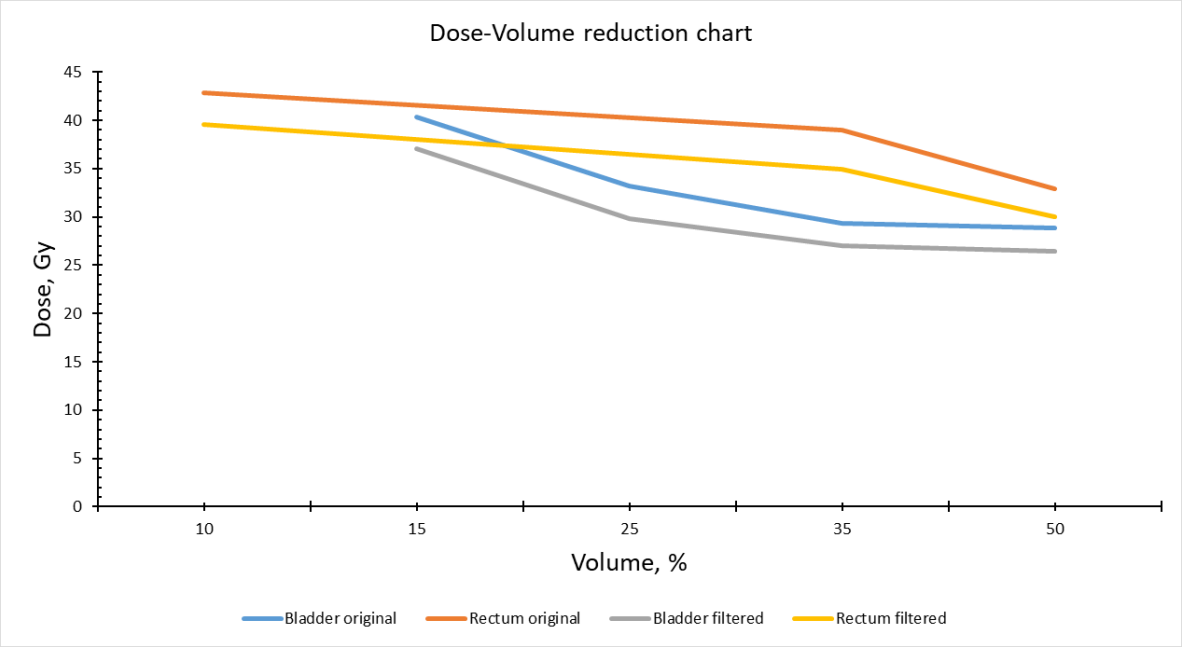

Fig. 48. Cervix-uterus group dose-volume reduction chart

Conclusions

1. The investigation of the possible CT filtering methods showed that, the different filter applications working together can make up algorithms, which are capable of detecting large range of deleted edges in CT images affected by noise or x-ray attenuations. A significant soft tissue and organ-edge enhancement has been indicated after filter applications in all investigated patients, providing unique possibility of radiation treatment plans optimization.
2. It was found that there is a significant change in organ edges after computed tomography data was subjected to metallic artifact reduction algorithm application. Going through all patients computed tomography slices, recording the bladder image, the edge change resulted in 5.1% of the edge drift as compared to the original organ diameter in the original non-filtered CT studies.
3. Performed investigation has shown that application of filtering algorithm resulted in significant dose reduction for both patients groups: female patients with cervix- uterus cancer and for male patients with prostate cancer. 2.6% reduction of dose to the target organ was indicated for prostate cancer patients. In addition to this, the dose changes to organs at risks like bladder and rectum were observed as well. Rectum irradiation dose was reduced by 2.21% while the dose to bladder was increased by 4.45%. For the cervix-uterus cancer group a substantial dose reduction to the target organ of 14.03% was achieved. Irradiation dose to rectum and bladder was reduced by 8.94% and 6.59% correspondingly. Estimated dose changes are indicative to further radiotherapy treatment plan optimization.

Acknowledgements

I would like to express my gratitude to Prof. Diana Adlienė and Assoc. Prof. Dr. Jurgita Laurikaitienė who have made my project possible. They have given me valuable advice and provided me with tools and knowledge necessary for radiotherapy planning investigations.

List of references

[1] VASPVT, Kompiuterinis tomografas. Valstybinė akreditavimo sveikatos priežiūros veiklai tarnyba prie Sveikatos apsaugos ministerijos, 2014, Vilnius, p. 4.

[2] European union statistics department, Healthcare resource statistics – technical resource and medical technology, 2020, p. 5.

[3] Sprawls. P, Physical principles of medical Imaging, Medical Physics international journal, 1995, p. 167-170.

[4] Kataoka. M. L., Hochman. M. G., Rodriguez. E. K., Paul-Lin. P. J., Kubo. S., Raptopolous. V. R., A Review of Factors That Affect Artifact From Metallic Hardware on Multi-Row Detector Computed Tomography, MedlinePlus, 2010, p.125-135.

[5] DiSaia. P, Creasman. W., Clinical Gynecology – Oncology, 8th. Edition, Elsevier inc. 16. Complications of disease and therapy, 2012, p.479-513.

[6] M. J. Willemink, P. B. Noel, The evolution of image reconstruction for CT—from filtered back projection to artificial intelligence, european radiology publications, 2018, p. 4

[7] F.E.Boas, D.Fleischman, CT artifacts: Causes and reduction techniques, Department of Radiology, Stanford University School of Medicine, 2012, p. 5.

[8] Avinash C. Kak, M. Slaney, Principles of computerized tomographic imaging, Institute of engineering and electronics, 1999, p. 49-80

[9] M.T. Al Hussani, M.H. Ali Al Hayani, The Use of Filtered Back projection Algorithm for Reconstruction of tomographic Image, Al-Nahrain University, College of Engineering Journal (NUCEJ) Vol.17 No.2, 2014, p.151-156

[10] K. M. Hanson, Noise And Contrast Discrimination In Computed Tomography, Radiology of the skull and brain TECHNICAL ASPECTS OF COMPUTED TOMOGRAPHY Vol. 5, 1981, p. 1 - 15

[11] M.Soleimani, Pengpen.T., Introduction: a brief overview of iterative algorithms in X-ray computed tomography, 2015, Phil.Trans.R.Society, p.4-7

[12] Gordon R., Bender R., Herman GT., Algebraic reconstruction techniques (ART) for three-dimensional electron microscopy and X-ray photography, journal of theoretical biology, 1970, p. 471-481.

[13] Herman GT, Meyer LB, Algebraic reconstruction techniques can be made computationally efficient, IEEE Trans, 1993, p. 600–609.

[14] W. Jiang, X. Zhang, Relaxation factor optimisation for common iterative algorithms in optical computed tomography, Hindawi - mathematical problems in engineering, 2017, p. 7.

[15] Dr.U.Hohenester, Computerized Tomography, Karl-Franenz university, 2015, p. 14-20

[16] L. Birnbacher, M. Viermetz and W. Noichl, X-ray Computed Tomography, Munich School of Bioengineering Technical University of Munich, 2019, p. 7-11.

[17] Michael F. McNitt-Gray, Tradeoffs in CT Image Quality and Dose, Depart of Radiology, David Geffen school of medicine, 2006, p. 2-8

[18] M. Ohkubo, S. Wada and others, mage filtering as an alternative to the application of a different reconstruction kernel in CT imaging: feasibility study in lung cancer screening, pubmed.gov, 2011, p. 1-2

[19] Iinternational atomic energy agency (IAEA), Image post processing and analysis, Diagnostic Radiology Physics: A Handbook for Teachers and Students, p. 1-176

[20] R.Rana, A. Verma, Comparison and Enhancement of Digital Image by Using Canny Filter and Sobel Filter, IOSR Journal of Computer Engineering, 2014, p. 6-10

[21] W. K. Al-Jibory, Ali El-Zaart, Edge Detection In X-ray Computed Tomography Images Using Weibull Distribution, Beirut arab university, 2001, p. 2

[22] O. R. Vincent, O. Folorunso, A Descriptive Algorithm for Sobel Image Edge Detection, Proceedings of Informing Science & IT Education Conference, 2009, p. 98-104

[23] M. Sc. R. Abdul, R. A. R. Lateef, Expansion and Implementation of a 3x3 Sobel and Prewitt Edge Detection Filter to a 5x5 Dimension Filter, 2019, Baghdad College of Economic Sciences University, p. 1 -12

[24] S.N. Kumar, A. L Fred, A. K. Haridhas, Medical image edge detection using gauss gradiant operator, Journal of Pharmaceutical Sciences and Research, 2019, p. 695 - 703

[25] M. Rafati, M. Arabfarb, M. H. Rahimzadev, Comparison of Different Edge Detections and Noise Reduction on Ultrasound Images of Carotid and Brachial Arteries Using a Speckle Reducing Anisotropic Diffusion Filter, Iran Red Crescent Med, 2014, p. 2-3

[26] P. Kaur, R. Kant, A Review on Comparison and Analysis of Edge Detection Techniques, Department of ECE, RBIEBT, Kharar, Punjab, India, 2014, p. 39

[27] S. V. Fotin, D. F. Yankelevitz, C. I. Henschke, A. P. Reeves, A multiscale Laplacian of Gaussian (LoG) filtering approach to pulmonary nodule detection from whole-lung CT scans, American cancer society , 2019, p. 14-15

[28] B.Ganeshan, K. A. Miles, R. C. D. Young, C. R. Chatwin, Texture analysis in non-contrast enhanced CT: Impact of malignancy on texture in apparently disease-free areas of the liver, Department of Engineering & Design, University of Sussex, Falmer, 2007, p. 101-109

[29] Z. Al-Ameen, G. Sulong, Reducing the Gaussian blur artifact from CT medical images by employing a combination of sharpening filters and iterative deblurring algorithms, Journal of Theoretical and Applied Information Technology, 2012, p. 31-36

[30] ed.ac.uk, Gausian smoothing / Spatial Filters, 2003, internet – accessed, 2021/04/20, <https://homepages.inf.ed.ac.uk/rbf/HIPR2/gsmooth.htm>

[31] H. Kong, H. C. Akakin, S. E. Sarma, A Generalized Laplacian of Gaussian Filter for Blob Detection and is applications, IEEE transactions on cybernetics vol. 43.p. 1719 - 1722

[32] E. A. Sekehravani, E. Babulak, M. Masoodi, Implementing Canny Edge detection algorithm for noisy image, Bulletin of Electrical Engineering and Informatics, 2020, p. 1404 - 1410

[33] R. P. K. Reddy, C. Nagaraju, I. R. Reddy, Canny Scale Edge Detection, Y.S.R.Engineering College of YV University, 2016, p. 1-3

[34] E.Punarselvam, P.Suresh, Edge Detection of CT scan Spine disc image using Canny Edge Detection Algorithm based on Magnitude and Edge Length, Institute of electrical and electronic engineers, 2012, p. 806-813.

[35] A. Castro, C. Dafonte, B. Arcay, The Performance of Various Edge Detector Algorithms in the Analysis of Total Hip Replacement X- ays, Faculty of Computer Sciences, University of A Coruña, 2005, p. 506-516

[36] R.Noviana, I. Rasal, E. U. Cintamurni Lubris, Axial Segmentation of Lungs CT Scan Images Using Canny Method and Morphological Operation, Faculty of Computer Science and Information Technology. Gunadarma University, 2017, p. 2-8

[37] F.Qadir, M. A. Peer, K. A. Khan, Efficient edge detection methods for diagnosis of lung cancer based on twodimensional cellular automata, Department of Comp. Science, University of Kashmir, 2012, p. 2050-2058

[38] S. K. T Hwa[1], A. Bade, M. H. Ahmad Hijazi, Enhanced Canny edge detection for Covid-19 and pneumonia X-Ray images, 1Faculty of Science and Natural Resources, Universiti Malaysia Sabah, 2020, p. 1-7.

[39] S. K. Jadwaa, Wiener Filter Based Medical Image De-Noising, Al-Nahrain University -College of Medicine, 2018, p. 318 - 322

[40] Rice University web resource, Wiener Filtering, internet – accessed, 2021/04/23, <https://www.owlnet.rice.edu/~elec539/Projects99/BACH/proj2/wiener.html>

[41] C. Anam, F. Haryanto, R. Widita, I. Arif, New noise reduction method for reducing CT scan dose: Combining Wiener filtering and edge detection algorithm, Department of Physics, Faculty of Mathematics and Sciences, Diponegoro University, Indonesia, 2015, p.1-2

[42] C. Anam, T. Fujibuchi, T. Toyoda and others, An investigation of a CT noise reduction using a modified of wiener filtering-edge detection, Journal of Physics: Conference Series volume 1217, 2019, p. 2-7

[43] World cancer research fund, Worldwide cancer data, American 2018, internet accessed – 2021/04/24, <https://www.wcrf.org/dietandcancer/cancer-trends/worldwide-cancer-data>

[44] M. T. Kitapci, Atlast of sectional radiological anatomy for PET/CT, Gazi university school of medicine, 2012, p. 66-117

[45] T. B. Moeller, Pocket Atlas of Sectional Anatomy CT and MRI, Stutgart and New York, 2001, p. 148 - 208

[46] IAEA Human health reports No. 11, Strategies for the Management of Localized Prostate Cancer: A Guide for Radiation Oncologists, International Atomic Energy Agency, 2014, p. 2 - 36

[47] B. W. Fischer-Valuk, Y.J. Rao, J. M. Michalski, Intensity-modulated radiotherapy for prostate cancer, Pubmed database, 2018, p. 1-6

[48] M. Antico, P. Prinsen, F. Celini, A. Francassi, A. A.Isolo and others, Real-time adaptive planning method for radiotherapy treatment delivery for prostate cancer patients, based on a library of plans accounting for possible anatomy configuration changes, School of Chemistry, Physics and Mechanical Engineering, Queensland University of Technology, 2018 p.3-6.

[49] IAEA Human health reports No. 6, Management of Cervical Cancer: Strategies for Limited-resource Centres — A Guide for Radiation Oncologists, International atomic energy agency, 2013, p. 2 - 29

[50] Chapel Hill, PlanUNC version 6.8.26 User Guide, Department of radiation oncology, University of north carolina, 2015, p.1-7.

Appendices

Appendix 1. MAR filtering algorithm in Matlab

```
%AUTOMATIC ANONIMIZER
clc, close all, clear all

% disp('Perskaitomasdicomfailas')
% I=dicomread(‘X.dcm');
%
% dicomanon('X.dcm'
%     'anonymized.dcm')
% % [m n]=size(I)

values.StudyInstance.UID=dicomuid;
values.SeriesInstance.UID=dicomuid;

d=dir('*.dcm')
for p=1:numel(d)
dicomanon(d(p).name, sprintf('anon%d.dcm',p),'update', values)
end

%MAR ALGORITHM
clc, close all, clear all

disp('Perskaitomasdicomfailas')
I=dicomread('X.dcm');

disp('Pavaizduojamasdicomfailas')
%figure
imshow(I, 'DisplayRange',[]);
% imtool(I, 'DisplayRange',[])

%figure
BW1=edge(I)
imshow(BW1), title('Edge filtras')

%figure
BW2=edge(I,'Sobel')
imshow(BW2),  title('Edge-Sobel filtras')

%figure
BW3=edge(I,'Sobel',0.0003)
imshow(BW3), title('Edge-Sobel filtrasir thresh')

%figure
BW4=edge(I,'prewitt')
imshow(BW4), title('Edge-Prewitt filtras')

%figure
```

```
BW5=edge(I,'prewitt',0.0001)
imshow(BW5), title('Edge-Prewitt filtrasir thresh')

%figure
BW6=edge(I,'roberts')
imshow(BW6), title('Edge-Roberts filtras')

%figure
BW7=edge(I,'roberts',0.0002)
imshow(BW7), title('Edge-Roberts filtrasir thresh')

%figure
BW8=edge(I,'log')
imshow(BW8), title('log filtras')

%figure
BW9=edge(I,'log',0.000002)
imshow(BW9), title('log filtrasir thresh')

%figure
BW10=edge(I,'log',0.000002,4)
imshow(BW10), title('Edge-log filtras, thresh, sigma')

%figure
BW11=edge(I,'zerocross')
imshow(BW11), title('Edge-zerocrossfiltras')

%figure
BW12=edge(I,'zerocross',0.00001)
imshow(BW12), title('Edge-zerocrossfiltras, thresh')

%figure
BW13=edge(I,'zerocross',0.0000)
imshow(BW13), title('Edge-zerocrossfiltras, threshold=0')

%figure
BW14=edge(I,'zerocross',0.00001)
imshow(BW14), title('Edge-zerocrossfiltras, threshold')

%figure
BW15=edge(I,'canny')
imshow(BW15), title('Edge-Canny filtras') %, threshold')

%figure
BW16=edge(I,'canny', 0.0001)
imshow(BW16), title('Edge-Canny filtrasir threshold')

disp('**********')
```

```
%figure
subplot(2,2,1)
imshow(I, 'DisplayRange',[]), title('Originalinuotrauka')

BW17=fspecial('motion',200,45);
MotionBlur=imfilter(I,BW17,'replicate')
subplot(2,2,2)
imshow(MotionBlur), title('fspecialfiltrasirMotionBlur - replicate nuotrauka')

BW18=fspecial('disk',20);
Blurred=imfilter(I,BW18,'replicate')
subplot(2,2,3)
imshow(Blurred), title('Blurred - replicate nuotrauka')

BW19=fspecial('average');
Blurred=imfilter(I,BW19,'replicate')
subplot(2,2,4)
imshow(Blurred), title('Blurred average - replicate nuotrauka')

figure
BW20=fspecial('gaussian');
Blurred=imfilter(I,BW20,'replicate')
imshow(Blurred), title('Blurred Gaussian - replicate nuotrauka')

disp('Irasomasmodifikuotaspaveikslasinaujadicomfaila:')
dicomwrite(Blurred,'aaa.dcm');
%pause
%figure
%BW21=fspecial('laplacian');
%Blurred=imfilter(I,BW21,'replicate')
%imshow(Blurred), title('Blurred Laplacian- replicate nuotrauka')

%figure
%BW22=fspecial('log');
%Blurred=imfilter(I,BW22,'replicate')
%imshow(Blurred), title('Blurred log- replicate nuotrauka')

%InstanceUID altering
clc, close all, clear all
I=dicomread('X.dcm');
info = dicominfo('X.dcm');

%dicomwrite(I,'60.dcm',info);
%instancnumber altering

clc, close all, clear all
I=dicomread('72.dcm');
```

```
%uid = dicomuid;
info.SeriesInstanceUID = uid;
info.StudyInstanceUID = uid;
dicomwrite(I,'72.dcm',info); %

%dicomwrite(Blurred,'nuotrauka_su_Gausofiltru.dcm');
% info = dicominfo('1.dcm');
%info2 = dicominfo('new2.dcm');
%info3 = dicominfo('new1.dcm');

clc, close all, clear all
I=dicomread('001.dcm');

%info = dicominfo('001.dcm') %nereik
info2 = dicominfo('CT.1.2.840.113619.2.278.3.2831185940.922.1586841586.402.1.dcm')
%dicomwrite(I,'1.dcm',info);
%uid = dicomuid;
%uid2 = dicomuid;
uid = '1.3.6.1.4.1.9590.100.1.2.614523337120836005144710569021106860 74'
uid2 = '1.3.6.1.4.1.9590.100.1.2.183343010611444776000781595261999547223'

info.SeriesInstanceUID = info2.SeriesInstanceUID;
info.StudyInstanceUID = info2.StudyInstanceUID;
info.RotationDirection = info2.RotationDirection;
info.PatientPosition = info2.PatientPosition;
info.AcquisitionNumber = info2.AcquisitionNumber
info.FocalSpot = info2.FocalSpot;
info.ImagePositionPatient = info2.ImagePositionPatient;
info.ImageOrientationPatient = info2.ImageOrientationPatient;
info.FrameOfReferenceUID = info2.FrameOfReferenceUID;
info.PositionReferenceIndicator = info2.PositionReferenceIndicator;
info.SliceLocation = info2.SliceLocation;
info.Modality = info2.Modality;
info.ImageType = info2.ImageType;
info.SpecificCharacterSet = info2.SpecificCharacterSet;
info.StudyDescription = info2.StudyDescription;
info.SeriesDescription = info2.SeriesDescription;
info.ScanOptions = info2.ScanOptions;
info.SliceThickness = info2.SliceThickness;
info.DataCollectionDiameter = info2.DataCollectionDiameter;
info.SoftwareVersion = info2.SoftwareVersion;
info.ReconstructionDiameter = info2.ReconstructionDiameter;
info.DistanceSourceToDetector = info2.DistanceSourceToDetector;
info.DistanceSourceToPatient = info2.DistanceSourceToPatient;
info.GantryDetectorTilt = info2.GantryDetectorTilt;
info.TableHeight = info2.TableHeight;
info.ExposureTime = info2.ExposureTime;
info.XrayTubeCurrent = info2.XrayTubeCurrent;
```

```
info.Exposure = info2.Exposure;
info.FilterType = info2.FilterType;
info.GeneratorPower = info2.GeneratorPower;
info.PatientPosition = info2.PatientPosition;
info.FrameOfReferenceUID = info2.FrameOfReferenceUID;
info.SamplesPerPixel = info2.SamplesPerPixel;
info.PositionReferenceIndicator = info2.PositionReferenceIndicator;
info.WindowCenter = info2.WindowCenter;
info.WindowWidth = info2.WindowWidth;
info.RescaleIntercept = info2.RescaleIntercept;
info.RescaleSlope = info2.RescaleSlope;
info.SOPInstanceUID = info2.SOPInstanceUID;
%info.SOPClassUID = info2.SOPClassUID; % MATRICOS KEITIKLIS
info.PatientID = info2.PatientID; %
info.PatientName = info2.PatientName; %
info.Manufacturer = info2.Manufacturer;
info.Modality = info2.Modality;
info.StudyDate = info2.StudyDate;
info.FileMetaInformationGroupLength = info2.FileMetaInformationGroupLength;
info.InstanceCreationDate = info2.InstanceCreationDate;
info.InstanceCreationTime = info2.InstanceCreationTime;
info.AccessionNumber = info2.AccessionNumber;
info.StudyID = info2.StudyID;
info.SeriesInstanceUID = uid;
info.StudyInstanceUID = uid;
info.Format = info2.Format;
info.FormatVersion = info2.FormatVersion;
info.Height = info2.Height;
info.BitDepth = info2.BitDepth;
info.ColorType = info2.ColorType;
info.FileMetaInformationVersion = info2.FileMetaInformationVersion;
%info.MediaStorageSOPClassUID = info2.MediaStorageSOPClassUID;
info.MediaStorageSOPInstanceUID = info2.MediaStorageSOPInstanceUID;
%info.TransferSyntaxUID = info2.TransferSyntaxUID;
info.ImplementationClassUID = info2.ImplementationClassUID;
%info.ImplementationVersionName = info2.ImplementationVersionName;
info.ContentDate = info2.ContentDate;
info.StudyTime = info2.StudyTime;
info.ContentTime = info2.ContentTime;
%info.ConversionType = info2.ConversionType;
info.PatientBirthDate = info2.PatientBirthDate;
info.PatientSex = info2.PatientSex;
%info.SecondaryCaptureDeviceManufacturer = info2.SecondaryCaptureDeviceManufacturer;
info.SeriesNumber = info2.SeriesNumber;
info.InstanceNumber = info2.InstanceNumber;
%info.PhotometricInterpretation = info2.PhotometricInterpretation;
%info.Rows = info2.Rows;
%info.Columns = info2.Columns;
```

```
%info.BitsAllocated = info2.BitsAllocated;
%info.BitsStored = info2.BitsStored;
%info.HighBit = info2.HighBit;
%info.PixelRepresentation = info2.PixelRepresentation %
%info.ImagePositionPatient = info2.ImagePositionPatient;
%info.ImageOrientationPatient = info2.ImageOrientationPatient; %
%info.PositionReferenceIndicator = info2.PositionReferenceIndicator;
%info.SliceLocation = info2.SliceLocation;
%info.PatientPosition = info2.PatientPosition;
%info.WindowCenter = info2.WindowCenter;
%info.RescaleIntercept = info2.RescaleIntercept;
%info.RescaleSlope = info2.RescaleSlope; %
%info.Private_3241_10xx_Creator = info2.Private_3241_10xx_Creator;
%info.Private_3241_1000 = info2.Private_3241_1000;
%info.Private_3241_1004 = info2.Private_3241_1004;
%info.Private_3241_1005 = info2.Private_3241_1005;
%info.Private_3241_1006 = info2.Private_3241_1006;
%info.Private_3253_10xx_Creator = info2.Private_3253_10xx;
%info.Private_3253_1000 = info2.Private_3253_1000;
%info.Private_3253_1001 = info2.Private_3253_1001;
%info.Private_3253_1002 = info2.Private_3253_1002;
%info.FocalSpot = info2.FocalSpot;
%info.SliceLocation = info2.SliceLocation;
%info.PositionReferenceIndicator = info2.PositionReferenceIndicator;

info3 = info;
dicomwrite(I, 'naujas001.dcm',info3);
%dicomwrite(I, 'naujas001.dcm', info3, 'CreateMode', 'copy');

%info2 = dicominfo('001.dcm')
%info3 = dicominfo('002.dcm')
```

Appendix 2. Patient No. 2 original and MAR algorithm filtered CT data sets, slice No. 44

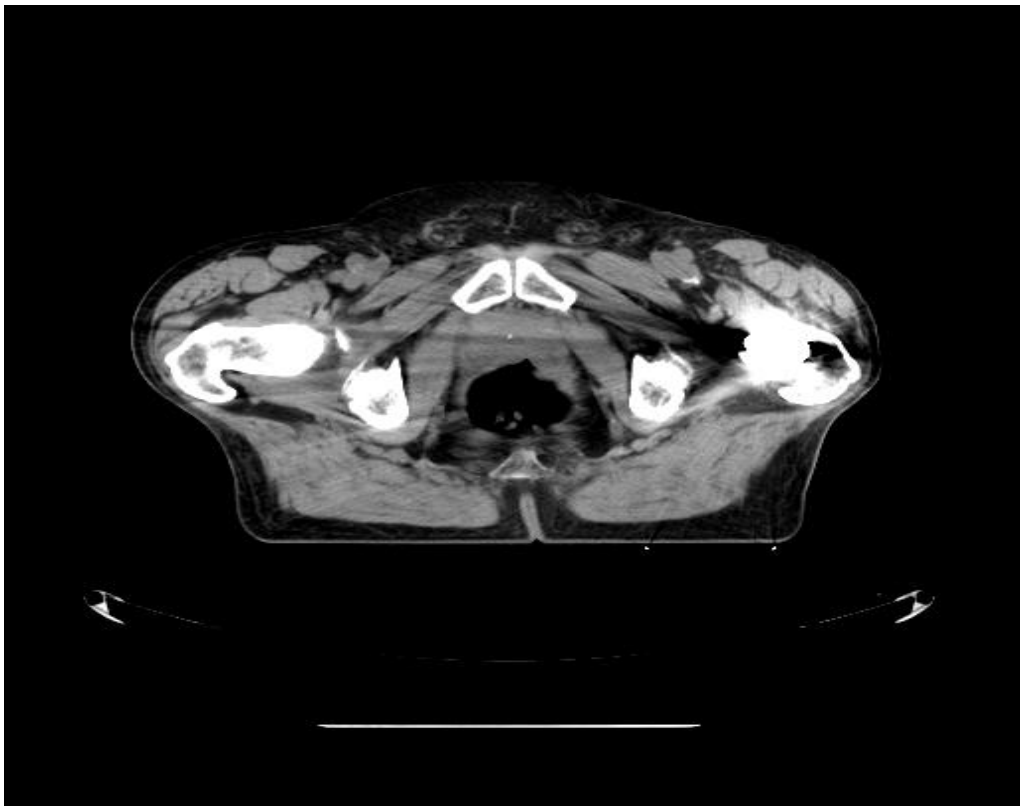

Fig. 49. Patient No. 2 original CT pelvic region, Kaunas Clinics, Hospital Of Oncology

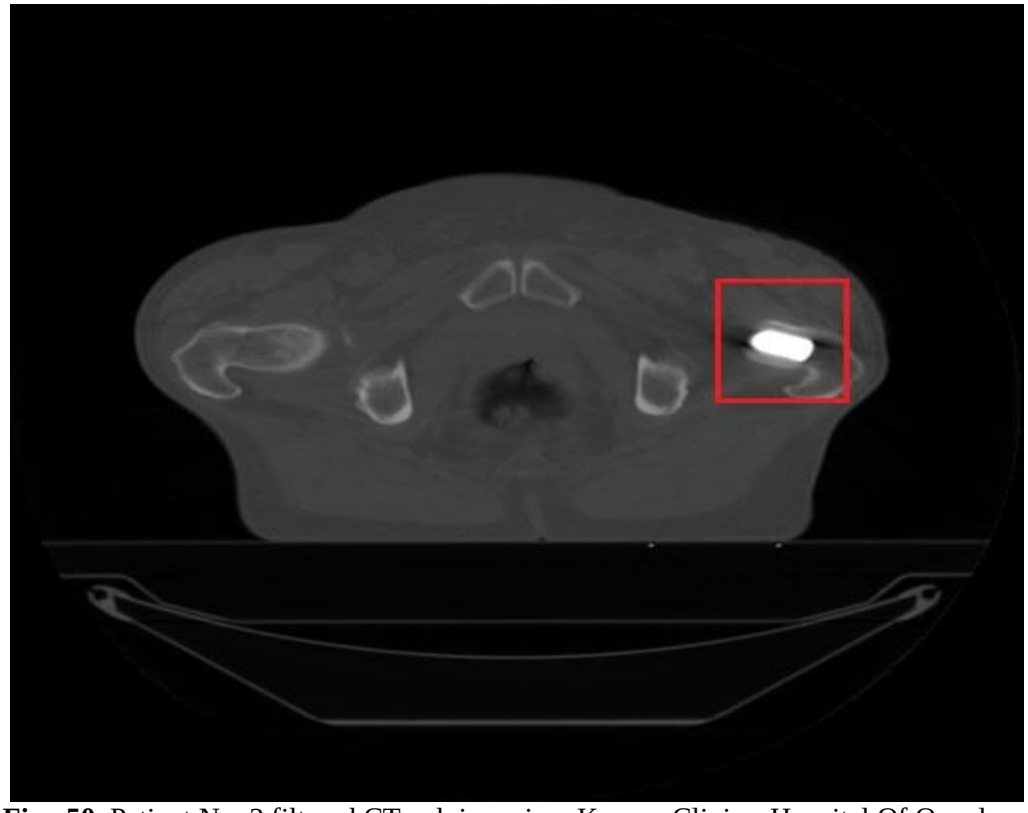

Fig. 50. Patient No. 2 filtered CT pelvic region, Kaunas Clinics, Hospital Of Oncology

Appendix 3. Patient No. 3 original and MAR algorithm filtered CT data sets, slice No. 83

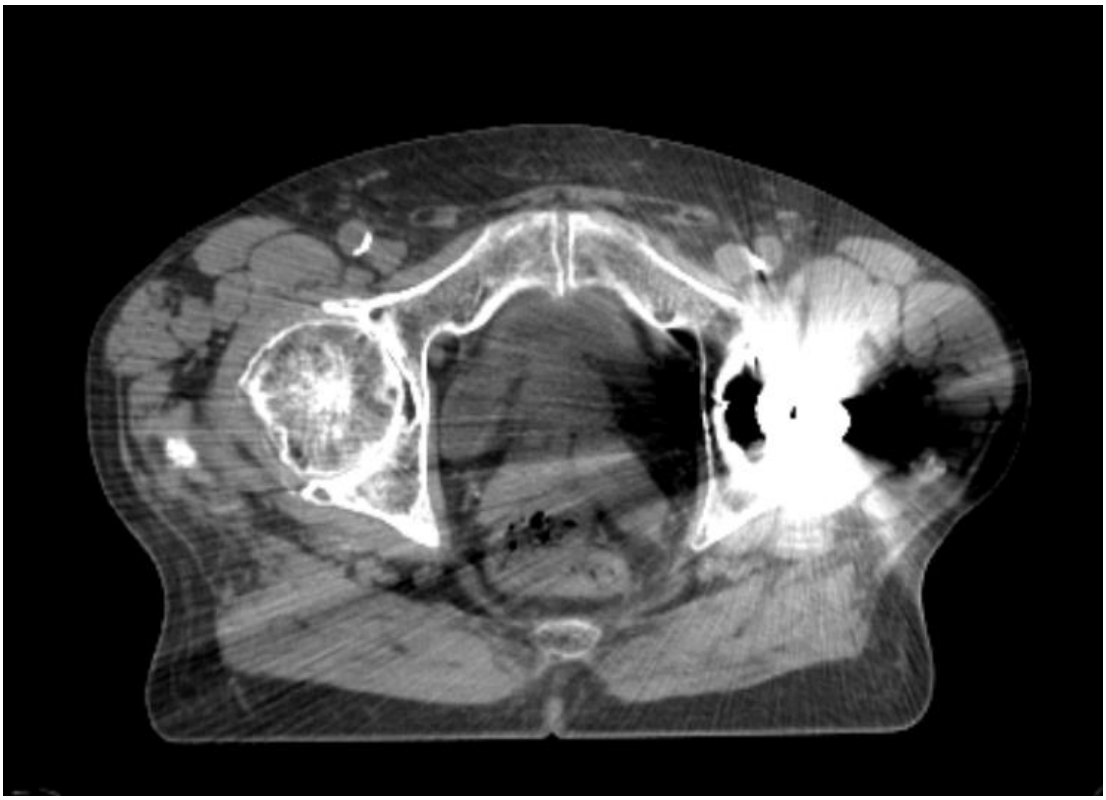

Fig. 51. Patient No. 3 original CT pelvic region, Kaunas Clinics, Hospital Of Oncology

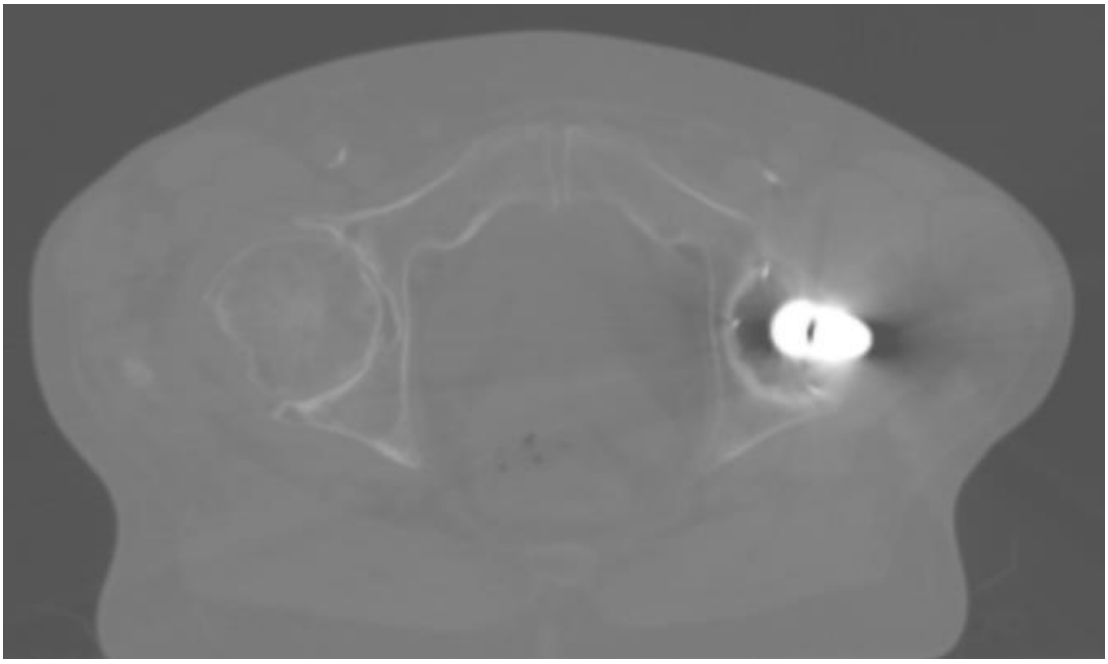

Fig. 52. Patient No. 3 filtered CT pelvic region, Kaunas Clinics, Hospital Of Oncology

Appendix 4. Patient No. 4 original and MAR algorithm filtered CT data sets, slice No. 69

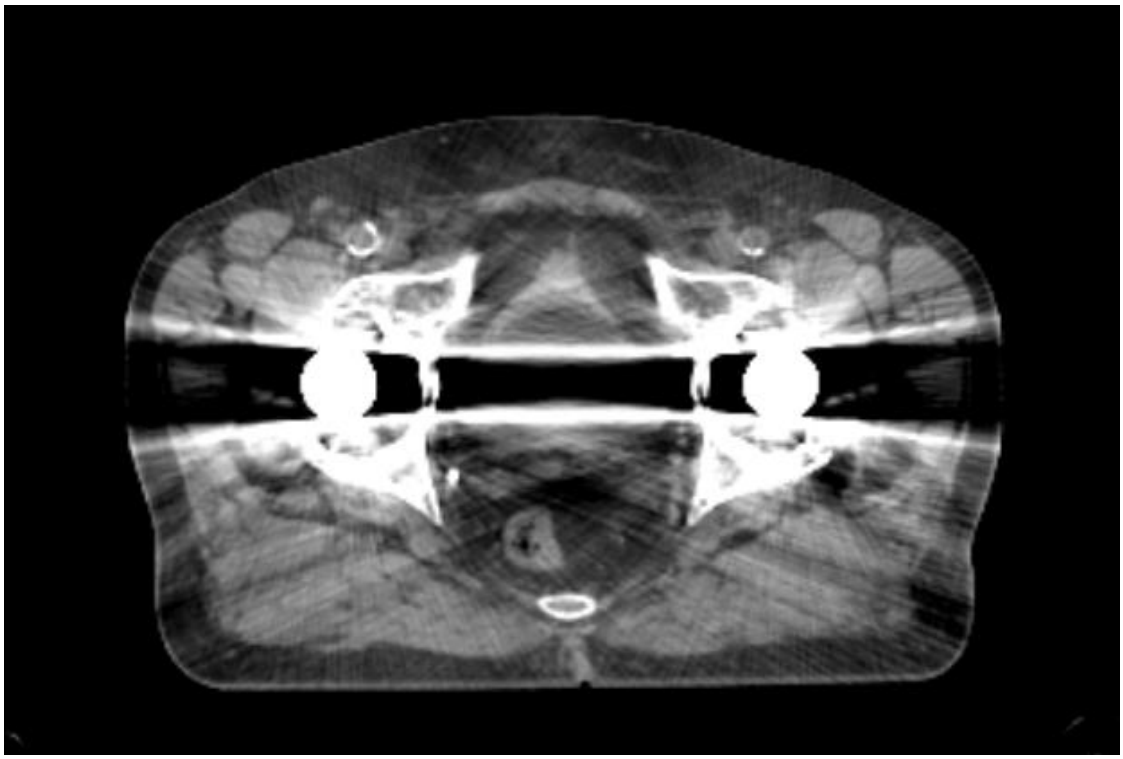

Fig. 53. Patient No. 4 original CT pelvic region, Kaunas Clinics, Hospital Of Oncology

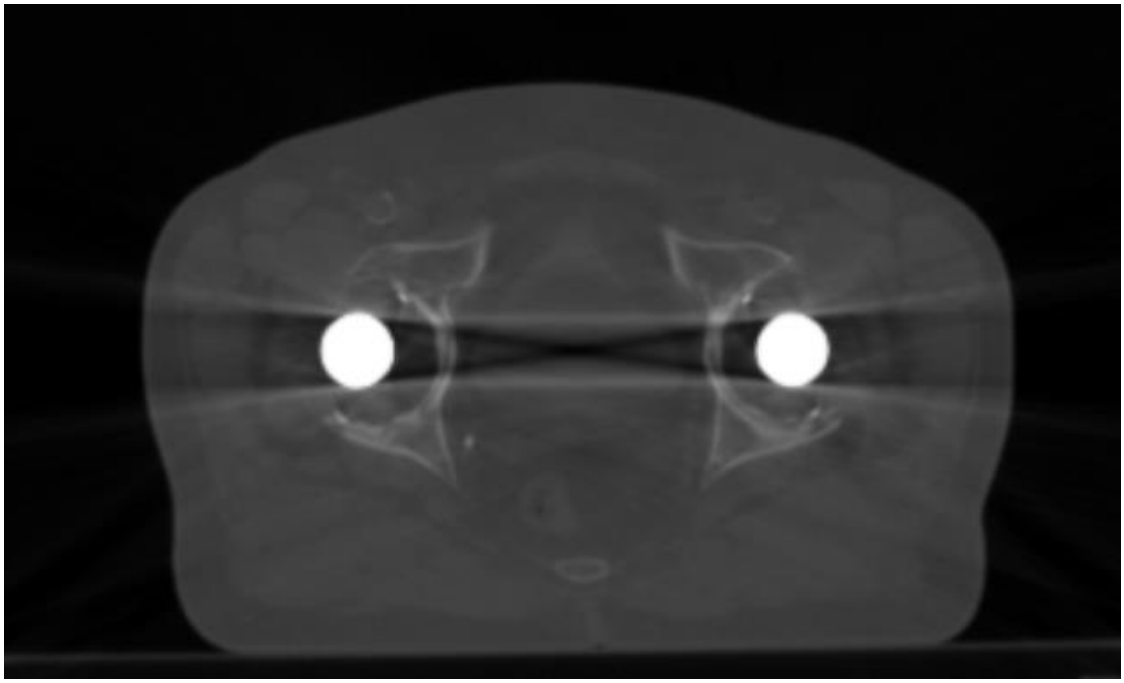

Fig. 54. Patient No. 4 filtered CT pelvic region, Kaunas Clinics, Hospital Of Oncology

Appendix 5. Patient No. 5 original and MAR algorithm filtered CT data sets, slice No. 44

Fig. 55. Patient No. 5 original CT pelvic region, Kaunas Clinics, Hospital Of Oncology

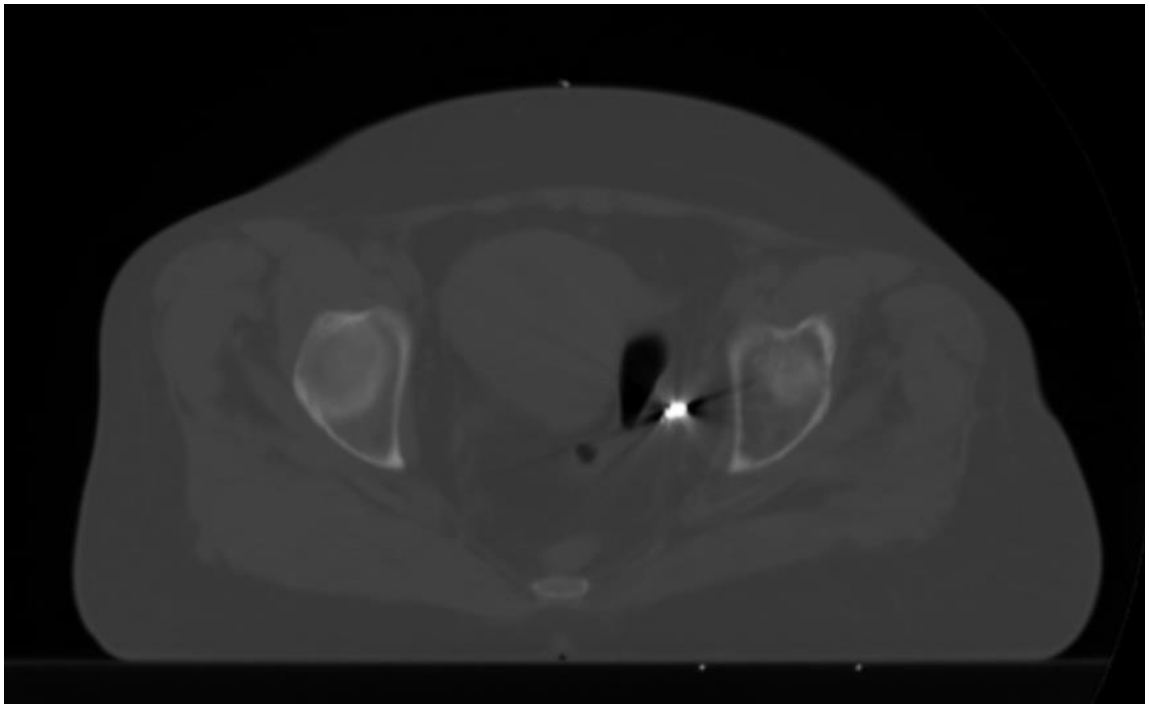

Fig. 56. Patient No. 5 filtered CT pelvic region, Kaunas Clinics, Hospital Of Oncology

Appendix 6. Patient No. 6 original and MAR algorithm filtered CT data sets, slice No. 75

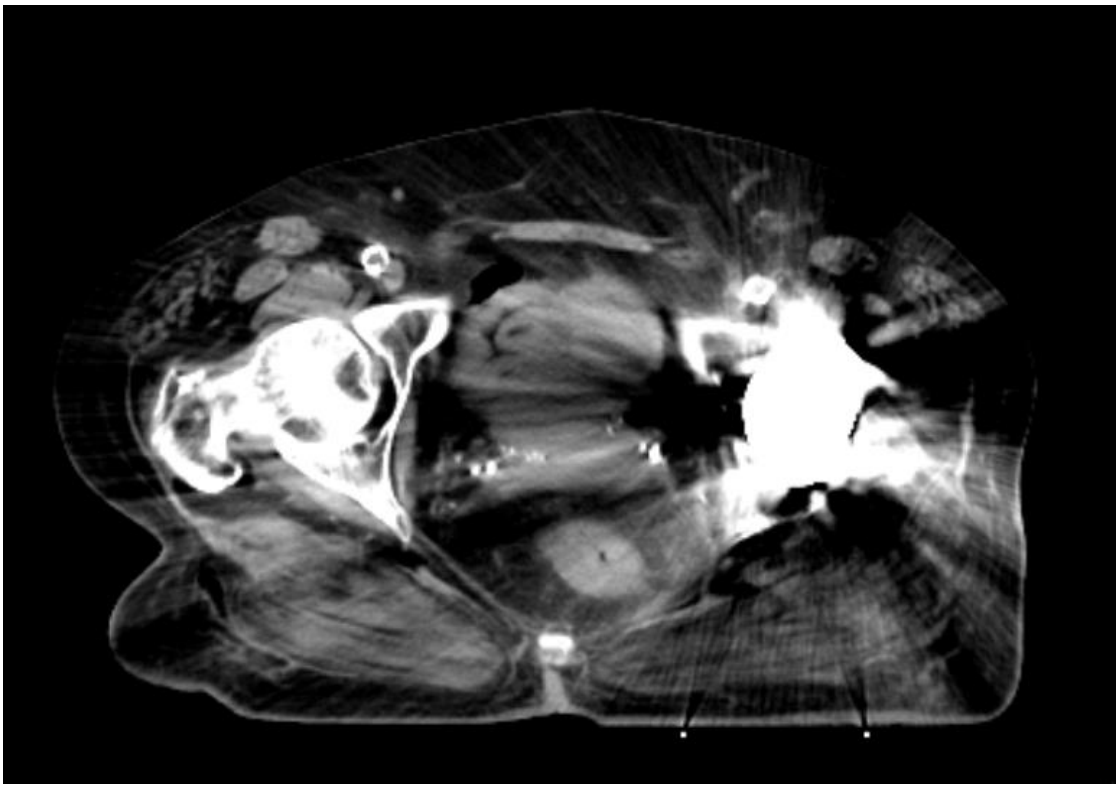

Fig. 57. Patient No. 6 original CT pelvic region, Kaunas Clinics, Hospital Of Oncology

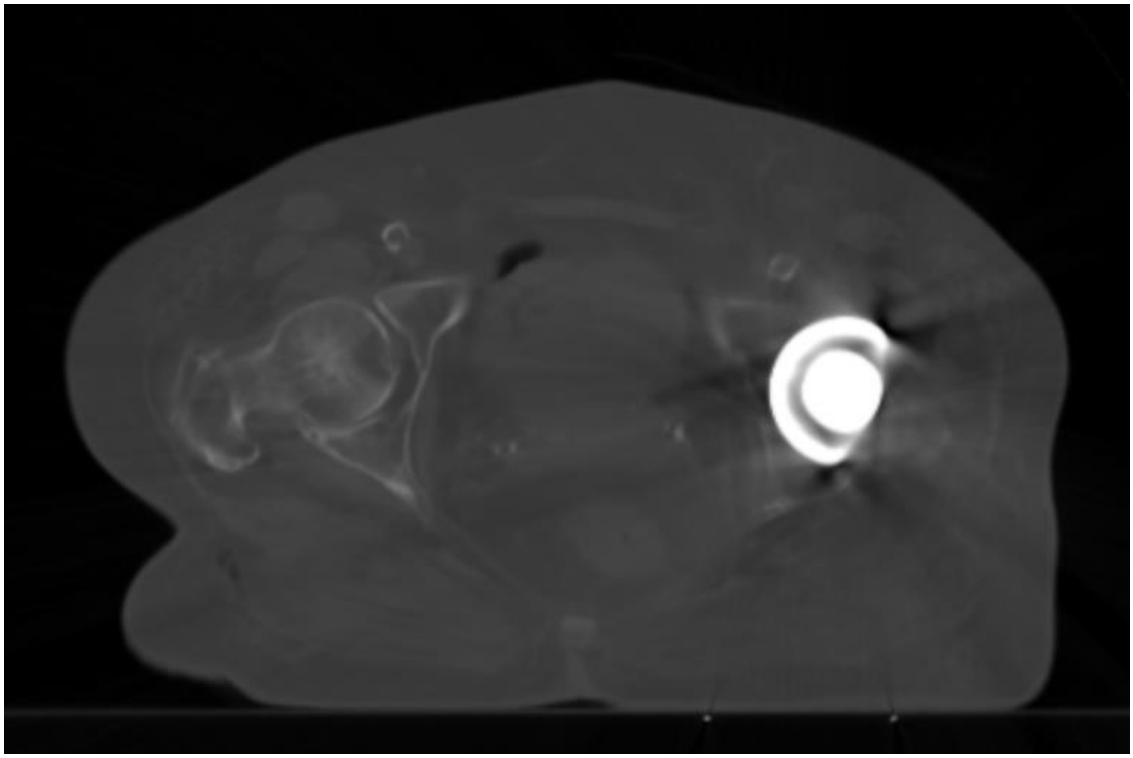

Fig. 58. Patient No. 6 filtered CT pelvic region, Kaunas Clinics, Hospital Of Oncology

Appendix 7. Patient No. 7 original and MAR algorithm filtered CT data sets, slice No. 51

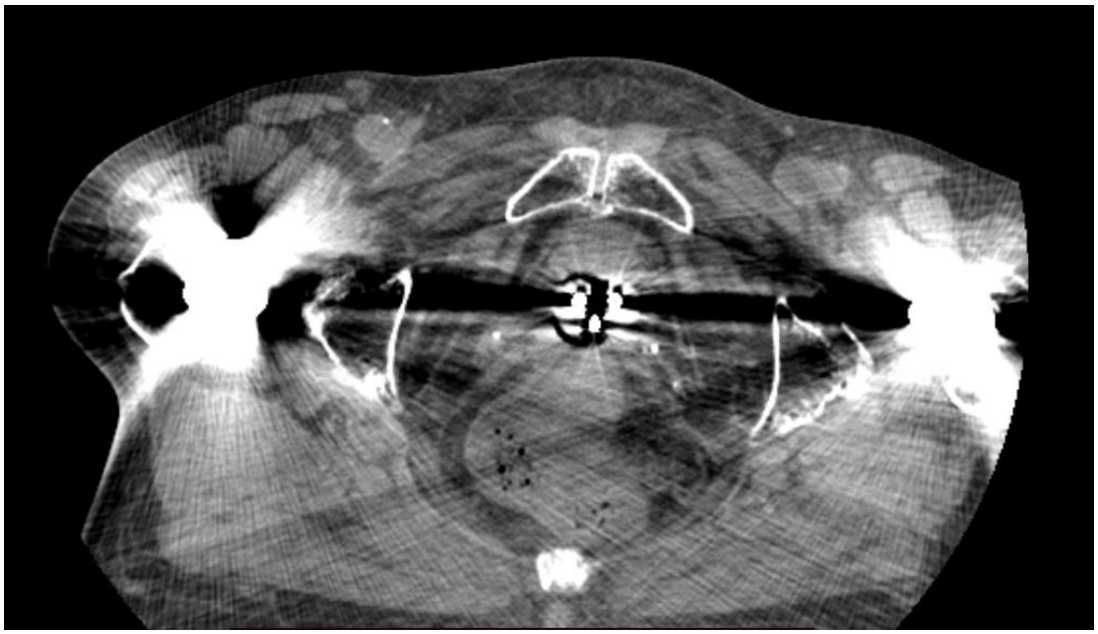

Fig. 59. Patient No. 7 original CT pelvic region, Kaunas Clinics, Hospital Of Oncology

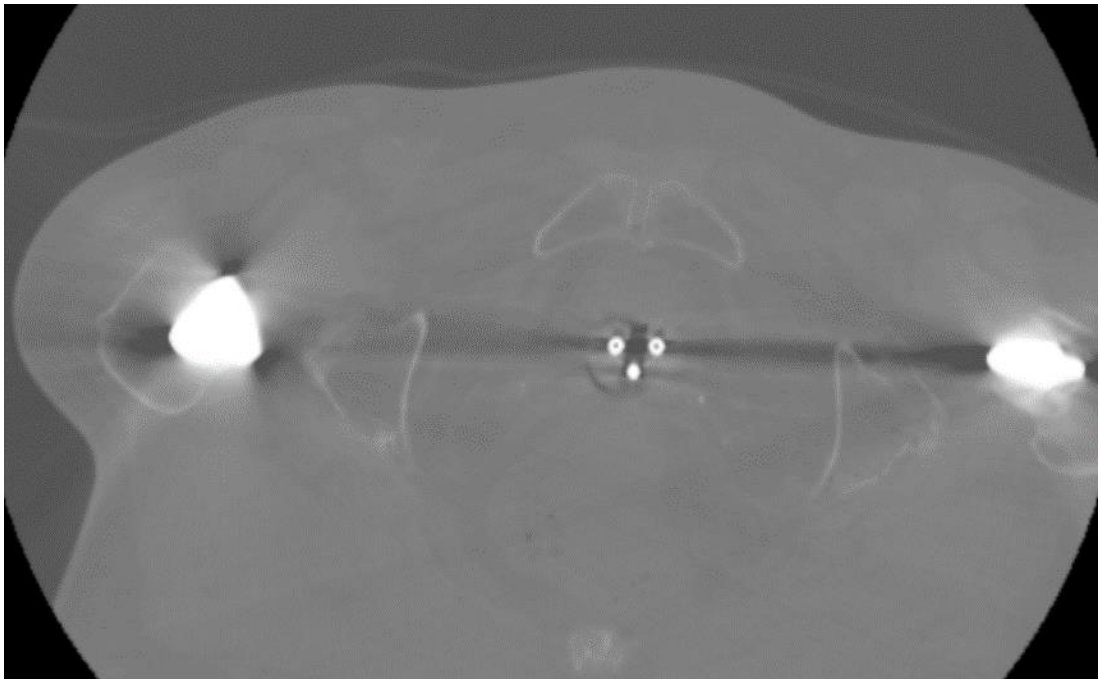

Fig. 60. Patient No. 7 filtered CT pelvic region, Kaunas Clinics, Hospital Of Oncology